

---

# Search for heavy Higgs bosons in the $Z + t\bar{t}$ final state with the CMS detector

---

Master thesis

Yannick Fischer

December 2021





1. Gutachter: Prof. Dr. Johannes Haller
2. Gutachter: Jun-Prof. Dr. Gregor Kasieczka



## Abstract

This thesis presents the first studies at the LHC for a search for heavy Higgs bosons in the decay mode  $A \rightarrow ZH(t\bar{t})$ . The analysis is performed with simulated proton-proton collision data at a centre of mass energy of  $\sqrt{s} = 13$  TeV at the CMS experiment.

A comprehensive study of the Two-Higgs doublet model 2HDM (type II) parameter space is given by analysing production cross section and branching ratios with respect to the 2HDM model parameters. Signal events have been simulated for different mass configurations and their kinematic properties have been compared, also to several standard model background processes. The transverse momentum of the reconstructed  $Z$  boson is found to be a powerful variable discriminating the signal from the background. Expected exclusion limits on the  $A \rightarrow ZH$  production cross section are derived. They are expected to exclude a large part of the 2HDM parameter space, especially in the high  $m_A$  and low  $\tan(\beta)$  regime, complementing existing searches in other channels.



## Kurzfassung

Diese Arbeit stellt die erste Analysestrategie am LHC für eine Suche nach schweren Higgs-Bosonen im Zerfallskanal  $A \rightarrow ZH(t\bar{t})$  vor. Die Analyse basiert auf simulierten Proton-Proton-Kollisionsdaten des CMS-Experiments am LHC bei einer Energie von  $\sqrt{s} = 13$  TeV.

Diese Arbeit liefert eine umfassende Analyse des 2HDM-(Typ II)-Parameterraumes durch die Betrachtung des Wirkungsquerschnitts und der Verzweigungsverhältnisse in Abhängigkeit der 2HDM-Modellparameter. Signalereignisse für die verschiedenen Massenpunkte wurden simuliert und ihre kinematischen Eigenschaften wurden untereinander und mit diversen Standardmodellhintergründen verglichen. Der transversale Impuls des rekonstruierten Z-Bosons wurde als Variable identifiziert, mit der das Signal effektiv vom Hintergrund getrennt werden kann. Erwartete Ausschlusslimits auf den  $A \rightarrow ZH$  Produktionsquerschnitt wurden berechnet. Die berechneten Limits schließen einen großen Bereich des Parameterraums aus, insbesondere die Bereiche mit hohen Massen  $m_A$  und niedrigen Werten für  $\tan(\beta)$ , und ergänzen so bereits bestehende Analysen anderer Zerfallskanäle.

# Contents

<b>1</b>	<b>Introduction</b>	<b>1</b>
<b>2</b>	<b>Theoretical background</b>	<b>2</b>
2.1	The Standard Model . . . . .	2
2.1.1	Particles in the SM . . . . .	2
2.1.2	Quantum electrodynamics . . . . .	4
2.1.3	Quantum chromodynamics . . . . .	5
2.1.4	Electroweak unification . . . . .	6
2.1.5	The Higgs mechanism . . . . .	8
2.2	Shortcoming of the Standard Model . . . . .	11
2.3	The Two-Higgs-doublet model . . . . .	12
2.3.1	The 2HDM potential . . . . .	12
2.3.2	Interaction with fermions . . . . .	19
2.4	Previous 2HDM searches . . . . .	20
2.5	The physics of collider experiments . . . . .	23
<b>3</b>	<b>Analysis of the 2HDM parameter space</b>	<b>25</b>
3.1	Branching ratios . . . . .	25
3.1.1	General remarks on the branching ratios of the involved processes . . . . .	25
3.1.2	$A \rightarrow ZH$ . . . . .	26
3.1.3	$H \rightarrow t\bar{t}$ . . . . .	28
3.2	Production cross sections . . . . .	29
3.2.1	The Standard Model Higgs boson production cross section . . . . .	30
3.2.2	The 2HDM production cross section . . . . .	32
3.3	Product of branching ratios and production cross section . . . . .	34
<b>4</b>	<b>Experimental setup</b>	<b>36</b>
4.1	The Large Hadron Collider . . . . .	36
4.1.1	General features of particle colliders . . . . .	36
4.1.2	Overview over the LHC components and properties . . . . .	37
4.2	The Compact Muon Solenoid Experiment . . . . .	39
4.3	The coordinate system . . . . .	39
4.4	CMS sub detectors . . . . .	40



4.5	Trigger	45
<b>5</b>	<b>Event reconstruction and object identification</b>	<b>47</b>
5.1	Particle Flow Algorithm	47
5.2	Muon identification	48
5.3	Electron identification	49
5.4	Jets	49
5.4.1	Jet clustering	50
5.4.2	Jet calibration	51
5.5	Pileup mitigation	52
5.6	B-jet-tagging	52
<b>6</b>	<b>Search for <math>A \rightarrow ZH(t\bar{t})</math></b>	<b>53</b>
6.1	Signal and background samples	53
6.1.1	The signal samples	53
6.1.2	Background processes	55
6.2	Signal topology at generator level	58
6.2.1	Jets	58
6.2.2	Muons	59
6.3	Event selection	63
6.3.1	Minimal muon momentum	63
6.3.2	Event selection	64
6.4	Signal and background properties at detector level	69
6.5	Results	71
6.5.1	The $CL_s$ technique	72
6.5.2	Systematic uncertainties	74
6.5.3	Expected exclusion limits	75
<b>7</b>	<b>Conclusion and Outlook</b>	<b>82</b>



---

# 1 Introduction

The question of what the universe is made of is as old as mankind. The philosophical idea of a smallest building block for all matter in the universe is present in many ancient philosophies such as Jainism in India [1], or Atomism in Greece [2]. For more than 2000 years this remained a philosophical paradigm rather than a scientific theory. J. Dalton and his work in stoichiometry in the early 19th century was the first evidence for the existence of small particles constituting all matter. Believing the smallest particles had been found, they were named atoms after the Greek word for indivisible. However, this idea was proven wrong about 100 years later when it was discovered that atoms have a substructure. The following years marked a series of important discoveries in physics. The structure of the atom was unravelled by the discovery of the electron (J.J. Thomson 1897 [3]), the proton (E. Rutherford 1918 [4]) and the neutron (J. Chadwick 1932 [5]). The proof that the cores of the so called atoms were in fact divisible was provided by L. Meitner, O.R. Frisch, O. Hahn and F. Straßmann in 1939 [6],[7]. In parallel, quantum mechanics, a description of the kinematics and interactions of the smallest particles, was formulated by people like M. Planck [8], E. Schrödinger [9], W. Heisenberg [10] and N. Bohr [11]. The Standard Model (SM) of particle physics was proposed in the 1970s as a gauge theory. It describes the fundamental particles and their interactions. However, the Standard Model is not complete since it lacks an extension beyond the Planck scale where gravity becomes relevant and can not explain a number of physical phenomena. Consequently, the search for physics beyond the Standard Model (BSM) has become an important field of particle physics.

Several BSM models predict an extended Higgs sector with an additional Higgs doublet compared to the SM, which leads to the existence of five physical Higgs bosons. The phenomenology of such models is described generically by Two-Higgs-Doublet-Models (2HDM), which are used as a benchmark in this thesis.

In this thesis a strategy for a search for heavy Higgs bosons  $A$  in the  $t\bar{t}Z$  final state with the CMS experiment is developed. It targets the decay channel  $A \rightarrow ZH$  with  $H \rightarrow t\bar{t}$ , where  $A$  and  $H$  are two of the four additional heavy Higgs bosons. This channel has not yet been probed at the LHC. The analysis follows the strategy proposed in Ref. [12] and extends it for the application to CMS data for the first time.

This thesis is structured as follows: In chapter 2 an overview of the Standard Model, its shortcomings and the 2HDM is given. Important basis transformation laws are derived, which are needed for the subsequent generation of signal events. Chapter 3 examines the properties of the 2HDM parameter space and the dependency of branching ratios and production cross sections on the model parameters. The chapters 4 and 5 give an overview of the LHC, the CMS detector and the particle reconstruction techniques used by CMS. In chapter 6, the results of this analysis are presented. The kinematic properties of signal events produced with DELPHES as part of this

thesis are compared to background processes. The transverse momentum spectrum of the  $Z$  boson is examined and used as a sensitive variable. With the help of the  $CL_s$  method, expected limits on the production cross section of heavy Higgs bosons are derived and compared to the predicted cross sections. Chapter 7 concludes this thesis and gives an outlook on possible next steps in the analysis.

## 2 Theoretical background

This chapter introduces the basic theoretical concepts of this analysis. In section 2.1 an overview of the Standard Model of particle physics is given. A special focus will be set on the Higgs mechanism. This first section is based on Refs. [13], [14] and [15]. With this information on hand, an introduction to the Two-Higgs-doublet model is given in section 2.3, where an important basis transformation law will be derived. An overview over recent 2HDM searches will be given in section 2.4. Since the experimental results considered in this thesis are obtained with data recorded by the CMS experiment at the LHC, an introduction to collider experiments is given in section 2.5.

### 2.1 The Standard Model

The Standard Model of particle physics (SM) is one of the most successful physical theories in history. It describes the elementary particles of the universe and the forces acting between them. Mathematically, the Standard Model is based on different gauge groups under which the Lagrangian is imposed to be invariant. The most general renormalizable Lagrangian fulfilling these relations is then constructed and its dynamic studied by using the Euler-Lagrange equation. The local symmetry groups of the SM are:

$$SU(3)_C \otimes SU(2)_L \otimes SU(1)_Y \tag{2.1}$$

$SU(3)_C$  is responsible for the strong interaction. The weak and the electromagnetic force can be unified to the electroweak force represented by the product  $SU(2)_L \otimes SU(1)_Y$ .

The Lagrangian invariant under this gauge groups represents quantum fields, pervading space-time. Quantum excitations of these fields can be interpreted as fundamental particles with different properties described in the next sections.

#### 2.1.1 Particles in the SM

A common way to classify the particles of the Standard Model is via their spin. If the spin is half-integer, the particle is called a fermion. Fermions follow the Fermi-Dirac statistic and the Pauli exclusion principle, meaning that two fermions can never be in exactly the same quantum

state. If the spin is an integer (including zero), the particle is called a boson. These particles follow the Bose-Einstein statistic, meaning they can be in a collective ground state. An overview over all particles of the Standard Model can be found in Fig. 2.1.

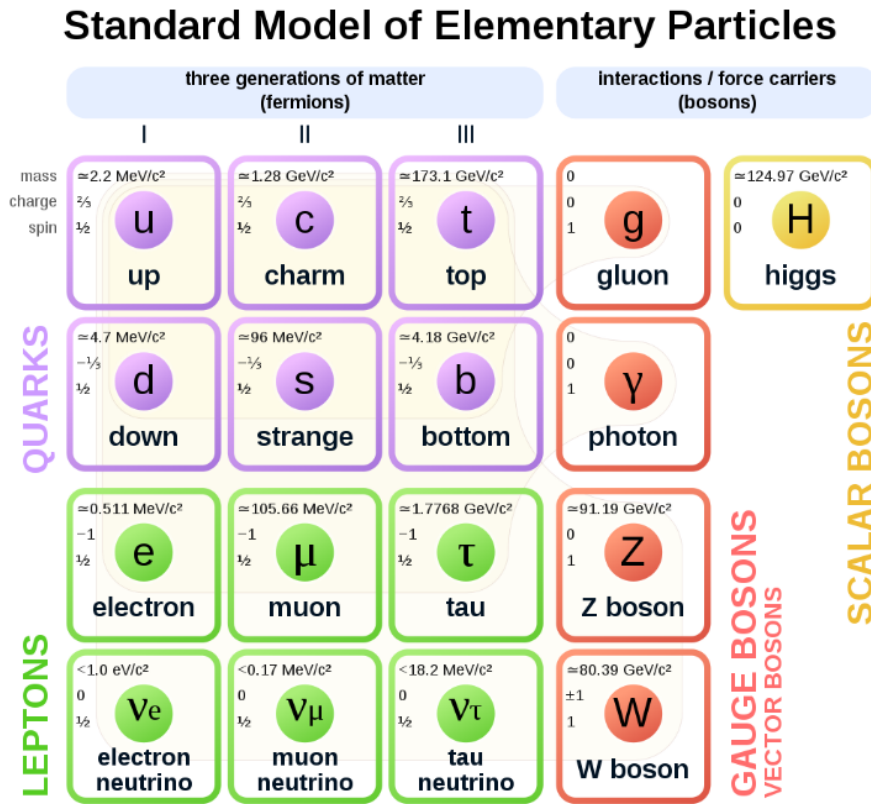


**Figure 2.1** Depiction of all particles of the Standard Model, the numbers in the upper left part from top to bottom being mass, charge and spin. For the neutrinos an upper mass limit is shown although the Standard Model assumes them to be massless. Taken from [16].

### Fermions

The Standard Model of particle physics includes 12 fermions. They can be further divided into two groups: Quarks carry colour charge and therefore interact via the strong interaction. They are also electrically charged with fractional elementary charges of  $+2/3e$  or  $-1/3e$ . The positively charged quarks are the up quark (u), the charm quark (c) and the top quark (t). The negatively charged quarks are the down quark (d), the strange quark (s) and the bottom quark (b). Up and down quarks are the building blocks of protons and neutrons and therefore among the main constituents of the world around us.

The other six fermions are called leptons and not carry colour charge. Three of them carry electric charge: The electron (e), the muon ( $\mu$ ) and the tauon ( $\tau$ ). In addition there are three other fermions called neutrinos. The neutrinos ( $\nu$ ) are electrically neutral and interact only via the weak force. Like for the leptons and quarks, there are three generations of neutrinos, the

## 2 Theoretical background

---

electron neutrino ( $\nu_e$ ), the muon neutrino ( $\nu_\mu$ ) and the tauon neutrino ( $\nu_\tau$ ).

Each of the fermions has its antiparticle with the exact same properties, but the opposite charge, e.g. the positron ( $e^+$ ) or the anti-top-quark ( $\bar{t}$ ).

All fermions carry the weak charge and therefore interact via the weak interaction.

### Bosons

In the Standard Model there are gauge bosons and the Higgs boson. The gauge bosons all carry a spin of 1. Photons ( $\gamma$ ) are mediators of the electromagnetic charge and carry no mass or charge themselves.  $W^\pm$  and  $Z^0$  bosons are the carriers of the weak interaction, they have a mass of 80 GeV respectively 91 GeV and differ in charge. The gluon is the massless mediator of the strong interaction. In contrast to the previous bosons, the gluon carries the charge of the strong interaction, the so called colour charge, by itself and can therefore interact with itself.

The final boson is the Higgs boson, the "youngest" particle of the Standard Model in terms of discovery date. The theoretical proposal, however, dates back to 1964, when P. Higgs, the team of F. Englert and R. Brout from Brussels and the team of G. Guralnik, C. Hagen and T.W. Kibble formulated the theory of spontaneous symmetry breaking and the Higgs mechanism (see section 2.1.5). The Higgs boson is massive, has a spin of 0 and carries no charge.

### 2.1.2 Quantum electrodynamics

Quantum electrodynamics (QED) describes the electromagnetic interactions of elementary particles. It is the oldest of the field theories involved with the Standard Model and was developed by Richard Feynman, Julian Schwinger, Shin'ichirō Tomonaga and many others. The Lagrange density of a free fermion must result in the Dirac equation

$$(i\gamma^\mu \partial_\mu - m)\Psi = 0, \quad (2.2)$$

describing the dynamics of a spin 1/2 particle where  $\Psi$  is the wavefunction of the electron and  $\gamma^\mu$  are the Dirac matrices. The Einstein convention is used, implying a summation over identical lower and upper indices. The simplest Lagrange density that yields the Dirac equation when the Euler-Lagrange equation is used, is the following term:

$$\mathcal{L} = i\bar{\Psi}\gamma^\mu \partial_\mu \Psi - m\bar{\Psi}\Psi \quad (2.3)$$

This Lagrange density, however, is not gauge invariant under  $U(1)$  with its local transformation  $\Psi \rightarrow e^{iq\theta(x)}\Psi$  with an arbitrary phase  $\theta(x)$  that is allowed to depend on spacetime and a coupling constant  $q$ . One solution is the introduction of a massless field  $A_\mu$  that cancels the non-gauge invariant terms by construction of its transformation behaviour:  $A_\mu \rightarrow A_\mu - \partial_\mu \theta(x)$ . The field is introduced by replacing the partial derivative  $\partial_\mu$  with  $\partial_\mu + iqA_\mu(x)$ . The full Lagrangian now

reads:

$$\mathcal{L}_{\text{QED}} = \underbrace{i\bar{\Psi}\gamma^\mu\partial_\mu\Psi}_{\text{kinetic term for } \Psi} - \underbrace{\bar{\Psi}\Psi m}_{\text{mass term}} - \underbrace{q\bar{\Psi}\gamma^\mu\Psi A_\mu}_{\text{interaction}} - \underbrace{\frac{1}{4}F^{\mu\nu}F_{\mu\nu}}_{\text{kinetic term for } A} \quad (2.4)$$

where the field strength tensor  $F_{\mu\nu} = \partial_\mu A_\nu - \partial_\nu A_\mu$  has been introduced. The Lagrange density now includes not only a kinematic term for the fermions and a mass term, but also a kinematic term for the electromagnetic field  $A$  and an interaction term between the fermions and the field  $A$ .

### 2.1.3 Quantum chromodynamics

A similar approach to quantum chromodynamics, the field theory for the strong interaction, can be chosen. Replacing the  $U(1)$  symmetry by the  $SU(3)$  symmetry, the local transformation now reads:  $\Psi \rightarrow e^{ig_s\alpha^a(x)T^a}\Psi$ , with  $\alpha^a(x)$  as a set of functions depending on space time,  $T^a$  as a set of linear independent  $3\times 3$  matrices and the generators of  $SU(3)$ , and  $g_s$  as a coupling constant. The common choice for the generators are the Gell-Mann matrices. The same approach as for QED gives a non-gauge invariant Lagrangian that can be fixed by introducing a set of eight vector fields  $G_\mu^a$  which represent the eight gluons. Again, the partial derivative is replaced by  $\partial_\mu + ig_s T^a G_\mu^a$ . This leads to a Lagrangian of the following form:

$$\mathcal{L}_{\text{QCD}} = \underbrace{i\bar{\Psi}^i\gamma^\mu\partial_\mu\Psi_i}_{\text{kinetic term for } \Psi} - \underbrace{\bar{\Psi}^i\Psi_i m}_{\text{mass term}} - \underbrace{g_s\bar{\Psi}^i\gamma^\mu T^a G_\mu^a\Psi_i}_{\text{interaction}} - \underbrace{\frac{1}{4}G_a^{\mu\nu}G_{\mu\nu}^a}_{\text{kinetic+ self interaction term for } G} \quad (2.5)$$

where the index  $i$  indicates the six quark generations which are summed over. Again, an interaction term arises from the requirement of gauge invariance. The field strength tensor  $G_{\mu\nu}^a$  now takes the form:

$$G_{\mu\nu}^a = \partial_\mu G_\nu^a - \partial_\nu G_\mu^a - g_s f^{abc} G_\mu^b G_\nu^c \quad (2.6)$$

where  $f^{abc}$  is defined via the commutator  $[T^a, T^b] = 2if^{abc}T^c$ . The third term corresponds to self interaction of gluons, a major difference to QED, where a photon-photon vertex is not allowed. Another important property arises from the renormalization of the coupling constant. For QCD this renormalization process differs by a minus sign to the renormalization of the other interactions, implying that quarks can only be described as free particles for small ranges. At larger distances, the potential energy between two quarks increases, meaning that free single quarks can not exist. Instead they form colourless hadrons, as for example the neutron, consisting of two down quarks and one up quark, or the proton consisting of two up quarks and one down quark. This observation is called *confinement*, its counterpart, the decreasing potential at small distances, *asymptotic freedom*.

### 2.1.4 Electroweak unification

Similar to QCD and QED, the Lagrangian for the electroweak interaction can be defined. The underlying gauge symmetry is the  $SU(2)_L$  symmetry, the charge is the third component of the weak isospin  $T_3$ . The local gauge transformation for  $SU(2)$  are  $\Psi_L \rightarrow \Psi_L e^{ig\alpha^a(x)T^a}$ , where  $T^a$  are the  $SU(2)$  generators, often represented by the Pauli matrices. One important difference to the previous two interactions poses the fact that the weak interaction couples only to left-handed fermions. This property is known from experimental evidence, most prominently the Wu experiment [17]. The chirality of a fermion is defined via the projection operator  $P_L = \frac{1}{2}(1 - \gamma^5)$  for left-handed and  $P_R = \frac{1}{2}(1 + \gamma^5)$  for right-handed particles. For massless particles the chirality equals the helicity of a particle, defined as its spin projected on its momentum. Particles with their spin and momentum aligned have a positive helicity and a right-handed chirality, for particles with an anti-parallel alignment the helicity is negative and the chirality is left-handed.

The left-handed fermions can be arranged in doublets with upper (lower) components having a weak isospin of  $I_3 = (-)\frac{1}{2}$ :

$$\begin{pmatrix} \nu_e \\ e \end{pmatrix}_L, \begin{pmatrix} \nu_\mu \\ \mu \end{pmatrix}_L, \begin{pmatrix} \nu_\tau \\ \tau \end{pmatrix}_L, \begin{pmatrix} u \\ d' \end{pmatrix}_L, \begin{pmatrix} c \\ s' \end{pmatrix}_L, \begin{pmatrix} t \\ b' \end{pmatrix}_L \quad (2.7)$$

The ' in the lower component of the quarks signals that these are not the mass eigenstates but the flavour eigenstates of the quark. They differ by a rotation defined by the Cabbibo-Kobayashi-Maskawa matrix  $V_{UD}$ :

$$\begin{pmatrix} d' \\ s' \\ b' \end{pmatrix} = V_{UD} \begin{pmatrix} d \\ s \\ b \end{pmatrix} \quad (2.8)$$

If the mass and flavour eigenstates were identical, the matrix would be diagonal. However, the appearing off-diagonal elements imply that the weak interaction allows the change between quark families. According to [18], the exact values of the components of  $V_{UD}$  are:

$$V_{UD} = \begin{pmatrix} 0.97370 \pm 0.00014 & 0.2245 \pm 0.0008 & (3.82 \pm 0.24) \times 10^{-3} \\ 0.221 \pm 0.004 & 0.978 \pm 0.011 & (41.0 \pm 1.4) \times 10^{-3} \\ (8.0 \pm 0.3 \times 10^{-3}) & (38.8 \pm 1.1) \times 10^{-3} & 1.013 \pm 0.030 \end{pmatrix} \quad (2.9)$$

By exchanging a  $W$  boson with its third isospin component of  $T_3 = \pm 1$  it is possible for one particle of the upper component to change to the lower component or vice versa. Using these constraints to construct a Lagrangian, introduce a three dimensional vector field  $W_{\mu\nu}^a$  and define



its transformation laws, the result is:

$$\mathcal{L}_{EW} = \underbrace{i\bar{\Psi}_L\gamma^\mu\partial_\mu\Psi_L}_{\text{kinetic term for } \Psi} - \underbrace{g\bar{\Psi}_L\gamma^\mu T^a W_\mu^a\Psi_L}_{\text{interaction}} - \underbrace{\frac{1}{4}W_a^{\mu\nu}W_{\mu\nu}^a}_{\text{kinetic+ self interaction term for } W} \quad (2.10)$$

Again, self interaction between the newly introduced fields are possible since its field strength tensor is defined as

$$W_{\mu\nu}^a = \partial_\mu W_\nu^a - \partial_\nu W_\mu^a - g\epsilon^{abd}W_\mu^b W_\nu^c \quad (2.11)$$

where  $\epsilon^{abc}$  is the Levi-Civita symbol. Most notably the mass term is missing. A designated mass term in the Lagrangian of the weak interaction would not be invariant under gauge transformation since it would require the left- and right-handed components to transform equally, which is generally not the case. This problem will be solved by the Higgs-mechanism described in section 2.1.5.

The electroweak unification is the combination of the  $U(1)_Y$  and the  $SU(2)_L$  symmetries into one singular theory. The  $U(1)_Y$  symmetry is very similar to QED, the only difference is the use of the hypercharge  $Y = 2(Q - I_3)$ , the coupling constant  $g'$  and the mediator field  $B_\mu$ . Summing up the Lagrange densities for  $U(1)_Y$  and  $SU(2)_L$ , the total Lagrange density takes the form:

$$\begin{aligned} \mathcal{L} = & i\bar{\Psi}_R\gamma^\mu\partial_\mu\Psi_L - g\bar{\Psi}_L\gamma^\mu T^a W_\mu^a\Psi_L - g'\bar{\Psi}_L\gamma^\mu\frac{Y}{2}B_\mu\Psi_L \\ & + i\bar{\Psi}_R\gamma^\mu\partial_\mu\Psi_R - g'\bar{\Psi}_R\gamma^\mu\frac{Y}{2}B_\mu\Psi_R \\ & - \frac{1}{4}W_a^{\mu\nu}W_\mu^a - \frac{1}{4}B^{\mu\nu}B_\mu \end{aligned} \quad (2.12)$$

where a summation over all left-handed doublets and right-handed singlets is implied. Often a short hand notation, the covariant derivative, is introduced  $D_\mu = \partial_\mu + igT^a W_\mu^a + ig'\frac{Y}{2}B_\mu$ , so that the first three terms can be expressed as one. Inserting the Pauli matrices in the  $g\gamma^\mu T^a W_\mu^a$  term, it results in the term:

$$-\frac{g}{2} \begin{pmatrix} W^3 & W^1 - iW^2 \\ W^1 + iW^2 & -W^3 \end{pmatrix}_\mu \quad (2.13)$$

The off-diagonal elements represent a flavour change, which means that the  $W^\pm$  boson can be identified as

$$W^\pm = \frac{1}{\sqrt{2}}(W^1 \mp iW^2) \quad (2.14)$$

In a similar way, the remaining field, namely  $W_\mu^3$  and  $B_\mu$ , can be rotated into the  $Z$  boson and the photon. This is necessary to ensure that the photon field is massless, as shown in section

2.1.5. The rotation angle between the fields is called *Weinberg angle*  $\theta_W$ .

$$\begin{pmatrix} W^3 \\ B \end{pmatrix}_\mu = \begin{pmatrix} \cos(\theta_W) & \sin(\theta_W) \\ -\sin(\theta_W) & \cos(\theta_W) \end{pmatrix} \begin{pmatrix} Z \\ A \end{pmatrix}_\mu \quad (2.15)$$

In the history of physics there are many examples of unifications of theories. Phenomenons that were thought to have different origins turned out to have a common cause. Notable examples include the unification of electrodynamics and magnetodynamics to electromagnetics by Maxwell and Heaviside in the mid 19th century, or the discussed unification of QED and the weak interaction to the electroweak interaction. Naturally, the question arises whether the electroweak interaction and the strong interaction can further be unified to a so called *Grand Unified Theory (GUT)*. All though the theoretical consideration and experimental search for evidences of such a GUT have been performed for several decades, so far no conclusive evidence for or against the existence of a GUT has been found.

### 2.1.5 The Higgs mechanism

The Higgs mechanism postulates a complex scalar field  $\phi$  in the form of a weak isospin doublet:

$$\phi = \frac{1}{\sqrt{2}} \begin{pmatrix} \phi^+ \\ \phi^0 \end{pmatrix} = \begin{pmatrix} \phi_1 + i\phi_2 \\ \phi_3 + i\phi_4 \end{pmatrix} \quad (2.16)$$

Assuming the spin of the doublet is zero and its dynamic therefore governed by the Klein-Gordon equation, its Lagrangian reads:

$$\mathcal{L}_\phi = (D^\mu \phi)^\dagger (D_\mu \phi) - V(\phi) \quad (2.17)$$

where  $D_\mu$  is the covariant derivative defined in the previous section. Note that a potential  $V$  that depends on the Higgs field has been postulated. This Higgs potential takes the form:

$$V(\phi) = \mu^2 |\phi|^2 + \lambda |\phi|^4 \quad (2.18)$$

with  $\lambda > 0$  to ensure vacuum stability. The different shapes of the potential depending on  $\mu$  can be seen in Fig. 2.2. For  $\mu^2 > 0$ , the potential forms a minimum at  $\phi = 0$ . For  $\mu^2 < 0$  it takes the famous "sombbrero" or "Mexican hat" shape. For the latter the minimum now lies at the position:

$$v = \sqrt{\frac{-\mu^2}{\lambda}} \quad (2.19)$$

Instead of a single minimum, the four dimensional potential has a continuous set of degenerated minima. By making a particular choice for the ground state, the symmetry of the system is

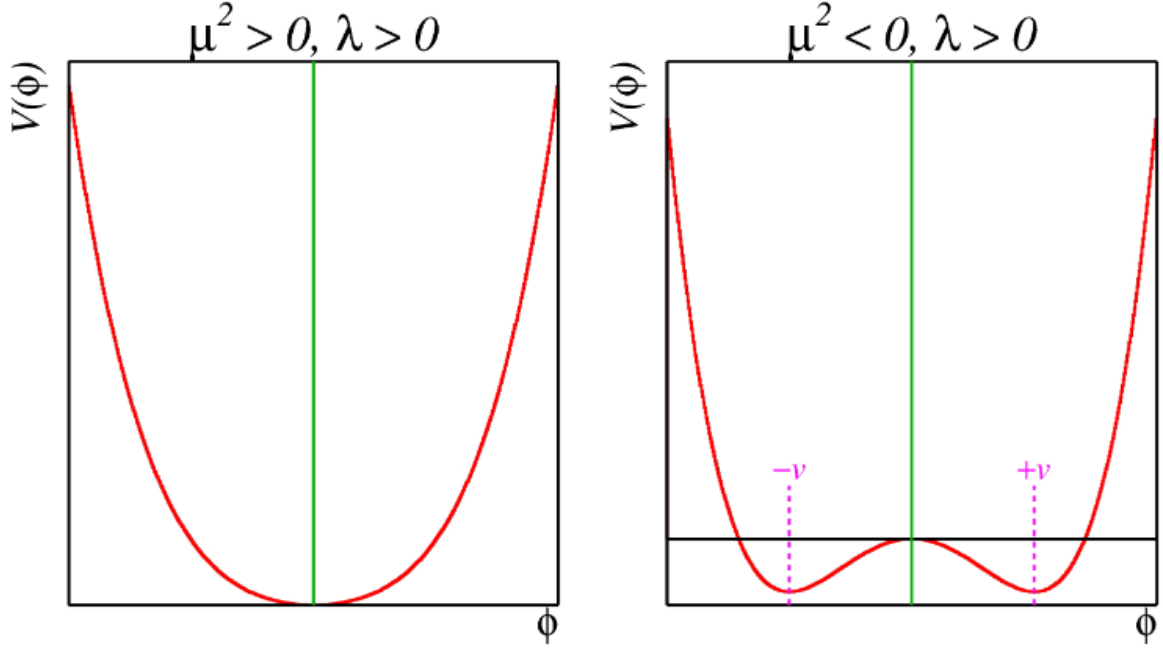


**Figure 2.2** The Higgs potential for positive  $\mu$  (left) and negative  $\mu$  (right). Taken from Ref [19]

broken. By choosing the neutral ground state

$$\phi_{\text{vacuum}} = \frac{1}{\sqrt{2}} \begin{pmatrix} 0 \\ v \end{pmatrix}, \quad (2.20)$$

further calculations can be simplified. All other choices do not change the physical behaviour of the system since they can be transformed by the  $SU(2)$  gauge transformation into the form written above. Now it is possible to develop the field around its minima, by allowing an excitation  $H(x)$ :

$$\phi = \frac{1}{\sqrt{2}} \begin{pmatrix} 0 \\ v + H(x) \end{pmatrix} \quad (2.21)$$

By inserting this relation into equation 2.18, the following terms arise:

$$V = -\mu^2 H^2 + \lambda v H^3 + \frac{1}{4} \lambda H^4 \quad (2.22)$$

The first term can be interpreted as a mass term with  $m_H = \sqrt{-2\mu^2}$ . The second and third terms are the Higgs boson self interaction terms, representing three- and four-Higgs vertices.

By inserting the expanded Higgs doublet into equation 2.17 and rearranging for the gauge

## 2 Theoretical background

---

bosons, one gets the expression:

$$(D^\mu \phi)^\dagger (D_\mu \phi) = \frac{1}{2} (\partial^\mu H) (\partial_\mu H) + \frac{1}{4} g^2 (v+H)^2 W^{+\mu} W_\mu^- + \frac{1}{8} (v+H)^2 \begin{pmatrix} W^{3,\mu} & B^\mu \end{pmatrix} \begin{pmatrix} g^2 & -gg' \\ -gg' & g'^2 \end{pmatrix} \begin{pmatrix} W_\mu^3 \\ B_\mu \end{pmatrix} \quad (2.23)$$

The first term can be interpreted as the kinetic term of the Higgs boson. By multiplying out the  $(v+H)^2$  terms, a variety of interaction terms arise, consisting of all summands including a factor of  $H$  or  $H^2$ . These terms describe the interaction between the gauge bosons and the Higgs boson. But furthermore several terms appear that have the same form as mass terms. Those terms can indeed be interpreted as the masses of the gauge bosons. By reading the prefactors, the mass of the  $W$  bosons can be directly identified with  $m_W^2 = \frac{1}{4} g^2 v^2$ . For the second term, the matrix has to be diagonalised first, resulting in the eigenstates:

$$A_\mu = \frac{gW_\mu^3 + g'B_\mu}{\sqrt{g^2 + g'^2}} \text{ and } Z_\mu = \frac{g'W_\mu^3 - gB_\mu}{\sqrt{g^2 + g'^2}} \quad (2.24)$$

with the corresponding eigenvalues 0 and  $\frac{1}{2} \sqrt{g^2 + g'^2}$ . With this transformation one additional massive gauge boson with  $m_Z^2 = \frac{1}{4} v^2 (g^2 + g'^2)$  and one massless gauge boson are described. These are the  $Z$  boson and the photon, respectively. Comparing the rotation with the Weinberg angle from section 2.1.4, one can express it in terms of the coupling constants:

$$\cos(\theta_W) = \frac{g}{\sqrt{g^2 + g'^2}}. \quad (2.25)$$

This resolves the question how the gauge bosons acquire their mass without adding an explicit mass term: Their interaction with the Higgs field produces dynamically a mass term in the Lagrangian.

With the Higgs boson there is another isospin doublet that can be connected to the fermion doublets in a way that mass terms in the Lagrangian become gauge invariant:

$$\mathcal{L} = -\lambda_f (\bar{\Psi}_L \phi \Psi_R + \Psi_R \phi^\dagger \bar{\Psi}_L) \quad (2.26)$$

By inserting the expansion from equation 2.21 for  $\phi$ , the Lagrangian takes the form:

$$\mathcal{L} = -\lambda_f \frac{v}{\sqrt{2}} (\bar{\Psi}_L \Psi_R + \Psi_R \bar{\Psi}_L) - \lambda_f \frac{H}{\sqrt{2}} (\bar{\Psi}_L \Psi_R + \Psi_R \bar{\Psi}_L) \quad (2.27)$$

This Lagrangian now consists of a mass term and a Yukawa interaction between fermions and the Higgs field:

$$\mathcal{L}_{\text{Fermions}} = -m_f \bar{\Psi}_f \Psi_f - \frac{m_f}{v} H \bar{\Psi}_f \Psi_f \quad (2.28)$$

where the fermion mass in terms of the Yukawa coupling strength  $\lambda_f$  is given by:

$$m_f = \frac{\lambda_f v}{\sqrt{2}}. \quad (2.29)$$

## 2.2 Shortcoming of the Standard Model

Despite its success, there are open questions that remain unanswered by the Standard Model. For this reason it is clear that the Standard Model at least is not complete. The following section gives a brief overview over the most important shortcomings of the Standard Model.

### Gravity

The fourth force of nature, gravity, is not included in the Standard Model. Our current theory of gravity is the general theory of relativity by A. Einstein which has not yet been included in the Standard Model.

### Dark matter and dark energy

The existence of *dark matter* is known from gravitational effects observed by astrophysicists that can not be explained with the visible matter [20]. Dark matter is considered neutral in terms of electromagnetic charge, but massive. No particle of the Standard Model matches with the properties of dark matter, leading to the postulation of new particles beyond the Standard Model. In addition the acceleration of the expansion of the universe requires a yet unknown form of energy called *dark energy*. Around 27% of all matter and 68% of all energy is considered to be dark matter and dark energy [21].

### Matter-antimatter asymmetry

The matter-antimatter asymmetry problem arises from the simple observation that there is more baryonic matter than baryonic anti-matter in the universe. This is an imbalanced, hence unnatural, state and neither the Standard Model nor general relativity can explain this asymmetry. The only way of producing a matter-antimatter asymmetry is by CP violation, but the only mechanism in the Standard Model responsible for CP violation, the weak interaction, is not sufficient to explain the asymmetry [22].

### Hierarchy problem and fine-tuning

While technically not a clear contradiction to the Standard Model, the large discrepancy between the four forces of nature (e.g. gravity is around 24 orders of magnitude weaker than the weak interaction) seems unnatural. The Standard Model does not give an explanation to these

large differences. One result is the unstable Higgs mass  $m_H$  with respect to higher order correction. These corrections result in a quadratically divergent term  $\sim \Lambda^2$  where  $\Lambda$  is the Planck scale at around  $10^{19}$  GeV. In order to cancel these large contributions, the uncorrected Higgs mass  $m_H$  would have to be fine-tuned to the Planck scale. Whether this is in fact the case or whether there is another mechanism cancelling out the quadratic contributions is unknown.

### 2.3 The Two-Higgs-doublet model

The shortcomings explained above gave rise to a variety of extensions of the Standard Model. Those extensions are generally formulated under two paradigms. On one hand their predictions must agree with existing data and verified predictions of the standard model. On the other hand they have to address the imperfections of the Standard Model in a way that answers at least some of the above questions, ideally also predicting results contradicting the Standard Model that can be searched for in experiments. To achieve this, different approaches have been used ranging from the plain extension of the Standard Model (Supersymmetry, Two-Higgs-doublet model) to its complete reinvention (String theory, Loop quantum gravity).

One of the extensions of the Standard Model in the Higgs sector is the Two-Higgs-doublet model (2HDM). The discussion in this chapter follows [23]. The 2HDM adds a second Higgs isospin doublet to the minimal version implemented in the Standard Model:

$$\Phi_1 = \begin{pmatrix} \phi_1^+ \\ \phi_1^0 \end{pmatrix}, \quad \Phi_2 = \begin{pmatrix} \phi_2^+ \\ \phi_2^0 \end{pmatrix} \quad (2.30)$$

All four components are complex numbers in general, resulting in a total of eight real degrees of freedom. Following the logic of the spontaneous symmetry breaking, it immediately becomes evident that adding the second doublet results in a total of five Higgs bosons and three Goldstone bosons.

#### 2.3.1 The 2HDM potential

To understand the nature of the five different Higgs bosons and the meaning of the new free parameters arising from the model, the Lagrangian has to be studied. It consists of a kinetic term and a potential similar in shape as before:

$$\mathcal{L}_{2\text{HDM}} = (D_\mu \Phi_1)^\dagger (D^\mu \Phi_1) + (D_\mu \Phi_2)^\dagger (D^\mu \Phi_2) - V(\Phi_1, \Phi_2) \quad (2.31)$$

with the covariant derivative defined as in section 2.1.4. Analogously to the Standard Model Higgs mechanism, a symmetric quartic potential is assumed. This potential can generally contain all possible two- and four-combinations of the two fields and their complex conjugate. The

most general form therefore can be written as:

$$\begin{aligned}
 V = & m_{11}^2(\phi_1^\dagger\phi_1) + m_{22}^2(\phi_2^\dagger\phi_2) - m_{12}^2(\phi_1^\dagger\phi_2) + h.c. \\
 & + \frac{1}{2}\lambda_1(\phi_1^\dagger\phi_1)^2 + \frac{1}{2}\lambda_2(\phi_2^\dagger\phi_2)^2 + \lambda_3(\phi_1^\dagger\phi_1)(\phi_2^\dagger\phi_2) + \lambda_4(\phi_1^\dagger\phi_2)(\phi_2^\dagger\phi_1) \\
 & + \left[ \frac{1}{2}\lambda_5(\phi_1^\dagger\phi_2)^2 + [\lambda_6(\phi_1^\dagger\phi_1) + \lambda_7(\phi_2^\dagger\phi_2)](\phi_1^\dagger\phi_2) + h.c. \right]
 \end{aligned} \tag{2.32}$$

This potential introduces the real parameters  $m_{11}, m_{22}, \lambda_1, \lambda_2, \lambda_3, \lambda_4$  and the complex parameters  $m_{12}, \lambda_5, \lambda_6, \lambda_7$  resulting in a total of  $6 + 2 \cdot 4 = 14$  degrees of freedom for the potential.

It should be emphasized that although their naming implies otherwise the parameters  $m_{ij}$  are not masses in a classical sense. To obtain the masses of the physical Higgs bosons a rotation between the doublets has to be performed.

There are several empirically motivated constraints one can demand, which reduce the number of degrees of freedom significantly:

- The absence of flavor-changing neutral currents (FCNC) at tree level
- CP conservation

To ensure the absence of FCNC, an additional  $\mathbb{Z}_2$  symmetry must be imposed to ensure that the interactions with the Z boson are still flavour diagonal as in the Standard Model. For a rigorous proof see Ref. [24]. The  $\mathbb{Z}_2$  symmetry implies that the parameters  $\lambda_6$  and  $\lambda_7$  are equal to zero. The potential is CP conserving if and only if a basis can be found in which all parameters are real [25]. This condition renders  $m_{12}$  and  $\lambda_5$  real and reduces the total number of degrees of freedom to 8. The potential now reads:

$$\begin{aligned}
 V = & m_{11}^2(\phi_1^\dagger\phi_1) + m_{22}^2(\phi_2^\dagger\phi_2) - m_{12}^2(\phi_1^\dagger\phi_2) + h.c. \\
 & + \frac{1}{2}\lambda_1(\phi_1^\dagger\phi_1)^2 + \frac{1}{2}\lambda_2(\phi_2^\dagger\phi_2)^2 + \lambda_3(\phi_1^\dagger\phi_1)(\phi_2^\dagger\phi_2) + \lambda_4(\phi_1^\dagger\phi_2)(\phi_2^\dagger\phi_1) \\
 & + \frac{1}{2}\lambda_5 \left[ (\phi_1^\dagger\phi_2)^2 + (\phi_2^\dagger\phi_1)^2 \right]
 \end{aligned} \tag{2.33}$$

It is further demanded that both doublets develop a vacuum expectation value in their lower (neutral) component marking the minimum of the Higgs potential. The existence of such a minimum is generally non-trivial for the 2HDM. However, calculations show that under some assumptions the minimum always exists and is stable [26]. By convention the two vacuum expectation values are denoted as:

$$\langle \Phi_1 \rangle_0 = \langle 0 | \Phi_1 | 0 \rangle = \frac{1}{\sqrt{2}} \begin{pmatrix} 0 \\ v_1 \end{pmatrix}, \quad \langle \Phi_2 \rangle_0 = \langle 0 | \Phi_2 | 0 \rangle = \frac{1}{\sqrt{2}} \begin{pmatrix} 0 \\ v_2 \end{pmatrix} \tag{2.34}$$

## 2 Theoretical background

---

The fields of the two doublets can now be developed around the ground state:

$$\Phi_1 = \frac{1}{\sqrt{2}} \begin{pmatrix} \sqrt{2}\phi_1^+ \\ v_1 + \rho_1 + i\eta_1 \end{pmatrix}, \Phi_2 = \frac{1}{\sqrt{2}} \begin{pmatrix} \sqrt{2}\phi_2^+ \\ v_2 + \rho_2 + i\eta_2 \end{pmatrix} \quad (2.35)$$

The excitations of the fields around this minimum can be interpreted as the different physical Higgs particles. The excitations of the fields  $\phi_i^+$  represent the charged Higgs bosons. Its isospin  $I_3$  is 0.5, while the hypercharge is equal to 1 by construction. To calculate the electrical charge, the Gell-Mann-Nishijima formula can be used:

$$Q = I_3 + \frac{1}{2}Y \quad (2.36)$$

This yields a charge of 1 for the upper components and 0 for the lower parts.

The fields  $\rho_i$  are the real valued perturbations of the ground state and therefore comparable to the Standard Model Higgs bosons. They are electrically neutral and CP-even.

The fields  $\eta_i$  on the other hand are the imaginary perturbations from the ground state resulting in the neutral CP-odd Higgs boson.

This gives a total of five Higgs bosons, two of which are charged, two CP even and one CP odd.

For the analysis of this thesis, the masses of the Higgs bosons in terms of the parameters of the Higgs potential have to be obtained to correctly configure the simulation tool described in section 6.1.1. In the following paragraphs the corresponding basis transformation laws from the generic to the physical mass basis will be derived based on the derivation of the transformation laws between other 2HDM basis in [27] and [28].

The two doublets from equation (2.35) have to be substituted in (2.33). Ignoring all terms that



are cubic and quartic in the fields, this yields:

$$\begin{aligned}
 V = & \eta_1 \left( m_{11}^2 + \lambda_1 \frac{v_1^3}{2} - v_2 (m_{12} - \lambda_3 + \lambda_4 + \lambda_5 \frac{v_1 v_2}{2}) \right) \\
 & + \eta_2 \left( m_{22}^2 + \lambda_2 \frac{v_2^3}{2} - v_1 (m_{12} - \lambda_3 + \lambda_4 + \lambda_5 \frac{v_1 v_2}{2}) \right) \\
 & + \frac{1}{2} \left[ m_{11}^2 (2\phi_1^+ \phi_1^- + \rho_1^\dagger \rho_1 + \eta_1^\dagger \eta_1) + m_{22}^2 (2\phi_2^+ \phi_2^- + \rho_2^\dagger \rho_2 + \eta_2^\dagger \eta_2) \right. \\
 & \quad \left. - m_{12}^2 (2\phi_1^+ \phi_2^- + 2\phi_2^+ \phi_1^- + \rho_2^\dagger \rho_1 + \rho_1^\dagger \rho_2 + \eta_2^\dagger \eta_1 + \eta_1^\dagger \eta_2) \right. \\
 & \quad \left. + \lambda_1 \left( \frac{3}{4} v_1^2 \rho_1^\dagger \rho_1 + \frac{1}{2} v_1^2 \eta_1^\dagger \eta_1 + v_1^2 \phi_1^+ \phi_1^- \right) + \lambda_2 \left( \frac{3}{4} v_2^2 \rho_2^\dagger \rho_2 + \frac{1}{2} v_2^2 \eta_2^\dagger \eta_2 + v_2^2 \phi_2^+ \phi_2^- \right) \right. \\
 & \quad \left. + \lambda_3 \left( \frac{v_2^2}{2} \rho_1^\dagger \rho_1 + \frac{v_1^2}{2} \rho_2^\dagger \rho_2 + v_1 v_2 (\rho_1^\dagger \rho_2 + \rho_2^\dagger \rho_1) + \frac{v_2^2}{2} \eta_1^\dagger \eta_1 + \frac{v_1^2}{2} \eta_2^\dagger \eta_2 + v_2^2 \phi_1^+ \phi_1^- + v_1^2 \phi_2^+ \phi_2^- \right) \right. \\
 & \quad \left. + \lambda_4 \left( \frac{v_2^2}{2} \rho_1^\dagger \rho_1 + \frac{v_1^2}{2} \rho_2^\dagger \rho_2 + v_1 v_2 (\rho_1^\dagger \rho_2 + \rho_2^\dagger \rho_1) + \frac{v_2^2}{2} \eta_1^\dagger \eta_1 + \frac{v_1^2}{2} \eta_2^\dagger \eta_2 + v_1 v_2 (\phi_1^+ \phi_2^- + \phi_2^+ \phi_1^-) \right) \right. \\
 & \quad \left. + \lambda_5 \left( \frac{v_2^2}{2} \rho_1^\dagger \rho_1 + \frac{v_1^2}{2} \rho_2^\dagger \rho_2 + v_1 v_2 (\rho_1^\dagger \rho_2 + \rho_2^\dagger \rho_1) - \frac{v_2^2}{2} \eta_1^\dagger \eta_1 - \frac{v_1^2}{2} \eta_2^\dagger \eta_2 + v_1 v_2 (\eta_1^\dagger \eta_2 + \eta_2^\dagger \eta_1) \right. \right. \\
 & \quad \left. \left. + v_1 v_2 (\phi_1^+ \phi_2^- + \phi_2^+ \phi_1^-) \right) \right] + \mathcal{O}(f^3) \\
 & \quad f \in \{\eta_i, \rho_i, \phi_i\}
 \end{aligned} \tag{2.37}$$

The first two terms linear in  $\eta$  represent the tadpole diagrams. These are one-loop Feynman diagrams with one external leg, reminiscent of a tadpole. However, two minimization conditions can be used in the case of CP-conservation. Those two equations follow from the form of the potential as shown in Ref. [29] and make the tadpole terms vanish:

$$m_{11}^2 = \frac{v_2}{v_1} m_{12}^2 - \frac{1}{2} \lambda_1 v_1^2 - \frac{1}{2} (\lambda_3 + \lambda_4 + \lambda_5) v_2^2 \tag{2.38}$$

$$m_{22}^2 = \frac{v_1}{v_2} m_{12}^2 - \frac{1}{2} \lambda_2 v_2^2 - \frac{1}{2} (\lambda_3 + \lambda_4 + \lambda_5) v_1^2 \tag{2.39}$$

The quadratic terms on the other hand can be rearranged and sorted by the fields:

$$V = \frac{1}{2} \left[ \begin{pmatrix} \eta_1 \\ \eta_2 \end{pmatrix}^\dagger M_\eta \begin{pmatrix} \eta_1 \\ \eta_2 \end{pmatrix} + \begin{pmatrix} \rho_1 \\ \rho_2 \end{pmatrix}^\dagger M_\rho \begin{pmatrix} \rho_1 \\ \rho_2 \end{pmatrix} + \begin{pmatrix} \phi_1^- \\ \phi_2^- \end{pmatrix}^\dagger M_\phi \begin{pmatrix} \phi_1^- \\ \phi_2^- \end{pmatrix} \right] \tag{2.40}$$

where the mass matrices are:

$$M_\eta = \begin{pmatrix} m_{11}^2 + \lambda_1 \frac{v_1^2}{2} + \lambda_{34-5} \frac{v_2^2}{2} & -m_{12}^2 + \lambda_5 v_1 v_2 \\ -m_{12}^2 + \lambda_5 v_1 v_2 & m_{22}^2 + \lambda_2 \frac{v_1^2}{2} + \lambda_{34-5} \frac{v_2^2}{2} \end{pmatrix} \tag{2.41}$$

$$M_\rho = \begin{pmatrix} m_{11}^2 + 3\lambda_1 \frac{v_1^2}{2} + \lambda_{345} \frac{v_2^2}{2} & -m_{12}^2 + \lambda_{345} v_1 v_2 \\ -m_{12}^2 + \lambda_{345} v_1 v_2 & m_{22}^2 + 3\lambda_2 \frac{v_1^2}{2} + \lambda_{345} \frac{v_2^2}{2} \end{pmatrix} \tag{2.42}$$

## 2 Theoretical background

$$M_\phi = \begin{pmatrix} 2m_{11}^2 + \lambda_1 v_1^2 + \lambda_3 v_2^2 & -2m_{12}^2 + \lambda_{45} v_1 v_2 \\ -2m_{12}^2 + \lambda_{45} v_1 v_2 & 2m_{22}^2 + \lambda_2 v_2^2 + \lambda_3 v_1^2 \end{pmatrix} \quad (2.43)$$

using the short hand notation  $\lambda_{ij-k\dots} = \lambda_i + \lambda_j - \lambda_k + \dots$

With the help of equations 2.38 and 2.39 one can eliminate  $m_{11}$  and  $m_{22}$  from the matrices:

$$M_\eta = \begin{pmatrix} \frac{v_2}{v_1} m_{12}^2 - \lambda_5 v_2^2 & -m_{12}^2 + \lambda_5 v_1 v_2 \\ -m_{12}^2 + \lambda_5 v_1 v_2 & \frac{v_1}{v_2} m_{12}^2 - \lambda_5 v_1^2 \end{pmatrix} \quad (2.44)$$

$$M_\rho = \begin{pmatrix} \frac{v_2}{v_1} m_{12}^2 + \lambda_1 v_1^2 & -m_{12}^2 + \lambda_{345} v_1 v_2 \\ -m_{12}^2 + \lambda_{345} v_1 v_2 & \frac{v_1}{v_2} m_{12}^2 + \lambda_2 v_2^2 \end{pmatrix} \quad (2.45)$$

$$M_\phi = \begin{pmatrix} 2\frac{v_2}{v_1} m_{12}^2 - \lambda_{45} v_2^2 & -2m_{12}^2 + \lambda_{45} v_1 v_2 \\ -2m_{12}^2 + \lambda_{45} v_1 v_2 & 2\frac{v_2}{v_1} m_{12}^2 - \lambda_{45} v_1^2 \end{pmatrix} \quad (2.46)$$

The matrices above are the equivalent to the prefactor  $-\mu^2$  from the Standard Model Higgs mechanism in section 2.1.5. This matrix appearance of the prefactors in a two dimensional model is natural. Still, an obvious problem arises from the fact that the choice of basis is arbitrary, which results in the non-diagonal form above: To obtain the masses of the new Higgs bosons, the three matrices have to be diagonalized. This can be done by finding their eigenvalues. The eigenvalues of a matrix  $A$  can be calculated with the zeros of its characteristic polynomial:

$$\det(A - \mathbb{I} \cdot x) \stackrel{!}{=} 0 \quad (2.47)$$

Hence for  $M_\eta$  we get:

$$\begin{aligned} \det \begin{pmatrix} \frac{v_2}{v_1} m_{12}^2 - \lambda_5 v_2^2 - x & -m_{12}^2 + \lambda_5 v_1 v_2 \\ -m_{12}^2 + \lambda_5 v_1 v_2 & \frac{v_1}{v_2} m_{12}^2 - \lambda_5 v_1^2 - x \end{pmatrix} &= x^2 - x \left( \frac{v_2}{v_1} m_{12}^2 - \lambda_5 v_2^2 + \frac{v_1}{v_2} m_{12}^2 - \lambda_5 v_1^2 \right) \\ &+ (m_{12}^4 + \lambda_5^2 v_1^2 v_2^2 - 2v_2 v_1 m_{12}^2 \lambda_5) - (m_{12}^4 + \lambda_5^2 v_1^2 v_2^2 - 2\lambda_5 m_{12}^2 v_1 v_2) \stackrel{!}{=} 0 \\ &\Rightarrow \begin{cases} x_1 = 0 \\ x_2 = m_{12}^2 \frac{v_2^2 + v_1^2}{v_1 v_2} - \lambda_5 (v_1^2 + v_2^2) \end{cases} \end{aligned}$$

which are the diagonal elements of the mass matrix for the fields  $\eta_i$ . One of them is 0, which corresponds to the massless neutral Goldstone boson, the origin of the Z mass.

The other mass term corresponds to the squared mass of the CP-odd Higgs boson  $A$ . By changing into polar coordinates with  $v^2 = v_1^2 + v_2^2$ ,  $v_1 = v \cos(\beta)$  and  $v_2 = v \sin(\beta)$  the final expres-

sion of  $m_A$  is:

$$m_A^2 = \frac{m_{12}^2}{\sin(\beta)\cos(\beta)} - \lambda_5 v \quad (2.48)$$

The same procedure can be applied to the third matrix  $M_\phi$ . Again, one of its eigenvalues is 0 corresponding to the two massless, but charged Goldstone bosons. These charged Goldstone bosons result in the mass of the  $W^\pm$ . The other eigenvalue and therefore the mass of the charged Higgs bosons is:

$$m_{H^\pm}^2 = \frac{m_{12}^2}{\sin(\beta)\cos(\beta)} - \frac{\lambda_{45}v}{2} \quad (2.49)$$

The matrix  $M_\rho$  is more difficult to diagonalize because the constant terms do not cancel, meaning there is no eigenvalue equal to zero:

$$\begin{aligned} \det(M_\phi - \mathbb{I} \cdot x) &= x^2 + x(m_{12}^2 \frac{v_1}{v_2} + m_{12}^2 \frac{v_2}{v_1} + \lambda_1 v_1^2 + \lambda_2 v_2^2) \\ &+ m_{12}^2 + m_{12}^2 \frac{v_1^3}{v_1} + m_{12}^2 \frac{v_2^3}{v_2} + \lambda_1^2 v_1 \lambda_2 v_2^2 - (m_{12}^4 - m_{12}^2 \lambda_{345} v_1 v_2 + \lambda_{345}^2 v_1^2 v_2^2) \\ &\Rightarrow x_{1,2} = -\frac{m_{12}^2 \frac{v_1}{v_2} + m_{12}^2 \frac{v_2}{v_1} + \lambda_1 v_1^2 + \lambda_1 v_2^2}{2} \\ &\pm \sqrt{\left[ \frac{(m_{12}^2 \frac{v_1}{v_2} + m_{12}^2 \frac{v_2}{v_1} + \lambda_1 v_1^2 + \lambda_2 v_2^2)}{2} \right]^2 - q} \\ q &= +m_{12}^2 + m_{12}^2 \frac{v_1^3}{v_1} + m_{12}^2 \frac{v_2^3}{v_2} + \lambda_1 \lambda_2 v_1^2 v_2^2 - (m_{12}^4 - m_{12}^2 \lambda_{345} v_1 v_2 + \lambda_{345}^2 v_1^2 v_2^2) \end{aligned} \quad (2.50)$$

However, these relations can be dramatically simplified by introducing the rotational angle  $\alpha$ . This is the angle by which the diagonal basis is rotated with respect to the original one, or in other words: it is the angle of the rotational matrix that diagonalizes  $M_\rho$ :

$$\begin{pmatrix} \cos(\alpha) & \sin(\alpha) \\ -\sin(\alpha) & \cos(\alpha) \end{pmatrix} M_\rho \begin{pmatrix} \cos(\alpha) & -\sin(\alpha) \\ \sin(\alpha) & \cos(\alpha) \end{pmatrix} = \begin{pmatrix} m_H & 0 \\ 0 & m_h \end{pmatrix} \quad (2.51)$$

This relation results in a total of four equations. Two equivalent equations will give rise to a definition of  $\alpha$  in terms of the known parameters:

$$\begin{aligned} &-\sin(\alpha)\cos(\alpha)\left(\frac{v_2}{v_1}m_{12}^2 + \lambda_1 v_1^2\right) - \sin(\alpha)^2(m_{12}^2 + \lambda_{345}) \\ &+ \cos(\alpha)\sin(\alpha)\left(\frac{v_1}{v_2}m_{12}^2 + \lambda_2 v_2^2\right) + \cos(\alpha)^2(m_{12}^2 + \lambda_{345}) = 0 \end{aligned} \quad (2.52)$$

Rearranging and simplifying with trigonometric addition and multiplication laws, this yields:

$$\frac{\sin(\beta - \alpha)}{\sin(\beta)\cos(\beta)} m_{12}^2 = \frac{v^2}{2} \left[ \sin(2\alpha) \left( -\cos(\beta)^2 \lambda_1 + \sin(\beta)^2 \lambda_2 \right) + \cos(2\alpha) \sin(2\beta) \lambda_{345} \right] \quad (2.53)$$

## 2 Theoretical background

Similarly, the other two equations can be obtained from the matrix relation. They represent the masses of the two CP-even Higgs bosons in terms of  $\alpha$ :

$$m_H^2 = \frac{\sin(\alpha - \beta)^2}{\sin(\beta) \cos(\beta)} m_{12}^2 + v^2 \left[ \cos(\beta)^2 \cos(\alpha)^2 \lambda_1 + \sin(\beta)^2 \sin(\alpha)^2 \lambda_2 + \frac{\sin(2\alpha) \sin(2\beta) \lambda_{345}}{2} \right] \quad (2.54)$$

$$m_h^2 = \frac{\cos(\alpha - \beta)^2}{\sin(\beta) \cos(\beta)} m_{12}^2 + v^2 \left[ \cos(\beta)^2 \sin(\alpha)^2 \lambda_1 + \sin(\beta)^2 \cos(\alpha)^2 \lambda_2 - \frac{\sin(2\alpha) \sin(2\beta) \lambda_{345}}{2} \right] \quad (2.55)$$

It turns out that applying the same technique for the first two matrices and determining their rotational angle will not result in a new parameter but rather gives  $\beta$  from the earlier definition of it being the the arctan( $\frac{v_2}{v_1}$ ). So the three mass eigenstates are:

$$\begin{pmatrix} \rho_1 \\ \rho_2 \end{pmatrix} = R(\alpha) \begin{pmatrix} H \\ h \end{pmatrix}, \quad \begin{pmatrix} \eta_1 \\ \eta_2 \end{pmatrix} = R(\beta) \begin{pmatrix} \eta \\ A \end{pmatrix}, \quad \begin{pmatrix} \phi_1 \\ \phi_2 \end{pmatrix} = R(\beta) \begin{pmatrix} \phi \\ H^+ \end{pmatrix} \quad (2.56)$$

A brief recap of what has been done so far: writing down the potential of the 2HDM results in 14 degrees of freedom, which can be reduced to 8 by imposing CP conservation and the absence of FCNC. Those 8 parameters plus the two vacuum expectation values  $v_1$  and  $v_2$  is often referred to as the generic basis:  $\{\lambda_1, \lambda_2, \lambda_3, \lambda_4, \lambda_5, m_{11}, m_{22}, m_{12}, v_1, v_2\}$

Using the two relations 2.38, 2.39 and further the results 2.48, 2.49, 2.54 and 2.55, two parameters can be eliminated and the rest expressed in terms of the Higgs boson masses and other parameters:  $\{m_A, m_{H^\pm}, m_H, m_h, \lambda_5, \alpha, \beta, v\}$ . This is often called the physical mass basis.

By inverting the equations above the following back transformations have been calculated:

$$\lambda_1 = \frac{1}{\cos(\beta)^2 v^2} \left( \cos(\alpha)^2 m_H^2 + \sin(\alpha)^2 m_h^2 - \sin(\beta)^2 (m_A^2 + \lambda_5 v^2) \right) \quad (2.57a)$$

$$\lambda_2 = \frac{1}{\sin(\beta)^2 v^2} \left( \cos(\alpha)^2 m_h^2 + \sin(\alpha)^2 m_H^2 - \cos(\beta)^2 (m_A^2 + \lambda_5 v^2) \right) \quad (2.57b)$$

$$\lambda_3 = \frac{\sin(2\alpha)}{\sin(2\beta) v^2} (m_H^2 - m_h^2) - \frac{1}{v^2} (m_A^2 - 2m_{H^\pm}) - \lambda_5 \quad (2.57c)$$

$$\lambda_4 = \frac{2m_A^2 - 2m_{H^\pm}^2}{v^2} + \lambda_5 \quad (2.57d)$$

$$m_{12} = \sqrt{\cos(\beta) \sin(\beta) (m_A^2 + \lambda_5 v^2)} \quad (2.57e)$$

### 2.3.2 Interaction with fermions

Just like in the Standard Model the interactions between the Higgs bosons and the fermions are described by a Yukawa term in the Lagrangian. The general Yukawa part of the Lagrangian in the physical mass basis notation from Ref.[30] reads as follows:

$$\begin{aligned} \mathcal{L}_{\text{Yukawa}} = & - \sum_{f=u,d,l} \left( \frac{m_f}{v} \xi_h^f \bar{f} f h + \xi_H^f \bar{f} f H - i \xi_A^f \bar{f} \gamma_5 f A \right) \\ & - \left[ \frac{\sqrt{2} V_{ud}}{v} \bar{u} (m_u \xi_A^u P_L + m_d \xi_A^d P_R) d H + \frac{\sqrt{2} m_l \xi_A^l}{v} \bar{\nu}_L l_R H^+ + h.c \right] \end{aligned} \quad (2.58)$$

Here,  $f$  denotes the different fermion categories (up-type quarks, down-type quarks and leptons),  $\nu_L$  ( $l_R$ ) denote the neutrinos (leptons),  $P_L$  and  $P_R$  denote the projection operators and  $\xi$  denotes the coupling constants for the respective interaction.

At this point a fundamental choice has to be made: Which one of the two doublets couples to which family?

There are four different schemes to match each class of fermions to exactly one doublet. The coupling of two doublets to the same class of fermions generally results in FCNC. An overview over all possibilities can be found in Table 1. The following classifications are taken from Ref. [23].

**Table 1** Different Types of 2HDMs based on their couplings to different kinds of fermions.

Type	up-type quarks ( $u_i$ )	down-type quarks ( $d_i$ )	charged leptons ( $l_i$ )
Type I	$\phi_2$	$\phi_2$	$\phi_2$
Type II	$\phi_2$	$\phi_1$	$\phi_1$
Lepton-specific	$\phi_2$	$\phi_2$	$\phi_1$
Flipped	$\phi_2$	$\phi_1$	$\phi_2$

In the type I model charged fermions couple to one doublet solely. It has been discussed in the early stages of 2HDM research history and has been used in more general analysis. However, it is rarely analysed in recent papers.

The type II model is arguably the most studied model. Different supersymmetric and Peccei-Quinn models all require an extended Higgs sector of type II, therefore this thesis will focus on the type II model, where the down-type quarks and the leptons couple to the same doublet.

In the lepton-specific model one doublet couples to the two quark families and the other one to the leptons. Many aspects are similar to the type I model, except for the behaviour of the charged Higgs bosons. The lepton specific model has recently been discussed in the context of dark matter and neutrino mass [31].

The flipped model is similar to the type II model, as only the couplings to the two quark families

## 2 Theoretical background

are switched. For  $\tan(\beta) = 1$  the branching ratios are identical to the type II model. When deviating from that value, the coupling will show a behaviour with respect to  $\tan(\beta)$  inverse to the type II model.

Inserting the original Higgs doublets with their respective rotation matrix defined in equation 2.56 into equation 2.58, one obtains the values for the fermion-Higgs boson coupling constants  $\xi_y^x$ , where  $x$  denotes the fermion class (up, down, lepton) and  $y$  denotes the Higgs boson ( $H, A, h$ ). They are listed in Table 2.

**Table 2** The different coupling constants for a type II 2HDM

$\xi_h^u$	$\frac{\cos(\alpha)}{\sin(\beta)}$	$\xi_h^d$	$-\frac{\sin(\alpha)}{\cos(\beta)}$	$\xi_h^l$	$-\frac{\sin(\alpha)}{\cos(\beta)}$
$\xi_H^u$	$\frac{\sin(\alpha)}{\sin(\beta)}$	$\xi_H^d$	$\frac{\cos(\alpha)}{\cos(\beta)}$	$\xi_H^l$	$\frac{\cos(\alpha)}{\cos(\beta)}$
$\xi_A^u$	$\cot(\beta)$	$\xi_A^d$	$\tan(\beta)$	$\xi_A^l$	$\tan(\beta)$
AVV	0	HVV	$SM * \cos(\beta - \alpha)$	hVV	$SM * \sin(\beta - \alpha)$

In the last row of Table 2 the couplings between the Higgs bosons  $A, H, h$  and vector bosons  $V$  are listed according to [23]. They are universal for every type.

To achieve Standard Model like couplings of one of the CP-even Higgs bosons, either  $\cos(\alpha - \beta)$  or  $\sin(\alpha - \beta)$  has to be 1.

In the first case this would mean that the  $H$  could be identified with the Standard Model Higgs boson at 125 GeV. Since  $m_H > m_h$ , a new Higgs boson lighter than the discovered one had to exist. This however constrains the parameter space significantly because in many regions it would have already been discovered. Therefore, analysis of the first case is uncommon today.

The second choice leads to the so called alignment limit. In it  $\sin(\alpha - \beta) \rightarrow 1$ , and therefore,  $\cos(\alpha - \beta) \rightarrow 0$ . In this alignment limit  $h$  can be identified with the Standard Model Higgs, implying the existence of a heavier Higgs boson at  $m_H > 125$  GeV. This analysis has been carried out in the alignment limit, meaning that the Standard Model Higgs boson is the lightest of all Higgs bosons.

### 2.4 Previous 2HDM searches

For the heavy Higgs bosons  $A$  and  $H$  there are different possible decay channels. In addition to the decay into leptons or quarks, the decay to another Higgs boson and a  $Z$  boson is also possible. Furthermore, the decay into two bosons (e.g.  $hh, gg$  or  $\gamma\gamma$ ) is possible. In the last years several searches for additional Higgs bosons have been performed in those channels at the LHC, the LEP and Tevatron. The data so far does not show any evidence of additional 2HDM-like

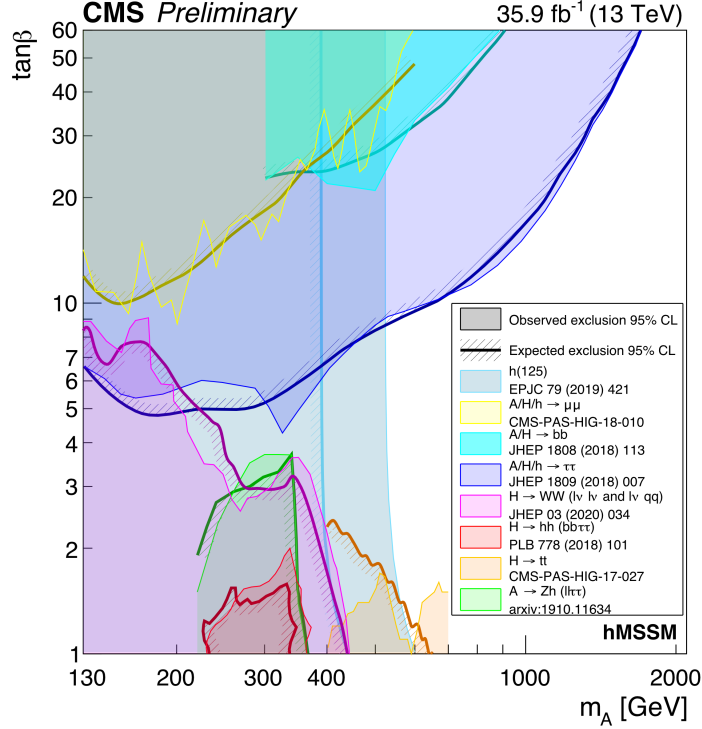


**Figure 2.3** Observed and expected 95% CL upper limits for  $m_A$  and  $\tan(\beta)$  at 13 TeV. Taken from [36].

Higgs bosons. An overview over the excluded regions can be found in Fig. 2.3. An explanation of the observed flavour anomalies [32] and the result of the  $g-2$  experiment [33] might also be possible within the framework of 2HDMs which would result in further constraints of the parameter space [34], [35]. In this section, a brief overview of recent searches in various decay channels is given.

### Decay scenario $A \rightarrow ZH$

At masses below the threshold for a decay into top quarks the decay into a  $Z$  boson and a heavy Higgs boson  $H$ . For this decay channel the mass difference between  $A$  and  $H$  must be at least  $m_Z$ . Some of the 2HDM models imply a different mass hierarchy resulting in the decay channel  $A \rightarrow ZH$ . In this channel many different studies have been performed over the years. The CMS collaboration published several searches (at  $\sqrt{s} = 8$  TeV [37] and  $\sqrt{s} = 13$  TeV [38]), probing the channel  $H \rightarrow ZA(b\bar{b}$  or  $\tau\tau$ ). The limits for this search can be seen in Fig. 2.4. At the ATLAS collaboration a similar search has been performed at  $\sqrt{s} = 13$  TeV [39]. Depending on the  $\tan(\beta)$  value, masses up to 400 GeV have been excluded. The regions of higher masses where the top decay channel opens up can not be excluded with either analysis. The analysis presented in this thesis will provide an extension to the higher mass regions where the previous searches only have a limited sensitivity

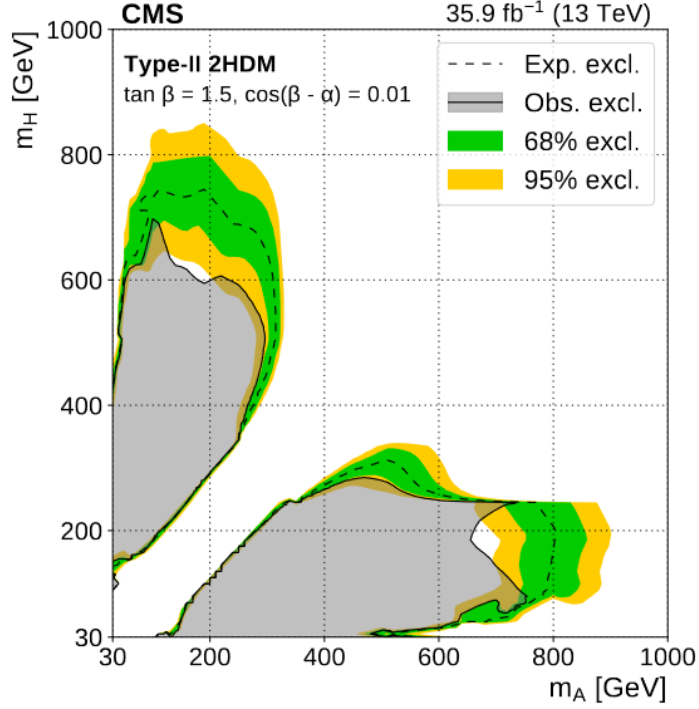


**Figure 2.4** Observed and expected 95% CL upper limits for  $m_A$  and  $\tan(\beta)$  at 13 TeV for the decay channel  $A \rightarrow ZH \rightarrow \ell\ell b\bar{b}$ . Taken from [38].

### Decay scenario $A \rightarrow Zh$

Another possible decay mode is the decay into a  $Z$  boson and a SM like Higgs boson. For this channel the lower boundary is the sum of the masses of the standard model Higgs and the  $Z$  boson. On the other hand there is again the problem of the rising branching ratio for the decay into a pair of top quarks, impeding the exclusion of heavier regions. Overall this results in a comparably small range of the parameter space that can effectively be excluded.

This search has been performed by the ATLAS collaboration at 8 TeV [40] and 13 TeV [41] and also by CMS at 8 TeV [42] and 13 TeV [43]. Depending on the luminosity and the choice of parameters masses up to  $m_A = 380$  GeV have been excluded.

### Decay scenario $A/H \rightarrow t\bar{t}$

At higher masses the decay into top quarks becomes the most important concurrence process to the  $ZH$  decay. This channel opens up at a mass of around  $m_{H/A} = 350$  GeV, when a pair of top quarks can be produced on-shell. This allows the examination of higher mass regions. However, due to the rather unspecific signature of this channel, the distinction between signal and background is a challenging task. One previous search for 2HDM bosons and other physics



beyond the standard model has been performed by CMS [44]. The regions 350-360 GeV for scalar and 350-410 GeV for pseudoscalar bosons have been excluded by this analysis. Another search at ATLAS [45] in the same channel does not mention 2HDMs explicitly, but should also be sensitive to them.

### Decay scenario $A/H \rightarrow b\bar{b}$

Similar to the decay into top quarks, a decay into bottom quarks is also possible. Since the top quark is more than 40 times heavier than the bottom quark, this decay channel is minor, if the coupling to down-type like quarks is not directly enhanced by a high value of  $\tan(\beta)$ . Therefore only at high values of  $\tan(\beta)$  or at lower masses beneath the threshold of  $2m_t$ , noteworthy exclusion can be achieved. A CMS search in this channel [46] obtains limits of  $m_A = 300$  GeV at  $\tan(\beta) = 25$ .

### Decay scenario $A/H \rightarrow l^+l^-$

The decay into leptons is minor in nearly all of the parameter space. For low Higgs boson masses the decay into a pair of tauons can be observed. Their measurement however results in large uncertainties. One search in the tau channel by CMS [47] reports exclusion limits of  $m_H = 250$  GeV at  $\tan(\beta) = 6$ .

The branching fraction of the muonic decay channel is around 300 times smaller than the one for the tau decay. Still, there has been a search with CMS data [48] in this channel as the muon momentum resolution of CMS is significantly better than for taus.

## 2.5 The physics of collider experiments

Since the simulated data used in this thesis comes from proton-proton collision, a brief overview over the physics of this process will be given in this section.

The proton itself is not a fundamental particle, but it consists of quarks held together by the strong force. Protons consist of two up and one down quark. These three quarks are called *valence quarks*. Further quarks can be found in the proton, the short living *sea quarks*. Since there is a continuous exchange of gluons in the proton, these gluons can produce quark-antiquark pairs which then annihilate to a gluon again. These quarks can be of any flavour, not being limited to up or down. Gluons, valence and sea quarks in a proton are collectively called *partons*.

When colliding protons, the individual partons interact, each carrying only a fraction  $x$  of the proton's momentum. Therefore the centre of mass energy of parton-parton collisions varies, even for constant energies of the protons:

$$\sqrt{s_{\text{parton}}} = \sqrt{x_1 x_2 s} \quad (2.59)$$

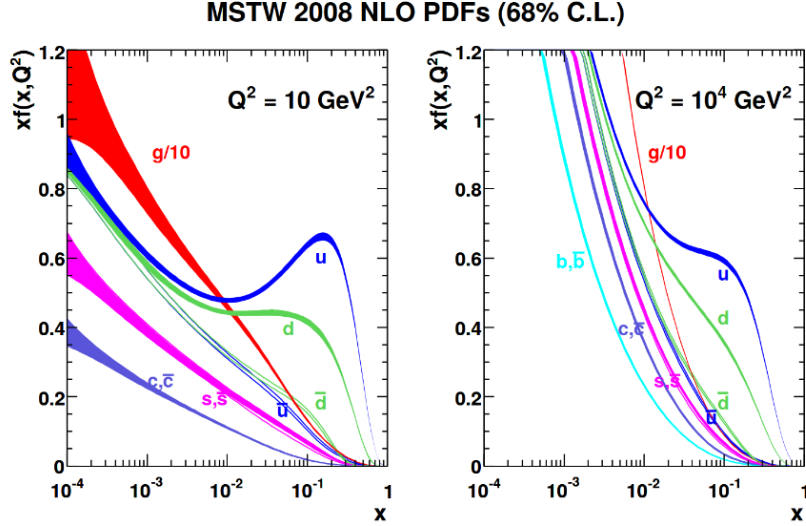


**Figure 2.5** Proton PDFs at different energy scales. Taken from [49].

where  $x_1, x_2$  denote the two four-momentum fractions of the protons and  $\sqrt{s}$  the total centre of mass energy of the protons. The probability of a certain parton carrying a certain fraction  $x$  of energy depends on the parton type and the momentum  $Q^2$  exchanged in the collision and is described by the *parton distribution functions (PDFs)*. Fig. 2.5 shows the proton PDFs at different energy scales. It can be seen that at high  $x$  values the valence quarks dominate, while for low values the sea quark and gluons dominate.

For the calculation of cross sections, the measure of how probable a reaction is in a collider experiment, the *factorisation theorem* [50] can be used. It states that the inclusive cross section for a reaction in a proton-proton-collision is given by the convolution over all  $x$  of the PDFs with the parton level cross section:

$$\sigma_{pp} = \sum_{i,j} \iint dx_1 dx_2 f_i(x_1, Q^2) f_j(x_2, Q^2) \sigma_{ij}(x_1, x_2, Q^2) \quad (2.60)$$

where the sum runs over all partons and  $\sigma_{ij}$  denotes the parton-parton cross section.

---

## 3 Analysis of the 2HDM parameter space

In this chapter the impact of the different parameters on the branching fractions and the production cross section of the 2HDM is discussed. The basis of this analysis are the 2HDM cross sections and branching ratios taken from Ref.[51]. With those numbers all relevant branching fractions and the production cross section are examined with respect to the 2HDM parameters in the physical mass basis. For the process  $A \rightarrow ZH \rightarrow \ell^+ \ell^- t\bar{t}$  these parameters are the two masses of involved Higgs bosons  $m_A$  and  $m_H$  and the ratio between the two vacuum expectation values  $\tan(\beta)$ . All other 2HDM parameters are fixed: Since the charged Higgs boson is not involved in the process, its mass does not contribute to the branching fractions at leading order. For this reason it is set to  $\max(m_H, m_A)$ . To match the  $h$  to the Standard Model Higgs boson, the alignment limit is chosen, i.e.  $\sin(\alpha - \beta) = 1$  and  $m_h = 125 \text{ GeV}$ . The parameter  $v = \sqrt{v_1^2 + v_2^2}$  is set to match its Standard Model counterpart at  $v = 246 \text{ GeV}$ . The parameter  $m_{12}$  is fixed to  $m_A^2 \tan(\beta)/(1 + \tan(\beta)^2)$ , which gives a valid model, according to Ref.[51]. With the help of equation 2.57e this can be transformed into a condition for  $\lambda_5$  of the physical mass basis.

### 3.1 Branching ratios

In this section, the two decays  $A \rightarrow ZH$  and  $H \rightarrow t\bar{t}$  and the competing processes are discussed.

#### 3.1.1 General remarks on the branching ratios of the involved processes

To obtain a general understanding of the nature of the different Higgs bosons and the parameter space, the various decay channels can be examined. A quantification of the probability of a given decay channel is described by the branching ratio. The branching ratio of an initial state  $X$  decaying into the final state  $Y$  is given by

$$Br(X \rightarrow Y) = \frac{\Gamma(X \rightarrow Y)}{\Gamma(X)} \quad (3.1)$$

where  $\Gamma(X \rightarrow Y)$  is the particle decay width of the process in question and  $\Gamma(X)$  is the total decay width consisting of the sum of all partial decay widths. Those decay widths can be calculated with Fermi's Golden Rule (see Ref. [52]) as the product of the squared matrix element times the size of the phase space element. The squared matrix elements can be calculated using the Feynman rules (see Ref. [53]) for the corresponding decay diagrams.

The final results of those calculations for all cases involved in this thesis can be found in Ref. [54]. For additional decay widths especially in the QCD sector see Ref. [55].

For decays involving top quarks, the decay width above the kinematic threshold reads [54]:

$$\Gamma(A \rightarrow t\bar{t}) = \frac{3G_F m_t^2}{4\sqrt{2}\pi} \cot(\beta)^2 m_A \sqrt{\left(1 - 4\frac{m_t^2}{m_A^2}\right)^3} \quad (3.2)$$

showing the characteristic Yukawa dependence on the mass of the decay products which causes decay into fermions with greater mass to be favoured. The decay width for the decay into any other pair of charged fermions can be obtained by replacing the  $\cot(\beta)$  with the correct coupling constant according to Table 2 and the top mass with the mass of the respective decay product.

For the decay  $A \rightarrow ZH$  the decay width is [54]:

$$\Gamma(A \rightarrow ZH) = \frac{G_F}{4\sqrt{2}\pi} \sin(\alpha - \beta)^2 \frac{m_Z^4}{m_A} \sqrt{\lambda(m_H^2, m_Z^2, m_A^2)} \lambda(m_H^2, m_A^2, m_Z^2) \quad (3.3)$$

with the  $\lambda$ -function:

$$\lambda(x, y, z) = \left(1 - \frac{x}{z} - \frac{y}{z}\right)^2 - 4\frac{xy}{z^2}. \quad (3.4)$$

Note that the two  $\lambda$  terms result in a complex dependence on the different masses. However, by calculating the Taylor series for  $m_A \gg m_Z, m_H$  the behaviour for high masses can be calculated. The second  $\lambda$  factor tends to 1, while the first factor tends to infinity by the order of  $\mathcal{O}(m_A^4)$ . Together with the  $1/m_A$  from the prefactor this leads to a dependence on  $m_A^3$  for large masses, meaning that this decay width grows faster than the Yukawa one.

#### 3.1.2 $A \rightarrow ZH$

There are many different decay channels for the heavy Higgs boson  $A$ . It can decay hadronically into a pair of quarks, leptonically into a pair of muons or taus, into a pair of photons or into a  $Z$  boson plus another Higgs ( $h$  or  $H$ ).

One of the most important parameters is the mass of the  $A$  boson. Plots of the branching ratios of the different decay channels with respect to  $m_A$  are shown in figure 3.1. For this figure the ratio of the vacuum expectation values  $\tan(\beta)$  is set to 1 and  $m_H$  to 200 GeV. The plot shows that for the low mass region  $m_A < 300$  GeV the decay into  $Zh$  and  $b\bar{b}$  dominates, since neither the decay channel into top quarks nor the one into  $ZH$  has opened up yet. At  $m_A = m_Z + m_H \approx 290$  GeV the  $A$  is heavy enough for decaying into  $HZ$ , the decay channel of this analysis. It immediately dominates over the other decay channels, becoming the leading channel with a branching ratio of almost 1, causing a decline of the other branching ratios by two to three orders of magnitude. At  $m_A = 2m_t \approx 350$  GeV the on-shell decay into a pair of top quarks is possible resulting in the branching ratio for the respective channel to peak. The branching ratio for the  $ZH$  channel decreases to around 0.2 as a result. At even higher masses the  $ZH$  branching ratio rises again due to its cubic dependence on  $m_A$  as described in equation 3.3.

The two branching ratios intersect at around  $m_A = 550$  GeV resulting in  $ZH$  to become the

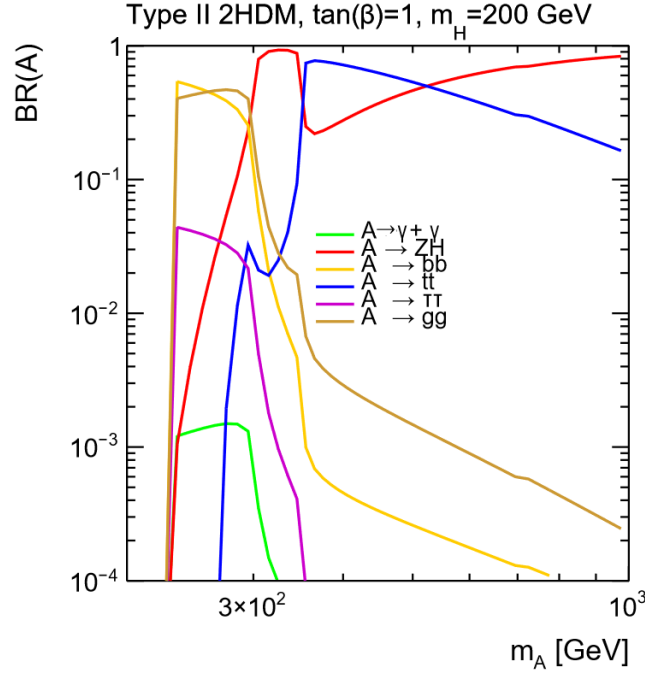


**Figure 3.1** Branching fractions for several decays of the heavy Higgs boson  $A$  as a function of its mass  $m_A$ .

leading channel again. At higher masses  $m_A > 800$  GeV the branching ratio for  $ZH$  tends to 1 while all the other steadily decline.

When studying the dependence of the branching ratio against  $\tan(\beta)$ , results are shown Fig. 3.2 (left), the influence of the coupling strength can be observed. For this plot the masses are fixed to  $m_A = 400$  GeV and  $m_H = 200$  GeV. According to the couplings in a type II 2HDM described in the first chapter,  $\tan(\beta)$  modifies the coupling strengths to up-type quarks on one hand and down-type quarks and charged leptons on the other. Higher values of  $\tan(\beta)$  result in a higher coupling to bottom quarks and taus while the coupling to top quarks is suppressed. Interestingly, the channel  $ZH$  peaks at medium values of  $\tan(\beta)$ . This is explained by the growing advantage either the  $b\bar{b}$  or the  $t\bar{t}$  acquires at extreme values of  $\tan(\beta)$ , while the branching ratio of the  $ZH$  decay does not depend on  $\tan(\beta)$ .

As shown in Fig. 3.2 (right), the influence of  $m_H$  is rather small. Looking at mass regions where the top decay of the  $A$  is accessible, the only two significant decay channels are  $t\bar{t}$  and  $ZH$ . The closer  $m_H$  gets to the threshold of  $m_H + m_Z = m_A$ , the more the branching ratio of the  $ZH$  channel decreases. Although equation 3.3 breaks down in the near vicinity of threshold  $m_H = m_A - m_Z$ , it predicts a steady decrease when approaching this limit, which is in good agreement with Fig. 3.2 (right).

By only looking at the decay channel of this analysis it is possible to visualize its branching ratio with respect to two parameters. Choosing both masses  $m_H$  and  $m_A$  gives a good overview of some important features. Such an overview can be found in Fig. 3.3 (left).

### 3 Analysis of the 2HDM parameter space

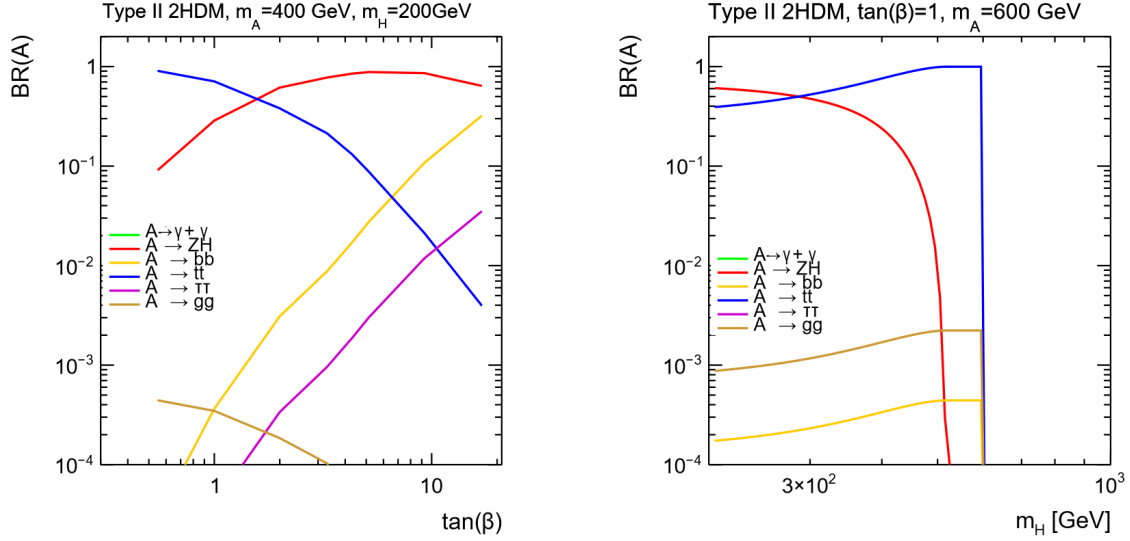


**Figure 3.2** Branching fractions for several decays of the heavy Higgs boson  $A$  as a function of the ratio of the vacuum expectation values  $\tan(\beta)$  (left) and  $m_H$  (right), the mass of the  $H$ .

The diagonal line represents the chosen mass hierarchy with the  $A$  heavier than the  $H$ , so only the lower right half of the plot is filled. Furthermore, for the on-shell production of  $Z$  and  $H$  the mass condition  $m_A > m_H + m_Z$  has to apply rendering the branching ratio to nearly zero in the 90 GeV broad band connected to the diagonal edge. Also visible is the small area between 250 GeV and 350 GeV where the  $ZH$  channel is dominating without its competing process  $t\bar{t}$  resulting in a small yellow triangle in the bottom left part of the plot. Overall, the tendency that a large mass difference between  $A$  and  $H$  leads to a larger branching fraction of the  $ZH$  channel is apparent.

Looking at the  $m_A$ - $\tan(\beta)$ -plane in Fig. 3.3 (right), many of the above mentioned effects are visible: A distinct ridge between 300 GeV and 350 GeV again marks the region where the  $ZH$  channel is energetically available, but the  $t\bar{t}$  channel is not. For higher masses the branching ratio rises again. Noticeable is also the ridge of maxima with respect to  $\tan(\beta)$  at around 5-10. As mentioned before, very extreme values favour the decay into one of the quark families. Since the top decay is favoured due to the higher mass of the top compared to the bottom, the maximum is shifted to higher  $\tan(\beta)$  values.

#### 3.1.3 $H \rightarrow t\bar{t}$

For the heavy Higgs boson  $H$  there are generally fewer decay channels, most importantly there is no leading order decay into another heavy Higgs boson possible as previously the  $ZH$  channel. Dominating channels are again the decay into top or bottom quarks, the decay into gluons and the leptonic decay.

Looking at the branching ratios with respect to  $m_H$  as shown in Fig. 3.4, it is evident that for the medium and high mass regions from around  $m_H = 400$  GeV the  $t\bar{t}$  channel reaches branching

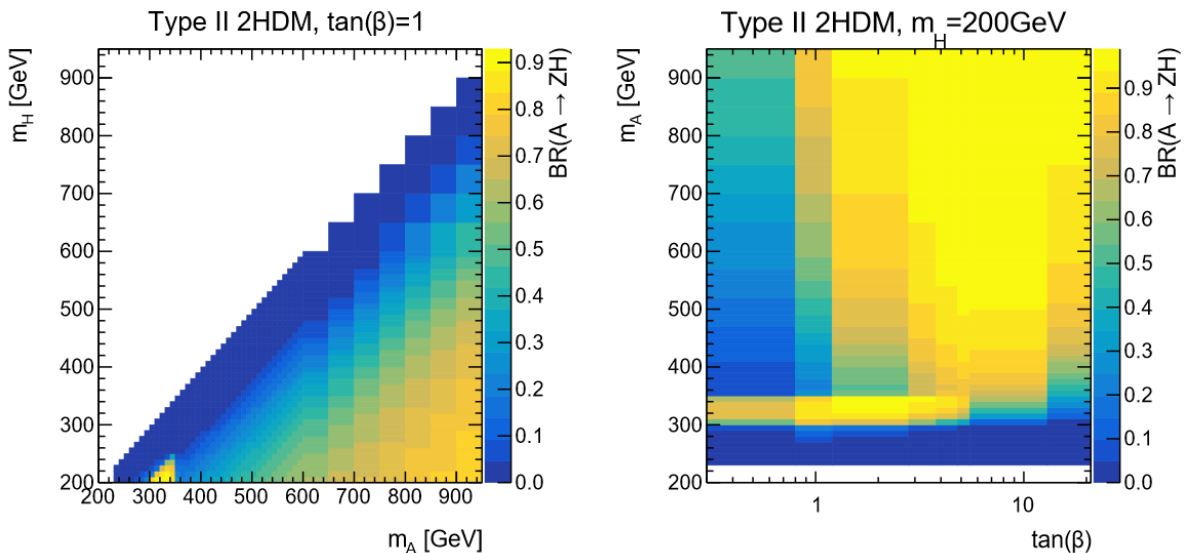


**Figure 3.3** Branching ratio of the decay process  $A \rightarrow ZH$

fractions of nearly 1. Below the  $2m_t$  threshold the  $b\bar{b}$  channel leads for most of the lower mass area, only briefly being surpassed by the gluon gluon channel at 310 GeV to 340 GeV.

The branching fractions with respect to  $\tan(\beta)$  in Fig. 3.5 (left) show a similar behaviour as in Fig. 3.2. Again the higher values favour the bottom decay compared to the pure Yukawa coupling in the Standard Model, while low values favour the top decay. This time the sum of both branching fractions is close to 1 since there is no important competing process like  $A \rightarrow ZH$ .

For the sake of completeness, Fig. 3.5 (right) shows the dependence on  $m_A$ . As expected it has no influence on the different branching ratios which are constant over the whole mass range.

The two dimensional plot (Fig. 3.6) gives a compact overview over some of the features mentioned above. The threshold at 350 GeV marks the opening of the  $t\bar{t}$  channel. Since there is no competing channel as before, this time the branching ratio grows monotonously with  $m_H$ .

A very prominent feature is the strong dependence of the branching ratio on  $\tan(\beta)$ . Since the  $b\bar{b}$  channel shows inverse scaling with respect to  $\tan(\beta)$ , the transition zone between the top quark and the bottom quark decay channel is rather narrow.

## 3.2 Production cross sections

After studying the parameter space for the different branching ratios a similar study for the production cross section is performed. The production cross section  $\sigma$  gives a quantitative measure on how likely a certain particle will be produced in a collider experiment. More on this in section 4.1.

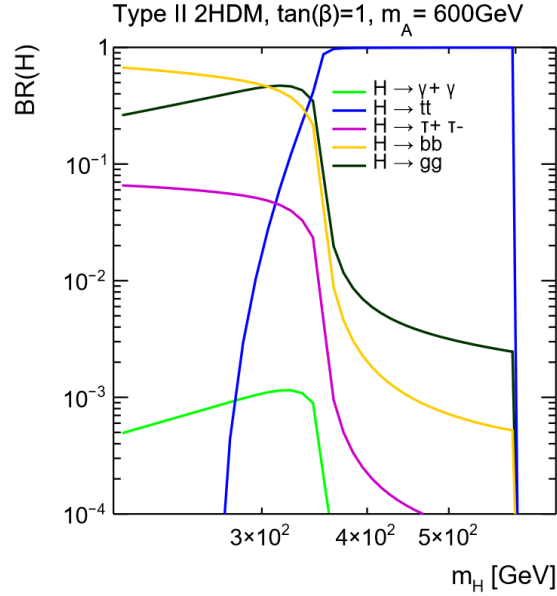


**Figure 3.4** Branching fractions for various decay channels of the heavy Higgs  $H$  with respect to its mass  $m_H$

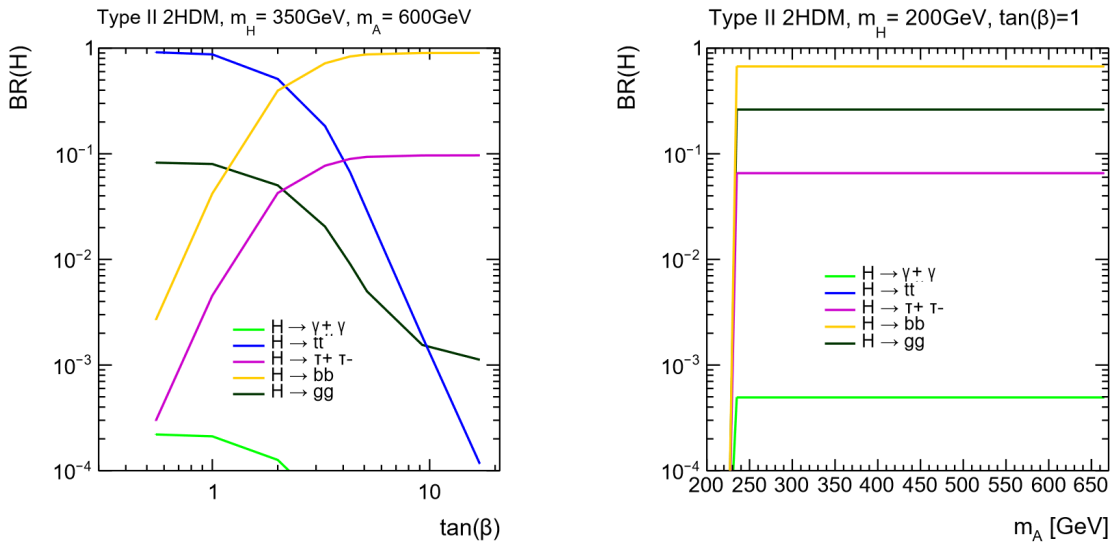


**Figure 3.5** Branching ratios of the heavy Higgs boson  $H$  with respect to  $\tan(\beta)$  (left) and the mass of the heavy Higgs  $A$   $m_A$  (right).

#### 3.2.1 The Standard Model Higgs boson production cross section

Because most of the production cross sections for 2HDM Higgs bosons are given in terms of the Standard Model cross section, a brief review of the latter is given. The following section mostly follows Ref. [56]. In the Standard Model there are four leading order production modes:

- Gluon-gluon fusion (ggF). At the LHC this process is the main production mode for the Higgs boson. Two gluons merge and form a loop of virtual quarks. At the end of the loop a real Higgs boson emerges. Since the Higgs fermion coupling is proportional to a



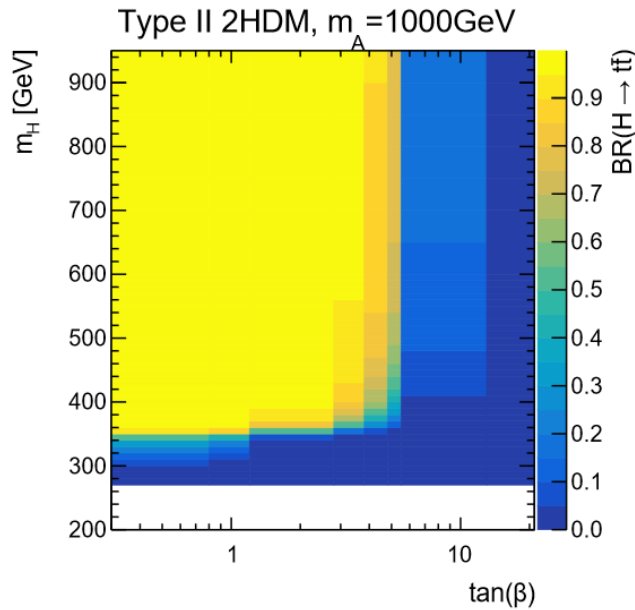


**Figure 3.6** Branching ratio for the process  $H \rightarrow t\bar{t}$

particles mass, this process happens most often with top- or bottom quarks in the loop. Such a process is shown in Fig. 3.7a.

- Vector boson fusion (VBF). A quark-antiquark pair exchanges a vector boson ( $W$ ,  $Z$ ) which then emits a Higgs boson. For the LHC this is the second most important production channel. The corresponding Feynman diagram can be found in Fig. 3.7b.
- Higgs-strahlung. A quark-antiquark pair merges and creates a  $W$  or  $Z$  boson with sufficient energy that it can radiate a Higgs boson. For proton-antiproton colliders such as the Tevatron this process is the second most important one while for the LHC it is only the third largest contributor. It is shown in Fig. 3.7c.
- $t\bar{t}$  associated Higgs production ( $t\bar{t}h$ ). A Higgs boson is produced with a pair of top quarks in the final state. One possible mode is the following: Two gluons decay into a pair of heavy quarks each (most likely tops). Then one quark-antiquark pair merges to form a Higgs boson. This is shown in Fig. 3.7d.

It is possible to calculate the production cross section of the Standard Model Higgs boson as a function of its mass  $m_h$ , see Ref. [57]. An overview of the cross sections for the different production modes at different values of  $m_h$  is shown in figure 3.8.

It becomes evident that ggF is the main production mode at the LHC not only for the actual Standard Model Higgs boson mass of 125 GeV. Between 100 GeV and 500 GeV the ggF is around one order of magnitude larger than VBF, which is the second most important production mode. Only when approaching 1000 GeV both channels start to converge.

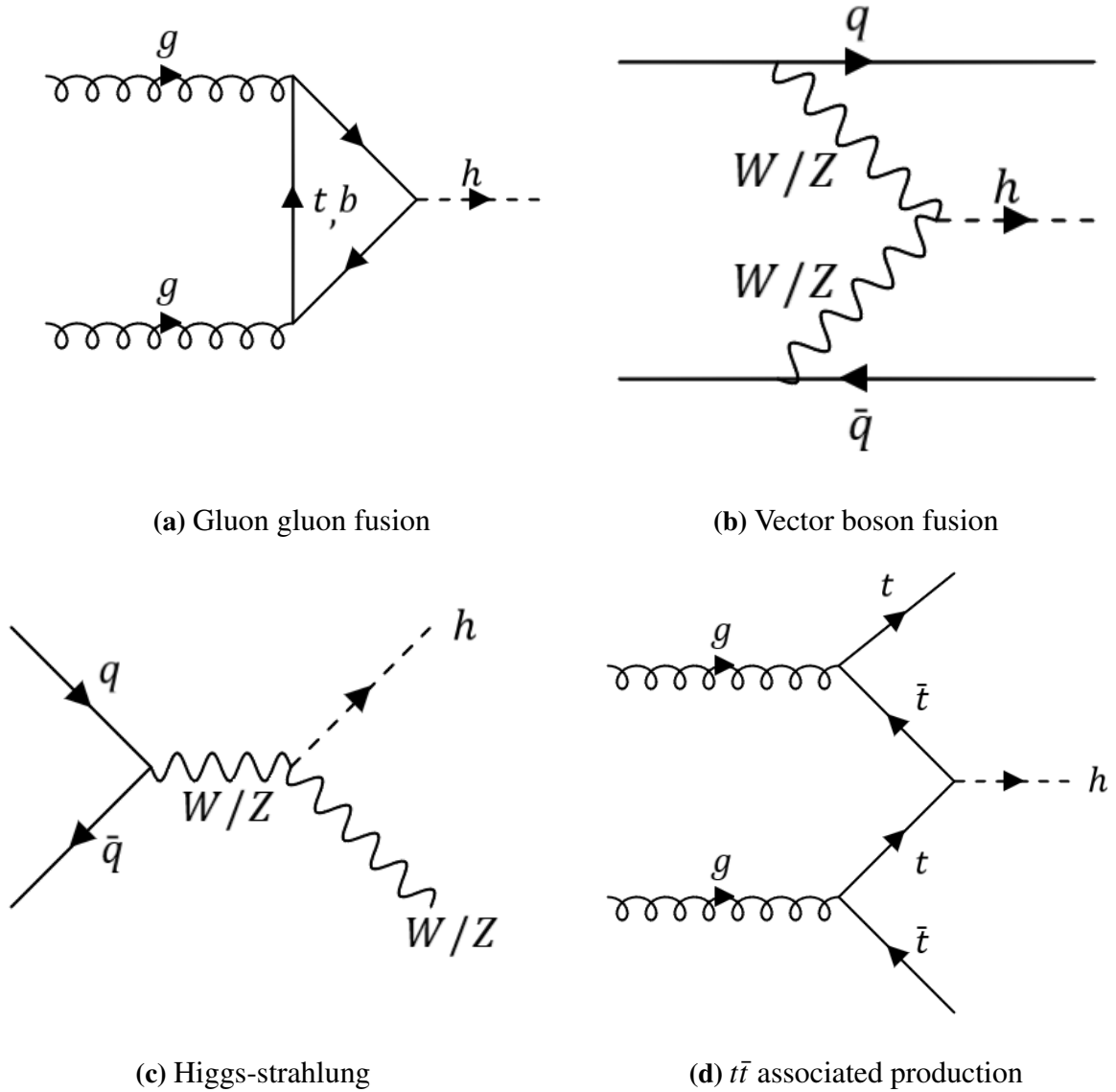


**Figure 3.7** Feynman diagrams for the four most common Higgs production modes at leading order

### 3.2.2 The 2HDM production cross section

For the production of the heavy Higgs bosons  $A$  and  $H$  there are a few notable differences compared to the Standard Model. First of all, the coupling between  $A$  and two vector bosons (AVV) is zero, see Table 2. The same is true for the HVV vertex in the alignment limit. This rules out two important production modes: The VBF and the Higgs-strahlung, leaving only the ggF and the  $t\bar{t}A$ .

To calculate the 2HDM production cross sections from the SM cross section, correction factors are applied to the SM results take into account the different coupling constants.

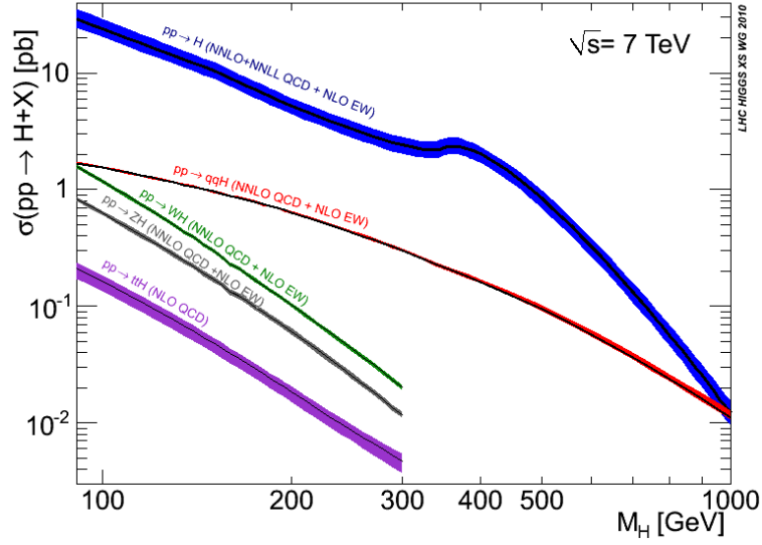


**Figure 3.8** Production cross section for different production modes with respect to  $m_h$ . Taken from Ref. [57].

For the ggF the prefactor is [56]:

$$\frac{\sigma_{gg \rightarrow A}}{\sigma_{gg \rightarrow h(\text{SM})}} = \frac{9}{4} \cot^2(\beta) \cdot \left| 1 - (3.5 - 4i) \frac{\tan^2(\beta)}{m_A} \right|^2 \quad (3.5)$$

The  $gg \rightarrow A$  production cross section with respect to  $\tan(\beta)$  is shown in Fig. 3.9 for three different masses  $m_A$ .

The structure involving a minimum in the middle and growing production rates for lower and higher values of  $\tan(\beta)$  are explained by the coupling of the  $A$  to the quarks in the loop of the ggF. In the lower region the loop is dominated by top quarks, so a further lowering of  $\tan(\beta)$  will increase the respective coupling strength since it scales with  $\cot(\beta)$ . At high values the opposite is true since bottom quarks dominate the loop whose coupling scales with  $\tan(\beta)$ .

The position of the minimum changes to higher values of  $\tan(\beta)$  for higher masses. The reason for this is that for higher masses the production via top quarks becomes increasingly likely, resulting in the equilibrium between top quarks and bottom quarks being reached at higher values of  $\tan(\beta)$ .

Generally a decrease of the production cross section with increasing mass can be observed. This is mostly caused by the decreasing Standard Model cross section as seen in Fig. 3.8.

The only other leading order production cross section, the  $t\bar{t}$ -associated production, can be calculated by the following formula:

$$\sigma_{gg \rightarrow t\bar{t}A} = \sigma_{gg \rightarrow t\bar{t}h(\text{SM})} \cdot \cot^2(\beta) \quad (3.6)$$

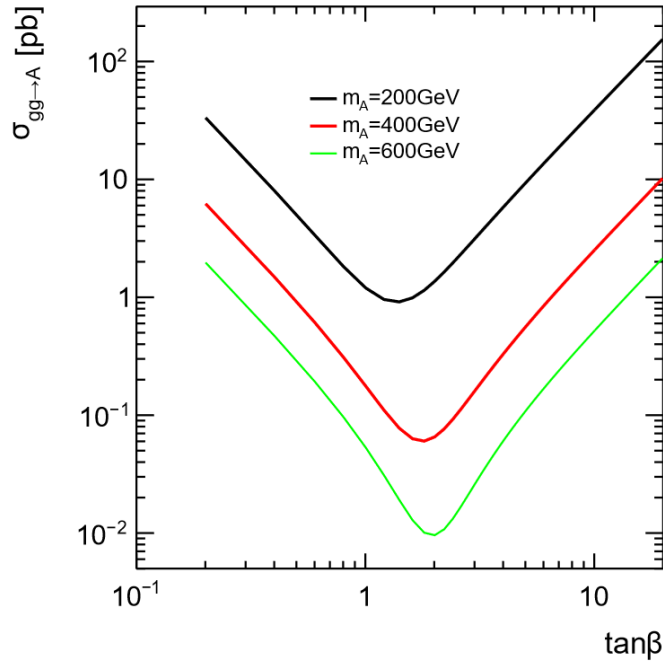


**Figure 3.9** Production cross section for the heavy Higgs  $A$  with respect to  $\tan(\beta)$  produced via ggF for three different masses  $m_A$

Again due to the  $At$ -coupling the cross section is enhanced for low values of  $\tan(\beta)$ , but since the same effect is true for ggF, the cross section for the  $t\bar{t}A$  production remains suppressed by its Standard Model counter part which is approximately two orders of magnitude smaller for  $t\bar{t}A$  than for ggF.

The same is true for the  $b\bar{b}A$ . Relative to the top cross section it is suppressed by a factor of  $[m_b \setminus m_t]^2$  and scales with  $\tan(\beta)$  rather than  $\cot(\beta)$ . Still, the same argumentation as before applies, this time for high values of  $\tan(\beta)$ . For this reason the total production cross section equals roughly the ggF production cross section for the entire parameter space of this analysis. Therefore, for the rest of this analysis only the ggF cross section is considered which for the sake of convenience will simply be called production cross section in the following.

This however is not necessarily an appropriate assumption for other types of 2HDMs. For certain regions of the parameter space in a type I 2HDM, the  $b\bar{b}$  associated production channel can be the dominating production mode. Such scenarios are discussed in depth in Ref. [58].

### 3.3 Product of branching ratios and production cross section

For a comprehensive overview the product of the three parameters relevant for this analysis, namely  $\sigma_{gg \rightarrow A}$ ,  $BR(A \rightarrow ZH)$  and  $BR(H \rightarrow t\bar{t})$  has to be discussed. This production cross section for the final state  $Zt\bar{t}$  with respect to  $m_A$  and  $m_H$  is shown in Fig. 3.10 as a two dimensional plot.

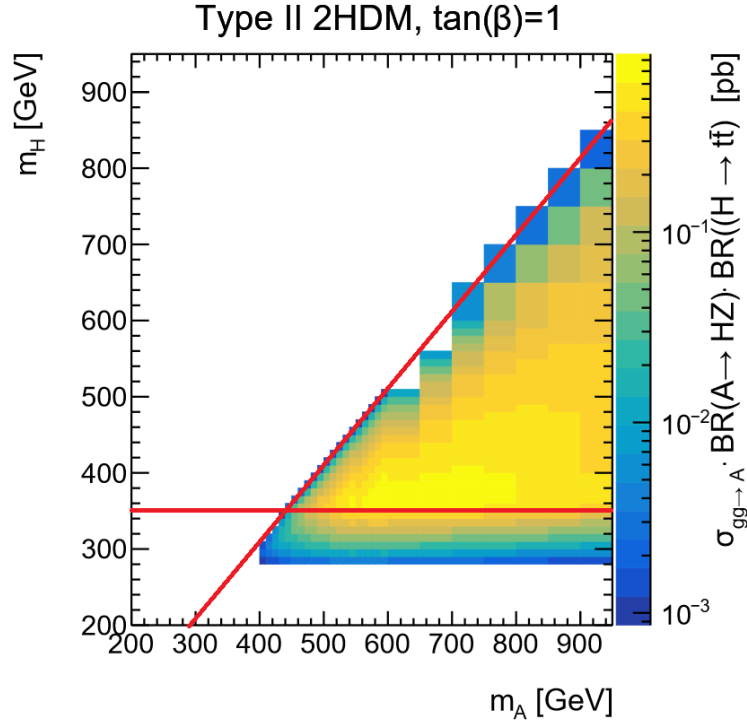


**Figure 3.10** Product of the production cross section and the two branching ratios with respect to masses of the two heavy Higgs bosons  $A$  and  $H$   $m_A$  and  $m_H$ . The red lines represent the thresholds  $m_A = m_H + m_Z$  and  $m_H = 2m_t$ .

Since it is the product of the two branching ratios, both thresholds ( $m_A > m_H + m_Z$  and  $m_H > 2m_t$ ) are shown in the plot as red lines. Since the colour scaling is logarithmic, the small chance for an off-shell production of the respective particle below the threshold is visible. Compared to Fig. 3.3 a few noticeable differences are visible. First of all, Fig. 3.3 does of course not show the lower threshold on  $m_H$ . Furthermore, the monotonous increase of the branching ratio with respect to  $m_A$  changes into a structure with a ridge of maxima at around  $m_A = 700$  GeV. The reason for this decrease at higher value is the branching ratio which begins to saturate at nearly one, while the production cross section, as shown in Fig. 3.8, starts to decrease rapidly at higher mass values.

The decay channel of this analysis is dominant in large region of the parameter space. Both separate decays are the leading channels, especially in the higher regions of  $m_H$  and in regions with a big mass difference. Compared to the decay into bottom quarks or leptons, the  $H \rightarrow t\bar{t}$  channel makes higher mass regions accessible. A search in this channel is promising to explore further regions of the parameter space. Especially in the lower right centre of figure 3.10 the total cross section from production to final state reaches values of up to 1 pb, promising a comparatively large number of signal events.

## 4 Experimental setup

This thesis uses simulated data based on Run-2 from the Compact Muon Solenoid Detector (CMS) at the Large Hadron collider (LHC) at CERN. In section 4.1 the general properties of the LHC are introduced, followed by a description of the CMS detector in section 4.2.

### 4.1 The Large Hadron Collider

The LHC is a particle ring accelerator in which protons are accelerated and collided at the location of different detectors, such as the CMS detector. Section 4.1.1 will explain the most important properties of particle accelerators, section 4.1.2 will then give an overview over the specific properties of the LHC.

#### 4.1.1 General features of particle colliders

The most important features of a particle collider are the centre-of mass energy and the luminosity.

In a particle collider like the LHC, where particles with the same mass are collided, the centre of mass energy is:

$$\sqrt{s} = 2E_p \quad (4.1)$$

with  $E_p$  the kinetic energy of the proton. The centre of mass energy is also the maximum value for the mass of new particles. Its scaling  $\sim E_p$  is characteristic for collider experiments and one of the advantages compared to fixed target experiments, where the centre of mass energy scale  $\sim \sqrt{E}$ .

The second property is the (instantaneous) luminosity. It describes the incoming flux in a collider per area and time:

$$L = \frac{N_1 N_2 f N_B}{A} \quad (4.2)$$

where  $N_B$  is the number of bunches (packets of particles) with the area  $A$  and the number of particles  $N_1$  and  $N_2$  in them, colliding with a frequency of  $f$ . The instantaneous luminosity can be integrated over time, to measure the total amount of collision taking place:

$$L_{int} = \int L dt \quad (4.3)$$

The total number of reaction taking place in a certain time is simply the integrated luminosity over this time period times the cross section of the reaction.

For the cross section and integrated luminosity, the unit *barn*  $1 \text{ b} = 10^{-28} \text{ m}^{-2}$  is used.

The accurate measurement of the luminosity is crucial, since any uncertainty luminosity will directly transfer into an uncertainty on the number of expected events and therefore the cross

section measurement. At the LHC the luminosity is measured and calibrated using several methods, e.g the *van der Meer scan*. This technique uses overlapping scans to calculate the extension of the bunches. Since all other variables are fixed by the design of the collider, the luminosity can be calculated. A detailed description of this method can be found in Ref. [59]. The integrated luminosity of the LHC measured by the CMS detector can be seen in Fig. 4.1. From the gradient of the different years it can be seen, that the instantaneous luminosity has

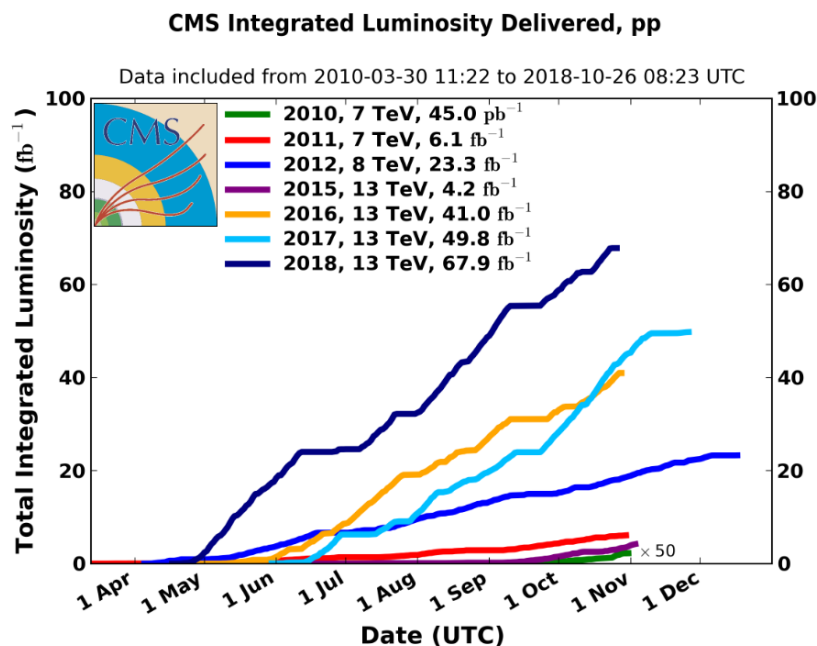


**Figure 4.1** The integrated luminosity of the LHC for different years. Taken from Ref [60].

been improved over the years by several different technical upgrades.

#### 4.1.2 Overview over the LHC components and properties

The LHC consists of two circular, evacuated beam pipes with a radius of 4.3 km. Inside these beam pipes two beams of protons are accelerated into opposite directions using superconducting cavities. The principle is described in depth in Ref. [61]. The proton beams are held on the circular track using dipole magnets and focused using quadrupole and higher order magnets. [62].

The LHC is designed to reach a centre of mass energy up to 14 TeV and a luminosity of  $10^{34} \text{ cm}^{-2} \text{ s}^{-1}$  [63]. The highest energy reached so far was 13 TeV during Run-II, in the years 2015-2018.

Because of the acceleration with cavities the beam divides into several bunches of particles, each with approximately  $1.15 \times 10^{11}$  protons. By design, the LHC can hold up to 2808 bunches. However, the highest number of bunches used so far was 2556 in 2017 [64].

The two beam pipes intersect at four places. At the four intersection point, four experiments are

## 4 Experimental setup

located. The first two: ATLAS [65] and CMS [66] are located at opposite ends of the ring and are multi-purpose detectors, to observe any new physics phenomenons at the LHC. The other two experiments are LHCb [67], specialized on the physics of B mesons and ALICE [68], an experiment specialised on heavy iron collisions.

The LHC does not accelerate the particles from rest. A series of pre-accelerators is used. The numbers in the following section are taken from Ref. [69]. The protons, produced from hydrogen gas which is ionized, run through the linear accelerator LINAC2 (which will be replaced by LINAC4 for Run-III), which accelerates the protons to 50 MeV. Then a set of circular accelerators is used: First the *Proton Synchrotron Booster* (PSB) further accelerating the protons to 1.4 GeV, followed by the *Proton synchrotron* (PS) which accelerates the protons to 26 GeV and finally the *Super Proton Synchrotron* (SPS) where the protons are accelerated to their injection energy of 450 GeV. The SPS already has a radius of more then a kilometre and is located around the ATLAS experiment. An overview of the different pre accelerators can be found in Fig. 4.2.

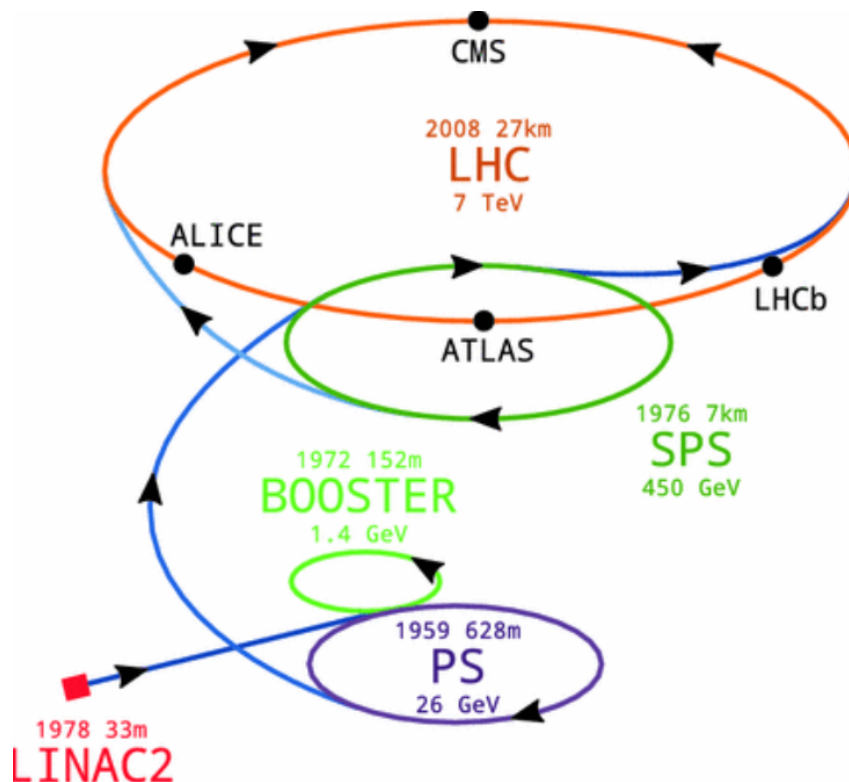


**Figure 4.2** The LHC with its pre-accelerator and experiments. Taken from Ref [70].

The whole acceleration process takes approximately 25 minutes with the pre-acceleration only taking milliseconds to seconds [71]. After about ten hours of collisions, the beam is exhausted and being dumped from the LHC.



## 4.2 The Compact Muon Solenoid Experiment

The CMS is one of the two multi purpose detectors at the LHC. Based on Ref. [66] the following sections will give an overview over the coordinate system used at the CMS detector and then describe its different components and sub-detectors.

### 4.3 The coordinate system

To describe the properties of the measured interaction products in the CMS detector, a spatial coordinate system is used based on spherical coordinates. As definition, the z-axis points in the direction of the beam, while the x-y-plane stand perpendicular to the beam. [72] The azimuthal angle  $\phi$  describes the angle relative to the x-axis in the x-y-plane. Since the colliding partons in general carry different fractions of the protons momentum, the decay products receive a Lorentz boost along the z-axis. This boost alters the polar angle  $\theta$  relative to the z-axis. The angle  $\theta$  has an important disadvantage: An angular difference  $\Delta\theta$  is not Lorentz invariant under this boost, which is why it is replaced by the *rapidity*  $y$ , defined as:

$$y = \ln \left[ \frac{E + p_z}{E - p_z} \right] \quad (4.4)$$

with  $p_z$  the z-component of the momentum. A difference between rapidities is Lorentz invariant. Furthermore, the *pseudorapidity* is defined as:

$$\eta = -\ln \left[ \tan \left( \frac{\theta}{2} \right) \right] \quad (4.5)$$

for which the difference between two pseudorapidities is again a Lorentz invariant quantity. For  $m \ll p$ , the two quantities are approximately equal  $y \approx \eta$ . Fig. 4.3 shows the pseudorapidity with respect to  $\theta$ . Close to the x-y-plane the pseudorapidity approaches zero, closer to the beam axis, the pseudorapidity tends to  $\pm\infty$ .

The angular distance  $\Delta R$  is defined as:

$$\Delta R = \sqrt{\Delta\eta^2 + \Delta\phi^2} \quad (4.6)$$

The total momentum of a particle is replaced by the transverse momentum of a particle, because the momentum in z-direction would be difficult to measure, since one would need to measure precisely all particles and their momentum z-components, which is becoming more difficult at high pseudorapidities close to the beam pipe, where there are no detector elements. The transverse momentum  $p_T$  is defined as:

$$p_T = \sqrt{p_x^2 + p_y^2} \quad (4.7)$$

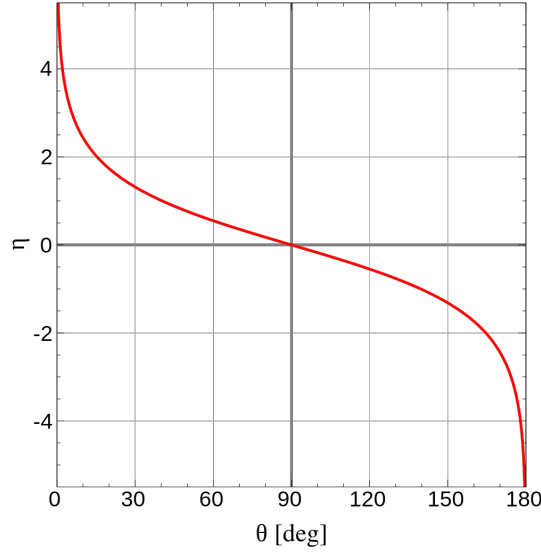


**Figure 4.3** The pseudorapidity with respect to the polar angle  $\theta$ . Taken from Ref. [73].

making it also invariant under a boost in z-direction. The momentum in cartesian coordinates can be retrieved from  $p_T$ ,  $\eta$  and  $\phi$  by the following relations:

$$\begin{aligned} p_x &= p_T \cos(\phi) \\ p_y &= p_T \sin(\phi) \\ p_z &= p_T \sinh(\eta) \end{aligned} \tag{4.8}$$

### 4.4 CMS sub detectors

The CMS detector consists of several sub detectors, each specialised to measure certain properties and certain kinds of particles. The next sections will give an overview over the main sub components of the CMS detector. A cutaway drawing of the detector for an overview can be found in Fig. 4.4. The beam pipe itself running through the centre of the detector has a diameter of 4.5 cm. Starting from the beam pipe and going further and further out, the following detectors are located inside the CMS.

#### The Tracking System

The purpose of the innermost layer, the *tracking system*, is the precise measurement of the trajectories of the charged particles. The tracker as a whole has a length of  $\sim 5.8$  m and a diameter of  $\sim 2.5$  m, meaning that the covered  $\eta$  region of the tracker includes approximately the interval  $[-2.5, 2.5]$ .

An overview over the different components of the tracking system after the upgrade of 2017 can be found in Fig. 4.5.

The tracking system consist of silicon detectors, that are sensitive to charged particles passing

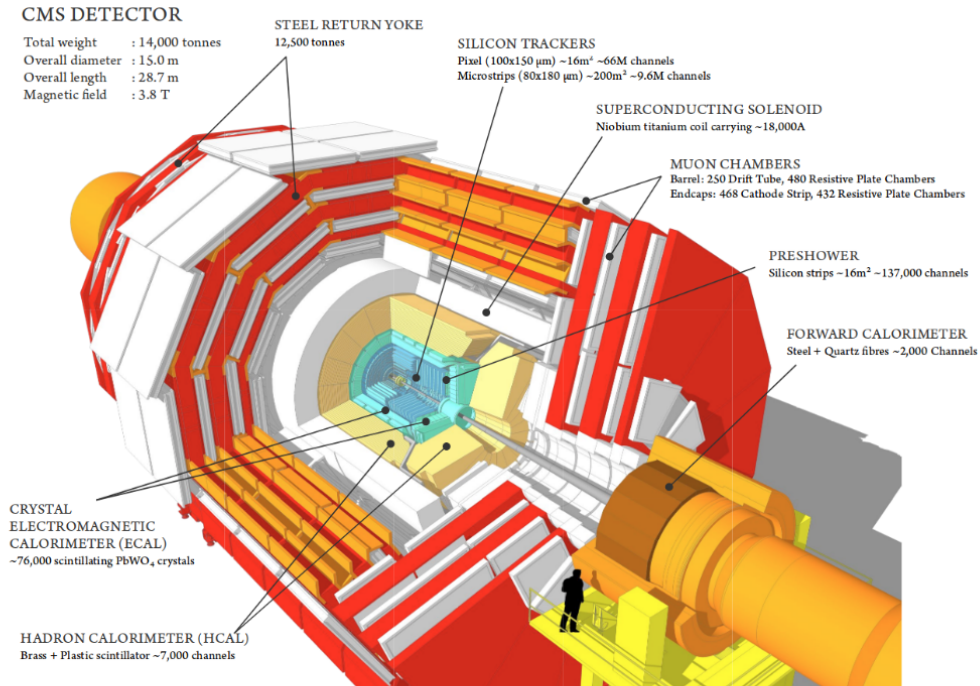


**Figure 4.3.** Cutaway view of the CMS detector. Taken from Ref. [55].

**Figure 4.4** A technical cutaway drawing of the CMS detector with its sub components. Taken from Ref. [74].

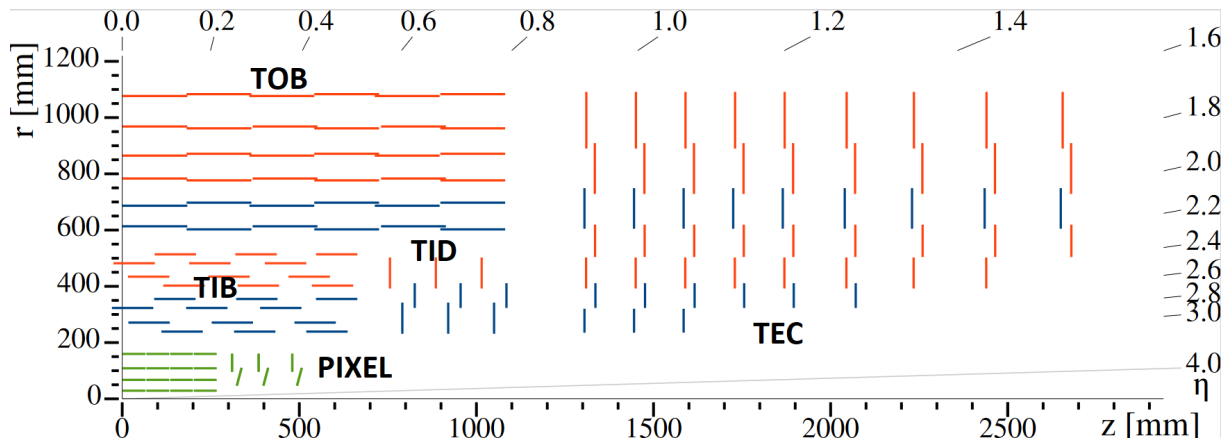


**Figure 4.5** The different components of the tracking system of CMS. Taken from Ref. [75].

though them. The energy loss in the tracker is generally low compared to other detector types such as the calorimeters.

The inner part of the tracking system consists of the PIXEL detector. Since 2017 it comprises four layers of pixel detectors at the barrel region, and three layers at the endcap region close to the beam pipe. The closest layer is placed at a distance of only 3 cm to the collision centre, the furthest is placed 16 cm from the centre. The close positioning of the pixel detectors is crucial for the identification of jets originating from b quarks. In total 66 million individual

pixel sensors measure the tracks in the pixel detector.

Further away from the centre at a radius of 20 to 55 cm the tracker inner barrel (TIB) and at a radius of 55 to 120 cm the tracker outer barrel (TOB) are located. Both consist of strip detectors, the TIB of four, the TOB of six.

At the same radius but at a higher distance in z-direction lays the tracker inner disk (TID) and even further in z-direction expanding along the full radius of the tracking system the tracker endcap (TEC) is located.

### The Electromagnetic Calorimeter

Surrounding the tracking system is the electromagnetic calorimeter (ECAL). Its main purpose is the measurement of the energy of electromagnetically showering particles as for example electrons or photons.

The electromagnetic calorimeter is made of  $\sim 75800$  lead tungsten ( $\text{PbWO}_4$ ) crystals. In the ECAL the particles induce a electromagnetic shower, by a cascade of subsequent pair production and bremsstrahlung processes. Each process increases the number of particles while decreasing their average energy until the energy is too low for the production of pairs or bremsstrahlung. The particles then deposit their energy in the crystals by producing scintillation light. The intensity of this scintillation light is proportional to the energy of the incoming particle.

The lead tungsten crystals show advantageous properties for building an ECAL with them. Their density is high  $\rho = 8.28 \text{ gcm}^{-3}$  resulting in a short radiation length of  $X_0 = 0.89 \text{ cm}$ , a property used to quantify the energy loss of electromagnetically interacting particles when travelling through matter. Furthermore their Mollière radius  $R_m$  describing the transversal extent of an electromagnetic shower is only 2.2 cm, allowing a compact calorimeter with high granularity.

Similar to the Tracker, the ECAL consists of a barrel region at  $|\eta| < 1.5$  and an endcap region at  $1.5 < |\eta| < 3.0$ . The barrel region consists of 61200 crystals with a surface area of  $22 \text{ mm} \times 22 \text{ mm}$  each, while the endcap regions consist of a total of 14648 crystals with a surface area of  $28.6 \text{ mm} \times 28.6 \text{ mm}$  each. Due to continuous improvements and the good  $r/X_0$  ratio the CMS ECAL allows a very precise energy measurement with a resolution of [76] [77]:

$$\frac{\sigma_E}{E} = \frac{2.8\%}{\sqrt{E[\text{GeV}]}} \oplus 0.3\% \oplus \frac{12\%}{E[\text{GeV}]} \quad (4.9)$$

The first term represents the stochastic effects from the showering, the second term the calibration uncertainties, independent from the measured energy, and the third term the noise from the systems electronic.

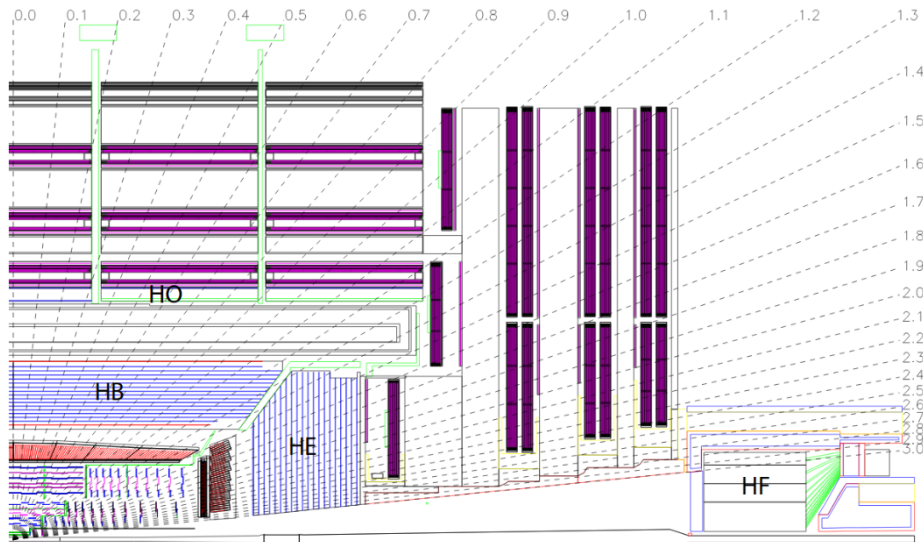


**Figure 4.6** Overview over the HCAL. Taken from Ref [66].

### The Hadronic Calorimeter

Around the ECAL the hadronic calorimeter (HCAL) is situated. It reaches from  $r = 1.77$  m to  $r = 2.95$  m. It can be further divided into the hadron barrel (HB) and the hadron outer (HO) in the barrel region and the hadron endcap (HE) and the hadron forward (HF) in the endcap region. A schematic overview can be found in Fig. 4.6.

The HB covers the regions with  $|\eta| < 1.3$  and is divided into 36 azimuthal wedges with 18 absorber plates in each wedge. The HO is structured in a similar way and extends the HB a further radii. The HE covers a the region  $1.6 < |\eta| < 3.0$  with its absorbers and detectors aligned in the x-y plane. For the highest pseudorapidities up to  $|\eta| < 5$  the HF is designed, to miss as few particles as possible. The total extension in z-direction of the HCAL is 11.2 m Its main purpose is the detection of hadronic jets. Similar to the electrons and photons in the ECAL, hadrons form a hadronic shower in the HCAL. Compared to the electromagnetic showering these showers are broader and have a longer interaction length in the same material. For this reason, the hadrons only lose a small fraction of their energy in the ECAL.

Some important differences between the ECAL and the HCAL shall be pointed out. The HCAL is a sampling calorimeter. It is build from two kinds of elements: Brass absorbers and plastic scintillators. The brass absorber have a relatively short interaction length of only approximately 16.42 cm, meaning that most of the energy of the hadrons is deposited in the brass absorbers. A certain fraction of the initiated shower is then measured in the plastic scintillators. By knowing this fraction of  $\sim 7\%$  very precisely, the total amount of energy deposited in the calorimeter can be determined. This is contrary to homogenous ECAL, in which all volume is sensitive. Furthermore, the radius of the ECAL corresponds to approximately 25 radiation lengths, while the radius of the HCAL corresponds to only around 5 interactions lengths.

Overall the energy resolution is given by:

$$\frac{\sigma_E}{E} = \frac{100\%}{\sqrt{(E[\text{GeV}]})} \oplus 5\% \quad (4.10)$$

With the statistical uncertainty much larger than for the ECAL. For this reason, the noise term  $\sim 1/E$  is negligible for most cases.

### The Solenoid Magnet

Central element of the CMS is the superconducting solenoid magnet. It is 6 m in diameter, 12 m long, made out of niobium titanium coils and weighs 220 t. A metal return yoke surrounding the whole detector returns the magnetic flux. Inside the solenoid a magnetic field of 3.8 T is produced. This magnetic field enables the determination of charge and momentum of charged particles in the inner detector components. Charged particles are subject to a Lorentz force when travelling through a magnetic field  $B$ :

$$\vec{F} = q\vec{v} \times \vec{B} \quad (4.11)$$

This forces the particles on a circular path, where for the radius  $r$  the following relation holds true:

$$\frac{mv}{r} = qB \quad (4.12)$$

When the magnetic field and the charge of the particles are known, the measured radius determines the momentum of the particles:

$$p = qrB \quad (4.13)$$

### The Muon System

Muons are minimally ionizing particles at the energies occurring in the proton-proton collisions, meaning the travel through all previously mentioned detector components without a significant energy loss. Since muons play an important role in different kind of analyses, including the one in these thesis, another sub detector, solely for muons is situated outside of the solenoid magnet. To measure the energy of the muons it relies on three different kinds of detectors: Drift tube chambers (DT), cathode strip chambers (CSC) and resistive plate chambers (RPC). A schematic overview can be found in Fig. 4.7.

The drift tubes are located in the barrel region where the magnetic field is approximately uniform and the muon flux is relatively small. The drift tubes are made from  $42 \text{ mm} \times 13 \text{ mm}$  cells, filled with a mixture of 85% Argon and 15%  $\text{CO}_2$ . Muons ionize the gas in the drift chambers and by using timing information, the muons position within the cell can be determined.

The cathode strip chambers are located at the endcap region with an varying magnetic field and

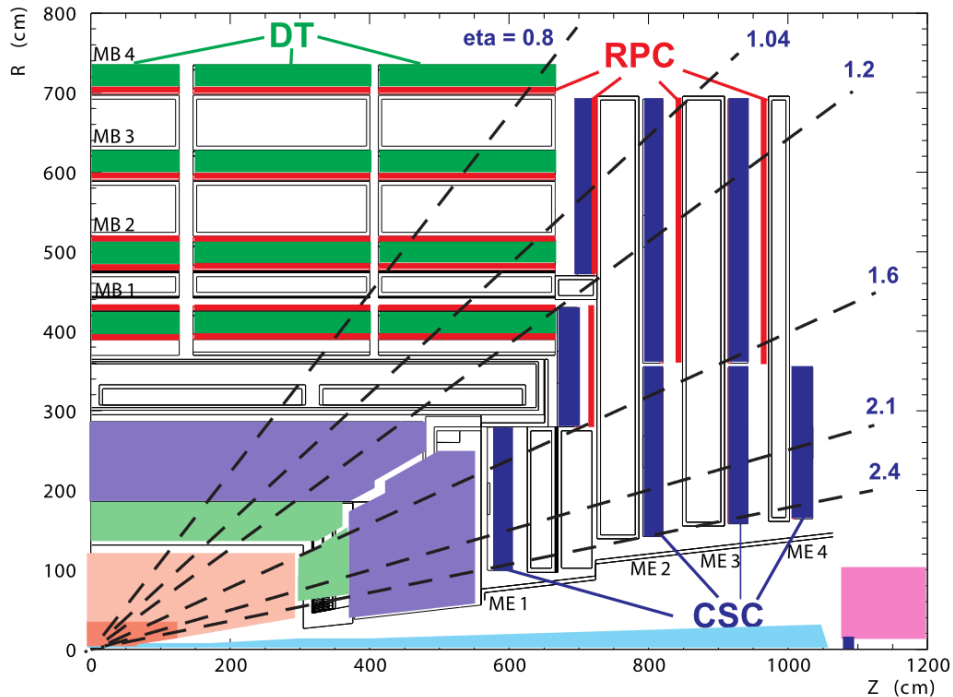


**Figure 4.7** The muon system of the CMS with its sub components. Taken from Ref [78].

a high muons flux. The gas mixture in the CSC consist of 50%  $\text{CO}_2$ , 40% argon and 10%  $\text{CF}_4$ . Inside the CSC positively charged strips and negatively charged wires intersect perpendicular. The muons ionizes the gas and the positively and negatively charged ions are measured by the wires and strips. This provides a measurement of the muon position with a very high segmentation.

The resistive plate chambers are located throughout the entire muon system. These contain oppositely charged metal plates which measure the electrons from ionization, resulting in a fast measurement of the muon momentum. This system is used for trigger purposes only (see section 4.5).

All together, the muon system of CMS is able to measure muons with a high momentum resolution of 1 to 3% for muons with a transverse momentum of less than 100 GeV respectively maximal 7% for a  $p_T$  of less than 1 TeV and with a high efficiency of 94%-99% [79].

## 4.5 Trigger

The total amount of data produced at the CMS experiment exceeds most data storing capacities. With a bunch crossing frequency of 40 MHz, every 25 ns the proton bunches hit, with an average number of interaction of 32 [80], depending on the instantaneous luminosity. Each event creates about 1 MB of data, resulting in a far too high data stream [81]. To reduce the number of events that are stored for further analyses a dedicated trigger system has been installed. This trigger system makes real time decisions about whether to store an event or not.

## 4 Experimental setup

---

The trigger system at CMS consists of two stages [82]: The *level-1 Trigger* (L1) is hardware based and reduces the data rate to around 100 kHz. The main criteria for the trigger are the energy of particles and jets, the amount of missing energy, or the number of photons. With this information, the large background from soft QCD events is sorted out. The data selected is then stored in memory pipelines and further processed at the second stage. This *high-level trigger* is software based and uses information from all of the sub detectors. It reconstructs physical objects, such as electrons, muons or jets and sorts events into certain categories, like events with high energetic jets or leptons. The data output of the high-level trigger is around 100 Hz, meaning that only every millionth event occurring in the detector is stored.



## 5 Event reconstruction and object identification

The raw data obtained from the detector has to be transformed into physical objects. This section explains the main steps of the event reconstruction, beginning with the general *particle flow algorithm* in section 5.1. Next, the identification of muons and electrons, relevant for this analysis, is introduced in section 5.2 and 5.3, followed by a description of how a jet is identified from particle flow objects in section 5.4.1 and which calibration methods are used to increase the accuracy in section 5.4.2. Finally, the b-jet-tagging is introduced, an important technique to identify jets originating from b quarks.

Each kind of particle leaves a unique signature in the detector helping to identify it. Fig. 5.1 shows an overview over which particle interacts with which detector component.

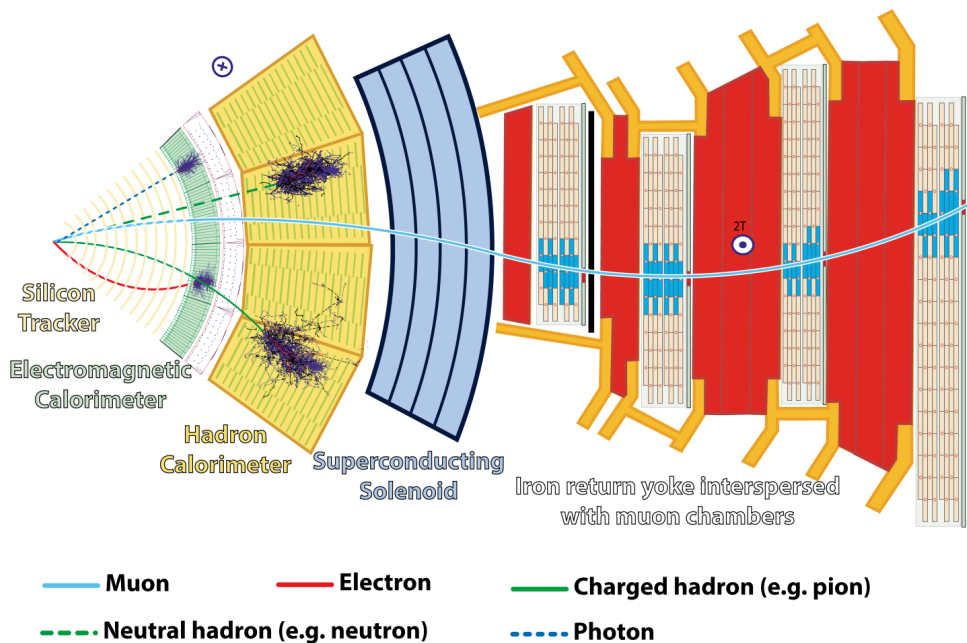


**Figure 5.1** Different types of particles interacting with the CMS detector. Taken from Ref [83].

The uppermost line represents a photon. Due to its electric neutrality, it can not be observed in the tracker but showers completely in the ECAL. A neutral hadron also travels through the tracker without a track, but showers in the HCAL rather than in the ECAL. A muon is visible in the tracker and in the muon system with only little interaction in both ECAL and HCAL. A charged hadron leaves a similar signature to the neutral hadron but is visible in the tracker. An electron showers in the ECAL and leaves a track in the tracker. To measure each particle optimally, a combination of all sub detectors is performed.

### 5.1 Particle Flow Algorithm

This combination of the information from different sub detectors at CMS is achieved by the *particle flow* (PF) reconstruction algorithm. The first step of the algorithm is to combine the

information of the individual hits in the tracker and the muon system. Two to three hits are used as seeds for a  $\chi^2$  fit of the particle's trajectory in an iterative procedure. With the trajectory of a particle the momentum, charge and vertex can be determined. Hits associated with particles fulfilling certain quality criteria are eliminated from the next iteration for which the quality criteria are gradually lowered.

In addition the showers in the calorimeters are analysed. Each calorimeter cell containing a certain minimum energy and more energy than all its neighbouring cells is used as a seed for a cluster. From this seed, all neighbouring cells containing an energy above a certain threshold are added to the cluster. This procedure is repeated until all cells directly next to a cluster cell contain only energy below the threshold.

Next, the different calorimeter clusters and tracks are combined. First, the ECAL and HCAL clusters are compared. Whenever the envelope around cluster of the HCAL contains the cluster of the ECAL, the two clusters are linked. Afterwards, the tracks and the ECAL/HCAL clusters are combined. The two objects are combined if the extrapolated path from the tracker ends in a cluster in the ECAL or HCAL. Furthermore, the photons originating from the bremsstrahlung of electrons bending in the tracker are matched to the corresponding electrons by analysing possible tangents at the electron path in the tracker. The found clusters and tracks are then combined and matched with the tracks from the muon system. As a last step, the remaining energy in the ECAL and HCAL are assigned to photons and neutral hadron respectively.

A typical event contains more than one vertex, because on average multiple protons interact. Therefore a primary vertex is defined by tracing all particle tracks reconstructed with PF back to their common origin and summing up their transverse momenta. The vertex with the highest momentum is referred to as the primary vertex. All other vertices found by the PF are referred to as pileup vertices.

With all the gathered informations, the *particle flow algorithm* identifies each set of clusters and tracks as a specific particle. This is done by using the different signatures by every particle explained in the previous section. A detailed description of the individual criteria and the PF reconstruction algorithm in general can be found in [84].

### 5.2 Muon identification

On the particles labelled as muons by the *particle flow algorithm*, further selection criteria are imposed. All selection criteria are designed to either increase the efficiency which comes at the cost of also increasing the misidentification rate (other particles wrongfully identified as muons) or vice versa. Several working points for selection criteria have been proposed by CMS [85]. The tightest one has been chosen for this analysis. This provides the smallest efficiency but also the lowest misidentification rate. The efficiency of the tight working point is well above 95% as shown in Ref. [79]. Each muon identified from the PF has to fulfil additional quality criteria,

for example the following:

- The path of the muon is reconstructed in the tracker and the muon system. Such muons are referred to as global muons.
- The global track fit matches a goodness of fit criterion (in this case  $\chi^2/\text{ndof} < 10$ ) where ndof is the number of degrees of freedom.
- At least one hit in the muon chamber is included in the muon track fit. This reduces the amount of punch through hadrons that do not deposit all their energy in the HCAL.
- At least one hit in the pixel detector. This suppresses muons from in flight decay.
- Hits in at least five different layers in the detector. This ensures a good accuracy of the measured  $p_T$ .

Furthermore, all muons are required to be isolated, which is defined by [79]:

$$I_{\text{rel}} = \frac{\sum_{h^\pm} p_T + \max(0, \sum_{h^0} E_T + \sum_{\gamma} E_T - 1/2 \sum_{h^\pm}^{PU} p_T)}{p_T^\mu} < 0.15 \quad (5.1)$$

where the sums run over all charged hadrons, neutral hadron, photons and estimated pileup in a cone with radius  $R < 0.4$ . This isolation criterion is used to differentiate muons that originate from weak interaction in jets.

In addition, muon are required to have  $|\eta| < 2.4$  and a  $p_T > 20\text{GeV}$ . The  $p_T$  criterion will be further discussed in section 6.3.1.

### 5.3 Electron identification

For electrons, a very similar procedure as for the muons is applied. Requirements for the electrons include similar general points as for the muons, e.g the total number of hits, but also include the ratio of energy deposited at the ECAL and the HCAL and the shower shape in  $\eta$  direction. The efficiency for electrons ranges from 90% to 97% depending on the pseudo rapidity [86]. The  $I_{\text{rel}} < 0.15$ ,  $p_T > 20\text{GeV}$  and  $|\eta| < 2.4$  criteria are the same as for the muons since the performance and the expected kinematics are very similar. Again the tightest of the CMS working points is chosen [87].

### 5.4 Jets

High  $p_T$  quarks can radiate off gluons, which in term can then from quark-antiquark pairs and start parton showers. Below an energy threshold, quarks and gluons hadronize and form colour neutral states by building groups. In a detector these hadronized particles are measured rather than the particle initiating the hadronization. A collection of the reconstructed particles from

such a hadron shower is called a *jet*. To define a jet from a collection of hits, different jet clustering algorithms are used.

### 5.4.1 Jet clustering

In this thesis the *anti- $k_t$*  algorithm is used [88].

The anti- $k_t$  algorithm clusters jets from particle four-vectors depending on their transverse momentum. For this purpose a distance parameter  $d_{ij}$  is defined between two particles:

$$d_{ij} = \min(p_{Ti}^{2n}, p_{Tj}^{2n}) \frac{\Delta_{ij}^2}{R^2} \quad (5.2)$$

where  $\Delta_{ij}$  is the distance in the  $\phi$ - $y$ -plane:

$$\Delta_{ij}^2 = (y_i - y_j)^2 + (\phi_i - \phi_j)^2 \quad (5.3)$$

with the rapidity  $y$ . The parameter  $n$  and  $R$  are free parameters of the algorithm, changing its behaviour. For this analysis,  $n$  is set to -1, the definition of the anti- $k_t$  algorithm. By choosing different values for  $n$ , other clustering algorithms are defined. For the  $k_t$  algorithm  $n$  is set to +1, and for the Cambridge/Aachen algorithm it is set to 0, completely ignoring the transverse momentum. A second quantity is defined as:

$$d_{iB} = p_{T,i}^{2n} \quad (5.4)$$

which can be understood as the distance in transverse momentum between the jet and beam. First, all  $d_{ij}$  and  $d_{iB}$  values are calculated. The smallest one is found; if it is a  $d_{ij}$  value, the objects  $i$  and  $j$  are added together into one object  $k$ , if it is a  $d_{iB}$  value, the object  $i$  is removed from the collection and stored as a jet. This procedure is done until all objects are clustered into jets.

One main property of the anti- $k_t$  algorithm is the clustering of low  $p_T$  objects to the nearest high  $p_T$  object first, rather than clustering them to each other. It produces circular, cone-shaped jets. The clustering behaviour of the anti- $k_t$  algorithm can be seen in Fig. 5.2. It can be seen that low  $p_T$  objects do not influence the cone structure. As seen in the case of the purple and green jets, a high  $p_T$  particle with low  $p_T$  particles around forms a jet by their own, leaving the low  $p_T$  particles to form another jet by their own.

The anti- $k_T$  algorithm is collinear- and infrared safe, meaning that the collinear splitting or the addition of a soft emission does not change the set of hard jets [89].

The radius parameter  $R$  changes the tendency for the jets to cluster at larger or smaller radii. For this analysis  $R = 0.4$  has been chosen.

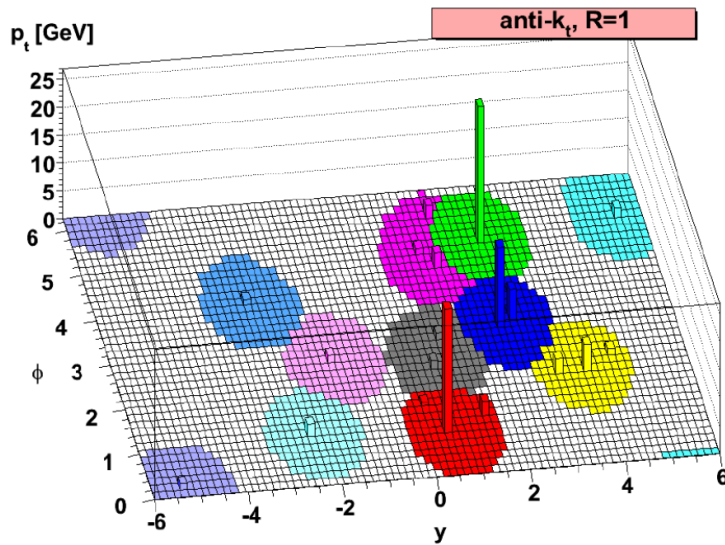


**Figure 5.2** A parton-level event clustered with the anti- $k_t$  algorithm. Each colour represents a different jet. Taken from Ref. [88].

### 5.4.2 Jet calibration

Corrections are applied to the measured jet energies to correct for systematic detector effects. For these *jet energy corrections* (JEC) the correction terms targeting different effects are factorised and individually be accounted for. The terms include correction of for example pile-up or the non-linear detector response.

To account for differences between simulated jets and measured jets in the jet energy resolution (JER), the simulated jets are further corrected to match the JER of the data.

Furthermore, certain quality criteria are applied. Similar to the criteria of muons and electrons, this quality criteria check things as e.g. the share of hadrons and leptons in a jet, or the number of hits in the HCAL. Again, the tight working point has been used, defined in Ref. [90].

Since prompt leptons clustered as jets lead to a double counting of the kinematic variables, a *jet-lepton cleaning* has been used to reduce this effect. To achieve this, the  $\Delta R$  between each jet and each lepton is calculated. If  $\Delta R < 0.4$ , the transverse momentum of the lepton is subtracted from the jet. This is done before jets with a  $p_T < 30\text{GeV}$  and  $|\eta| > 2.4$  are sorted out, so that leptons identified as jets are sorted out after losing most of there transverse energy from the jet-lepton cleaner.

### 5.5 Pileup mitigation

Since during each crossing several proton-proton collisions happen, the detector is confronted with particles from several collision vertices. These additional processes consist mainly of soft QCD interactions. They can distort the measured kinematic variables of the particles of interest. To mitigate the effects of pileup, the *pileup per particle identification* (PUPPI) is used [91]. PUPPI assigns a variable to each particle that differs greatly for pileup and the reaction products from hard scattering processes. This variable is calculated using kinematic informations of the particles and their relation to each other.

Based on the variable, a weight is assigned to each event ranging from 0 to 1, based on how likely this particle is a pileup particle. Values close to zero indicate that the particle originated from pileup, values close to 1 indicate the opposite. The weight is then used to rescale the four-momenta of the particles.

### 5.6 B-jet-tagging

Jets originating from b quarks can be distinguished from other jets by their distinct signature in the detector. They decay into either charm or up quarks. But since these decays are heavily suppressed by the respective CKM-matrix elements, b quarks form B mesons. B mesons have a lifetime of around  $1.5 \times 10^{-12}$  seconds, meaning they travel a certain distance from the primary vertex before decaying and forming a secondary vertex. This characteristic can be used to identify jets originating from a b quark, a process called *b-tagging*.

Multiple algorithms have been developed for this task. In this analysis, the DeepJet tagger [92] is used, based on a deep neural network. The algorithm uses the information on secondary and primary vertices as an input and returns a discriminator as an output. This discriminator takes values from 0 to 1, depending on how likely it is that the jet is a b jet. For this analysis, the medium working point has been used, with an efficiency of 82% to correctly identify b jets and a misidentification rate of approximately 1% for light-quark jets and gluon jets. [93].

---

## 6 Search for $A \rightarrow ZH(t\bar{t})$

In this chapter the analysis strategy is presented. For the analysis several sets of signal events have been simulated for different Higgs boson masses of the  $A \rightarrow ZH \rightarrow Zt\bar{t}$  channel.

In subsection 6.1 simulated signal and background samples are discussed. The signal samples have been simulated specifically for this analysis as part of this thesis. To distinguish the signal events from the background events, various object and event selections have been tested and applied. An overview of these can be found in subsection 6.3.2

For this thesis the pure hadronic decay of the top quarks and the leptonic decay of the  $Z$  boson has been studied. The signal topology of this  $l^+l^- + 6$  jets final state is discussed in subsection 6.4.

Subsection 6.5 will then review the statistical methods used in the analysis with which the exclusion limits have been calculated.

### 6.1 Signal and background samples

#### 6.1.1 The signal samples

The signal simulation consists of several steps.

- Production of the heavy Higgs boson  $A$ , only through gluon-gluon fusion.
- Decay of the  $A$  boson into a heavy Higgs boson  $H$  and a  $Z$  boson.
- Decay of the  $H$  boson into a pair of top quarks.
- Decay of the  $Z$  boson into a pair of muons. Contrary to the previous processes this branching ratio does not depend on the parameters. The branching ratio for this decay is approximately 3.4% [94].
- Hadronic decay of the top quarks. This branching ratio is known to be approximately 45.7% (see Ref. [95]).

A Feynman diagram of the process at leading order (LO) perturbation theory for this process can be found in Fig. 6.1. Choosing the hadronic decay results in a signature of six jets, the leptonic decay of the  $Z$  provides two opposite sign same flavour leptons (OSSF) in the final state.

To probe the relevant  $m_A$ - $m_H$ -parameter space, a total of 19 signal samples have been simulated. Those signal samples have been simulated inclusively to all top decays in order for them to be

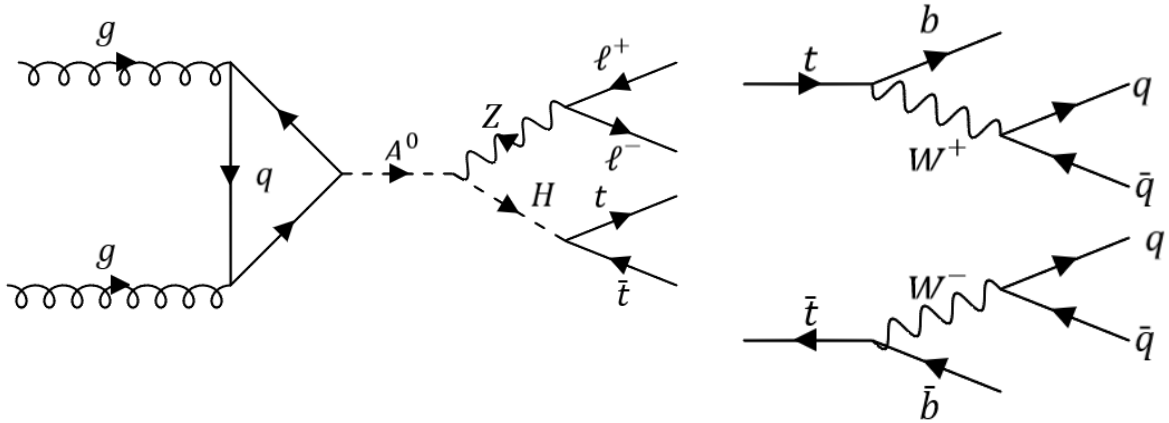


**Figure 6.1** Signal process with production mode (left) and further decay of the top system (right) analysed in this thesis.

reusable for future analysis probing different decay modes and to also take into account contributions due to migration from misreconstructed other top decay modes. Regarding the  $Z$  decay the samples have been produced only inclusive to the decay into electrons and muons. This choice was made since the hadronic decay of the  $Z$  loses the prominent OSSF-signature and the invisible decay into neutrinos is much harder to reconstruct. The focus of this analysis will also lie on muons since they can be reconstructed with a high precision at the CMS detector.

The samples have been simulated with MADGRAPH5\_aMC@NLO [96], using the 2HDM $t$ II\_NLO model [97], which is specifically designed for a type II 2HDM scenario. It features QCD corrections at next to leading order (NLO). This is important because of the gluon-gluon fusion production mode loop, not included in most leading order models. The top quark mass is assumed to be 172.5 GeV. The parton distribution functions (PDF) have been taken from the NNPDF3.1 set [98]. MADSPIN [99] has been activated for the decay of the  $H$  and the  $Z$  boson since MADGRAPH does not allow decay chains at NLO. All parameters apart from the masses, such as  $\tan(\beta)$ ,  $\cos(\alpha - \beta)$  and  $M_{H^\pm}$ , do not have a leading order influence on the kinematics of this decay channel. They were set to the values defined at the beginning of section 3. The cross section has not been calculated with MADGRAPH, but rather with equation 3.5. An overview over the chosen mass points can be found in Table 4. The column cross section lists the product of the  $A$  boson production cross section via gluon-gluon fusion and the decay  $A \rightarrow ZH$  with  $Z \rightarrow \mu\mu$  and  $H \rightarrow t\bar{t}$ :  $\sigma_{gg}(A) \times BR(A \rightarrow ZH) \times BR(Z \rightarrow \mu\mu) \times BR(H \rightarrow t\bar{t})$  For each signal sample a total number of 10,000 events has been simulated. The subsequent showering and hadronization has been simulated with Pythia8 [100]. The parameters for the underlying event description correspond to the CP5 tune [101]. The detector response is simulated using DELPHES [102], a fast detector response simulation. It simulates the response of a multi-purpose detector in a parametrized way, including effects like pile-up, the tracking system, hadronic and leptonic calorimeters and the muons system. Its main purpose is the fast and effective scanning



of a large parameter space rather than a high precision analysis. By reducing the computation time per event from around 100 s to 10 ms compared to a GEANT-based [103] full-sim [104], it enables the fast probing of different points in the parameter space, making it ideal for a first study of the analysis sensitivity presented in this thesis.

Interference between the signal and the Standard Model background has been studied in [12] and is expected to be small for the relevant kinematic distributions such as  $p_T^Z$ . Interference effects have therefore not been included in this analysis.

### 6.1.2 Background processes

Different Standard Model processes can have a similar topology as the signal and thus contribute as background. This section gives a brief overview over the different background processes and why they were considered.

Different Monte Carlo event generators are used to model the background events, depending on the process. With the generators POWHEG (v.2) [105–109] or MADGRAPH5\_aMC@NLO (v.2.4.2) (Ref. [96]), events are simulated at NLO, or with PYTHIA (v.8.230) (Ref. [100]) at LO. For all the background events the same assumptions as for the signal events regarding the top quark mass, the PDFs and the CP5 tune are made. For all background processes detector effects have been simulated using the GEANT-based full CMS detector simulation. The background samples have been centrally provided by the CMS Collaboration.

The  $t\bar{t}$  events are produced with POWHEG, the single top events with POWHEG or MADGRAPH, depending on the decay channel, QCD,  $t\bar{t}Z$ , W+jets and Drell-Yan with MADGRAPH and Diboson events with PYTHIA.

Irreducible background to the signal process is the  $t\bar{t}Z$  production. Irreducible in this context means that the  $t\bar{t}Z$  and the signal events share the exact same final state and differ only in certain kinematic variables, such as invariant mass distributions. Two example diagrams of this type of background can be found in Fig. 6.2 (top). With a production cross section of  $\sigma = 0.86$  pb and  $\sigma \cdot BR(Z \rightarrow \ell\ell) = 0.088$  pb it is comparatively small (NLO results from Ref.[110]). The Drell-Yan process (also referred to as Z+jets) is a second large contributor to the background. In a Drell-Yan two partons (e.g a quark and a gluon or a quark and an antiquark) react to form a Z boson. At higher orders an increasing number of jets can be emitted at some point of the process. A Drell-Yan process with 6 jets in the final state results the same topology as the signal but often without b jets.

A similar process is the production of a W boson plus jets. The mechanism is similar to the Drell-Yan process. The W boson decays into a lepton-neutrino pair, resulting in missing transverse energy from the neutrino. This topology is different to the signal, but still, through lepton misidentification, some events can be mistaken for a signal event.

Similarly, the production of a pair of top quarks and the single top production has both been

**Table 3** Inclusive cross sections for the most important background processes

Background sample	cross section [pb]	Ref.
QCD	$1.96 \times 10^8$	[111]
W+jets	3162	[112],[113]
$t\bar{t}$	832	[114]
Drell-Yan	271	[112]
Single top	237	[115]
Diboson	116	[112]
$t\bar{t}Z$	0.86	[110]

taken into account. Two exemplary Feynman diagrams for the  $t\bar{t}$  production can be found in Fig. 6.2 (bottom).

Depending on the further decay, the Diboson production can also result in a pair of leptons and a varying number of jets.

The largest fraction of background before the event selections comes from QCD processes. Its cross section is around nine orders of magnitude larger than e.g. the  $t\bar{t}Z$  production. Despite its large total rate the event selection can efficiently reduce it such that it plays only a minor role in the analysis. Due to initial and final state radiation, a large variety of final states is possible.

Table 3 gives an overview over all the used background samples and their respective cross sections. Of final importance are not only the cross sections but also the selection efficiencies. The relevant event yields after the selection are listed in Table 7

The event yields for both signal and background have been normalised to the Run-II luminosity of the year 2018 of  $59 \text{ fb}^{-1}$

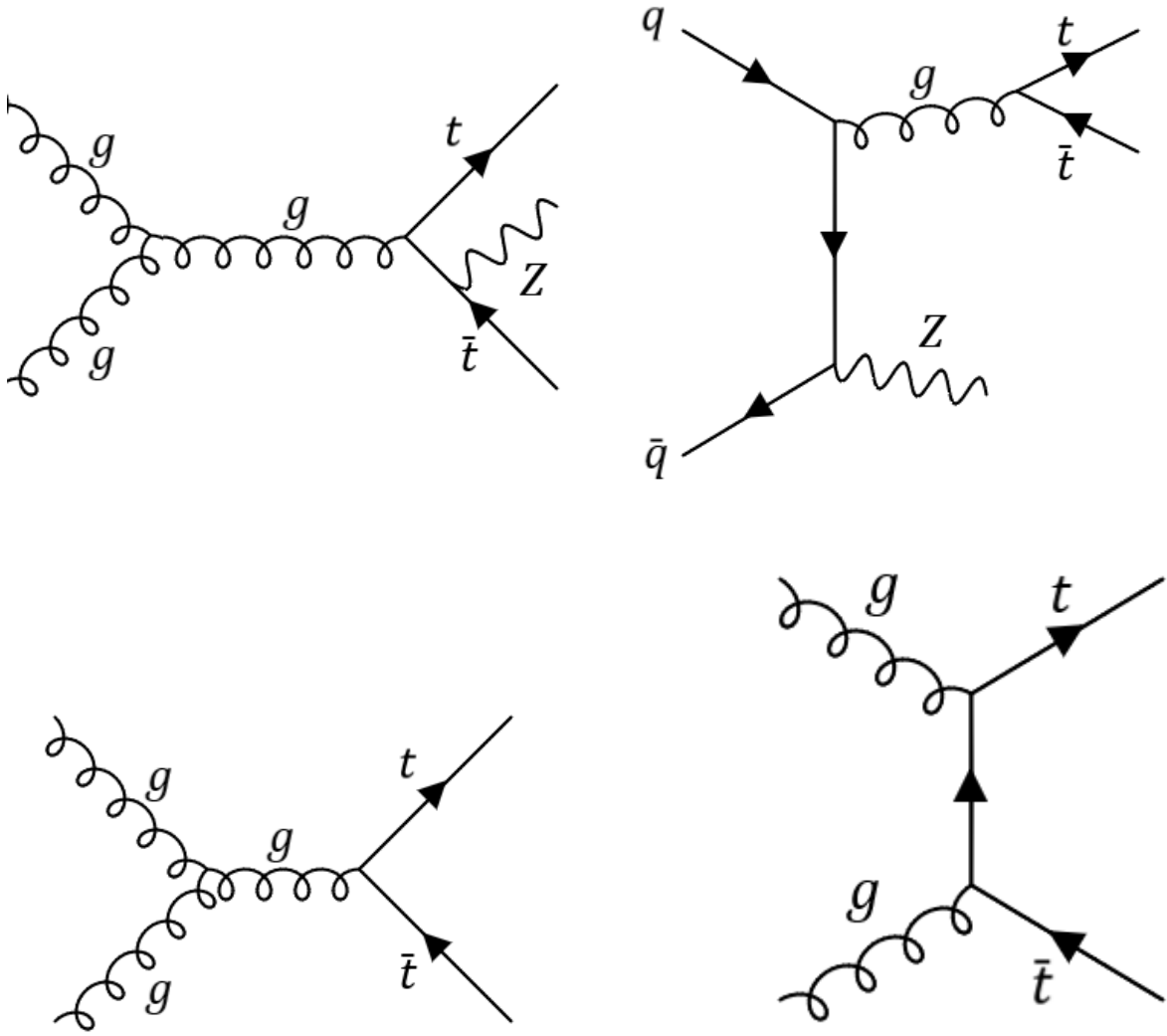


**Figure 6.2** Exemplary Feynman diagrams for several background processes. The upper two diagrams show the irreducible  $t\bar{t}Z$  background, the lower two diagrams show the dominant  $t\bar{t}$  background.

## 6.2 Signal topology at generator level

In this chapter the signal topology for different mass configurations of the heavy Higgs bosons will be discussed. A special focus will be set on the transverse momentum spectrum of the  $Z$  boson.

As a first step, the kinematic distributions of the signal samples have been studied at generator level, meaning after the parton shower and hadonization but before the inclusion of any detector effects. To highlight the differences and similarities between the signal, the irreducible  $t\bar{t}Z$  background and the largest background  $t\bar{t}$ , several kinematic observables are compared. Therefore, three mass configurations of the signal are chosen to represent three different points in the parameter space: One configuration with a large mass difference between the two Higgs bosons ( $m_A = 900$  GeV and  $m_H = 400$  GeV), one with a small difference but overall high masses ( $m_A = 800$  GeV and  $m_H = 700$  GeV) and one with medium values ( $m_A = 700$  GeV and  $m_H = 500$  GeV). For all samples the other parameters have been chosen as before, setting  $\tan(\beta) = 1$ ,  $\cos(\alpha - \beta) = 0$  and  $m_{H^\pm} = \max(m_A, m_H)$ . All of the distributions are normalized to unity

### 6.2.1 Jets

All processes discussed in this section involve a pair of top quarks. The (anti)-top quark will decay into a (anti)-bottom quark and a  $W^+$  ( $W^-$ ) boson. For the further decay of the two  $W$  bosons three different decay channels are open: The fully hadronic decay in which both  $W$  bosons decay into a quark-antiquark pair (this channel is shown in figure 6.1 (right)), the fully leptonic, in which both  $W$  bosons decay into one lepton and one neutrino each and the  $\ell + \text{jets}$ , in which one  $W$  boson decays into leptons and one into quarks. Since all analysed events are inclusive for all three decay channels, any jet multiplicity between 2 and 6 is expected at LO and ignoring acceptance ( $p_T, \eta$ ) effects. In Fig. 6.3 (top left) it can be seen that the jet multiplicity of the signal processes are in general higher than for the background processes. The reason for this is the higher transverse momentum spectrum (see Fig. 6.3 (top right)) of jets in signal events. A requirement of 30 GeV on the transverse momentum has been applied (see section 6.3.2). On average, more jets in signal than in background events fail this criterion resulting in a slightly higher jet multiplicity for the signal events.

The  $p_T$  spectrum of the jets shows the characteristic decreasing behaviour making high  $p_T$  jets unlikely. However, some differences between the signal and background processes can be observed. Compared to  $t\bar{t}$  production, the  $t\bar{t}Z$  spectrum is harder. This effect comes from the higher momentum transfer in the process that is necessary to produce a pair of top quarks and a  $Z$  boson.

The same can be observed for the signal events. The higher the mass of the  $A$  boson the higher the centre of mass energy and therefore the average transverse momentum of the jets.

A similar argumentation is true for the pseudorapidity  $\eta$ , defined in section 4.3. A higher

## 6.2 Signal topology at generator level

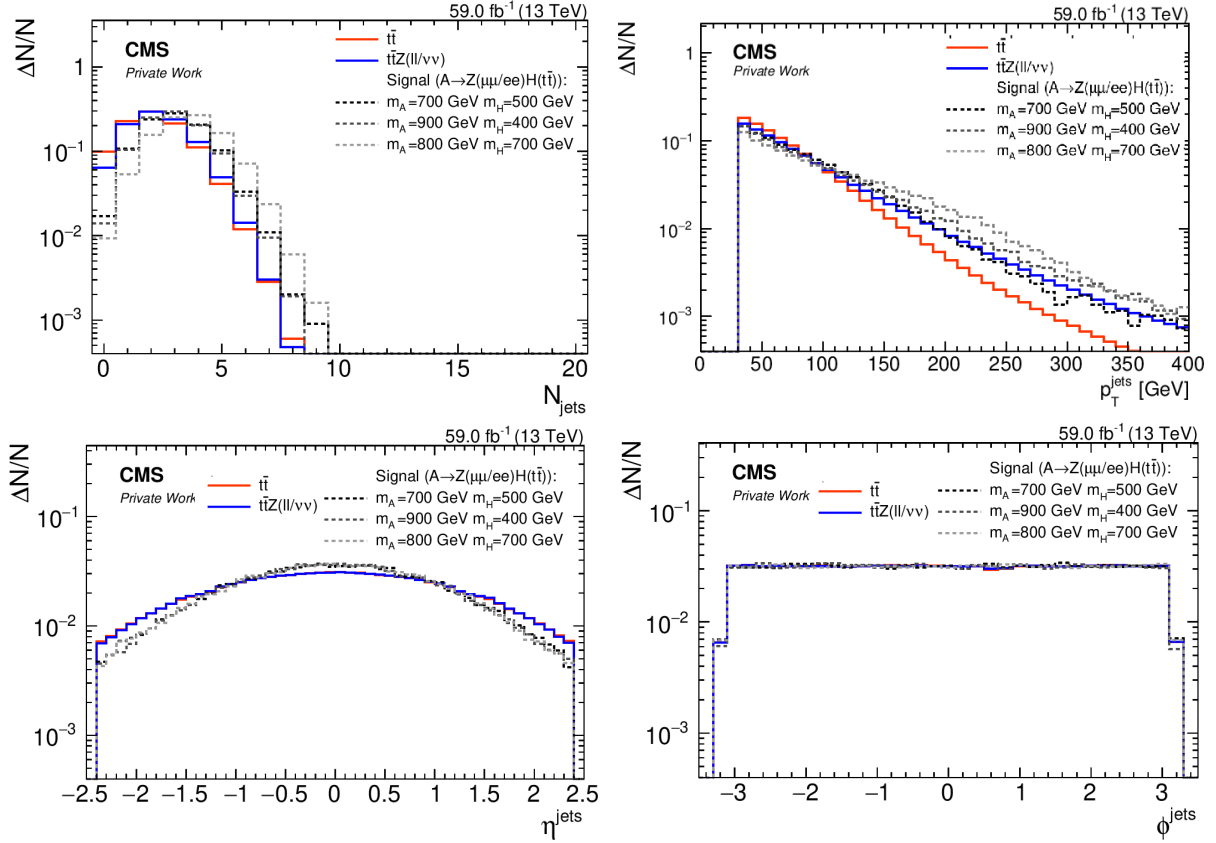


**Figure 6.3** Kinematic properties of generator level jets for the two main background and signal processes at three different mass configurations. Clockwise from the top left figure the multiplicity, transverse momentum, azimuthal angle and pseudorapidity are shown.

momentum transfer in the collision process generally leads to a more central production of the particles, due to kinematic effects explained in Ref. [116]. The  $\eta$  distribution of the heavy signal events shows a more steep decline towards higher values than the background events.

The distribution of the azimuthal angle  $\phi$  is a good cross check for any simulation errors. The distributions all show the expected uniform behaviour.

### 6.2.2 Muons

There are different sources for prompt muons in the signal processes: The  $Z$  boson decay and the top quark decay. For the  $t\bar{t}Z$  events, there are two possible decay paths leading to two muons in the final state: Either the top quarks decay into two muons and the  $Z$  boson decays into a pair of neutrinos, or the  $Z$  decays into muons and the top quarks decay hadronically. The number of muons for each process can be found in Fig. 6.4 (top left). The effects explained above are clearly visible, since most top quarks decay without any muons in their final state. Since the  $t\bar{t}Z$  samples have two possible decay paths leading to two muons and no electrons in the final state their fraction of no muon events is smaller. Independent from the masses, the three signal processes all show the highest numbers of muons in the final state, since they are produced

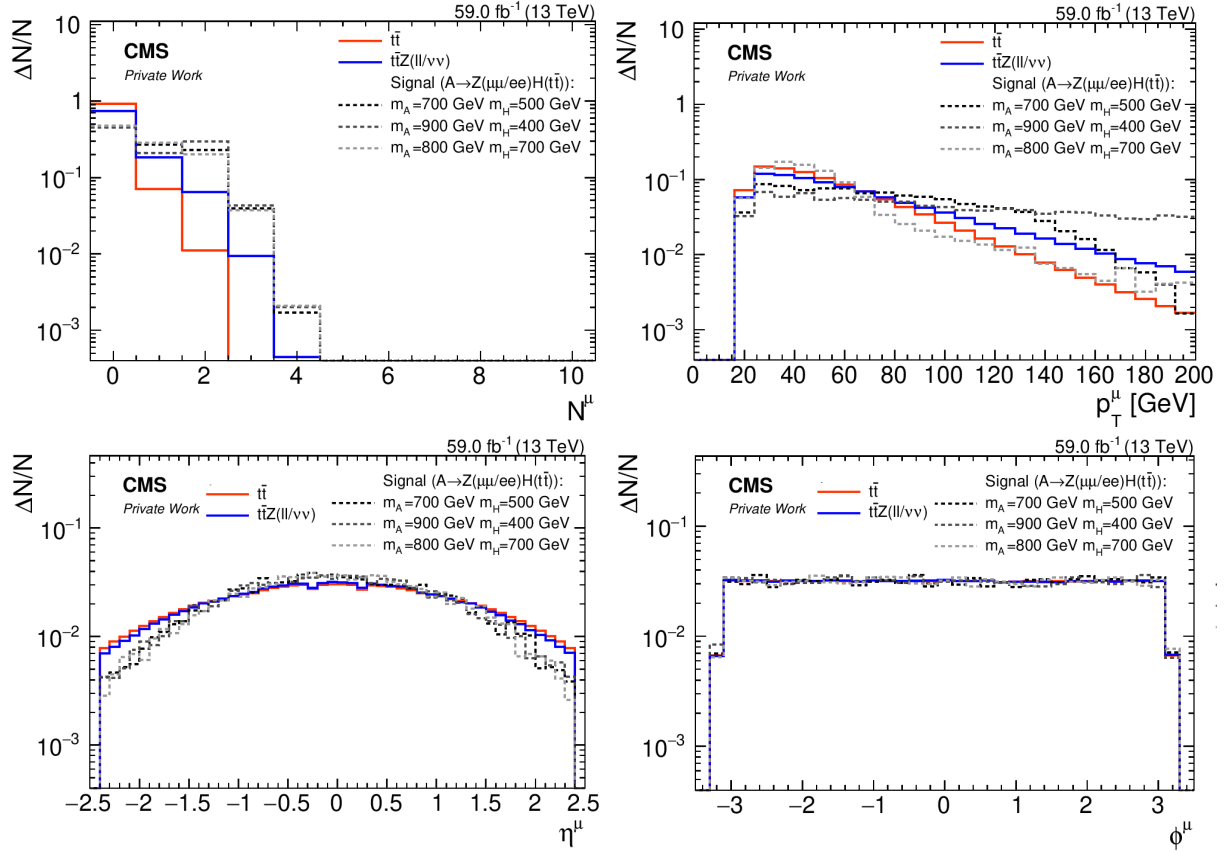


**Figure 6.4** Kinematic properties of generator level muons for the two main background and three signal processes at different mass configurations. Clockwise from the top left panel the multiplicity, transverse momentum, azimuthal angle and pseudorapidity are shown.

inclusively to only the leptonic decay of the  $Z$  boson.

The  $p_T$  spectrum of the muons is shown in Fig. 6.4 (top right). The most significant difference can be seen between the different signal mass configurations. For the process with  $m_A = 900$  GeV and  $m_H = 400$  GeV, the transverse momentum of the muons is the highest. The large mass difference between the two Higgs bosons results in a large amount of kinetic energy for the decay products. The smaller the mass difference, the less kinetic energy is transferred to the  $Z$  boson. Therefore, the  $p_T$  distributions tend to lower values for smaller mass differences.

Similar to the jets, the  $\eta$  distribution of the muons is more central for the signal events, since they are all produced at a higher momentum transfer compared to the background processes.

The  $\phi$  distribution is again completely uniform, showing no signs of asymmetry.

The two muons in the final state can be used to reconstruct the  $Z$  boson. The requirement of exactly two muons and no electrons in the final state reduces the number of muons originating from the top quarks. The invariant mass of the two muons is shown in Fig. 6.5 (left). For the signal and the  $t\bar{t}Z$  background events a prominent peak can be seen around the mass of the  $Z$  boson  $m_Z \approx 90$  GeV. For the  $t\bar{t}Z$  events the Lorentz shaped resonance profile is clearly visible. For the signal events, the Lorentz shape is cut off at the upper end. The occurrence of this

## 6.2 Signal topology at generator level

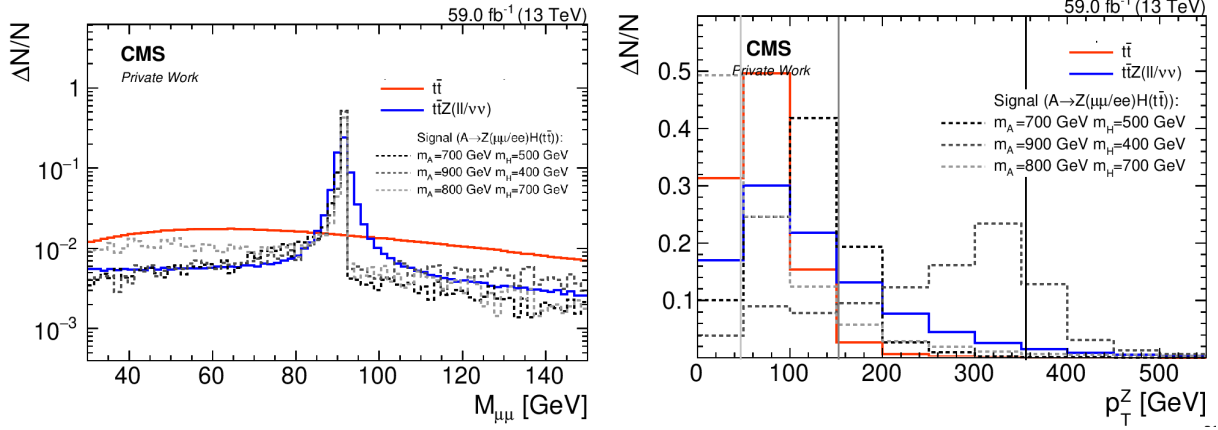


**Figure 6.5** Kinematic properties of sum of the two muon four-momenta. for the two main background and signal processes at three different mass configurations. The left plot show the invariant mass, the right plot the transverse momentum. The three vertical lines mark the theoretical prediction for the position of the edges.

edge is not yet fully understood, but attributed to the narrow width approximation used in the  $A \rightarrow ZH$  configuration. Left and right to the peak a plateau is reached with a gentle decline at higher values. The  $t\bar{t}$  events on the other hand do not show such a feature, but the distribution is rather monotonously falling for values larger than 50 GeV. Rejecting events outside the mass window of the  $Z$  boson therefore is an efficient way to minimize the number of background events involving no  $Z$  boson.

One key property for this analysis is the transverse momentum of the  $Z$  boson, shown in Fig. 6.5 (right). A characteristic edges in the signal distributions can be observed. The position of this edge varies for different masses of the Higgs boson masses. It can be calculated via the four momenta of the involved particles. In the rest frame of the heavy Higgs boson  $A$  its four momentum is  $P_A = (m_A, \vec{0})$ . The heavy Higgs boson  $A$  then decays into the  $Z$  and the  $H$  with their respective four momenta  $P_Z = (E_Z, \vec{p}_Z)$  and  $P_H = (E_H, \vec{p}_H)$ . Imposing conservation of the four momentum this yields  $P_A = P_Z + P_H$ . Rearranging for  $P_H$  and squaring yields:

$$P_H^2 = (P_A - P_Z)^2 = P_A^2 - 2P_A P_Z + P_Z^2 \quad (6.1)$$

Using the relativistic energy momentum relation  $E^2 = p^2 + m^2$  and as a consequence the fact that the squared four momentum gives invariant mass  $P^2 = m^2$ , the equation can be written as

$$m_H^2 = m_A^2 - 2m_A E_Z + m_Z^2 \quad (6.2)$$

which can be rearranged to

$$E_Z = \frac{m_A^2 + m_Z^2 - m_H^2}{2m_A}. \quad (6.3)$$

Exchanging  $E$  with  $\sqrt{\vec{p}_Z^2 + m_Z^2}$  and rearranging again, this yields

$$|\vec{p}_Z| = \frac{\sqrt{(m_A^2 + m_Z^2 - m_H^2)^2 - 4m_A^2 m_Z^2}}{2m_A} \quad (6.4)$$

This end result is in agreement with the formula for the  $p_T^Z$  edge in Ref. [12]. This edge marks the limit  $\eta \rightarrow \infty$  in which  $p \rightarrow p_T$ . This edge structure poses a substantial difference to the background  $p_T^Z$  spectra that peak at low values and decrease exponentially for higher transverse momenta. Therefore, this kinematic property combines several advantages as a discriminator. Signal and background distributions show a significant difference in shape, the measurement of this observable is comparatively easy as it can rely on the high precision muon tracking system of CMS. For these reasons the transverse momentum of the  $Z$  boson has been chosen as sensitive observable for the statistical analysis in this thesis. The expected position of the edges can be found in table 4.

**Table 4** Signal samples with their expected edges of the transverse momentum distribution of the  $Z$  boson according to equation 6.4 and their expected cross section.

$m_A$ [GeV]	$m_H$ [GeV]	$p_T^Z$ edge [GeV]	Cross section [fb]
1200	400	529	13.93
900	400	35	43.88
900	500	302	37.72
900	600	238	26.93
900	650	201	20.13
800	400	291	56.21
800	500	231	41.04
800	550	196	30.92
800	600	156	18.10
800	700	41	0.34
700	400	224	64.26
700	500	153	29.59
700	550	107	11.39
700	600	40	0.58
600	400	148	50.64
600	500	40	10.68
550	400	103	28.28
500	400	39	21.58

For the three signal mass configurations shown in Fig. 6.5 (right), the expected values obtained with equation 6.4 are in good agreement. Vertical lines have been inserted at the position of the expected edges. For the sample with the largest mass difference the edge is located at a momentum, where the background distribution decreased significantly. For the sample with



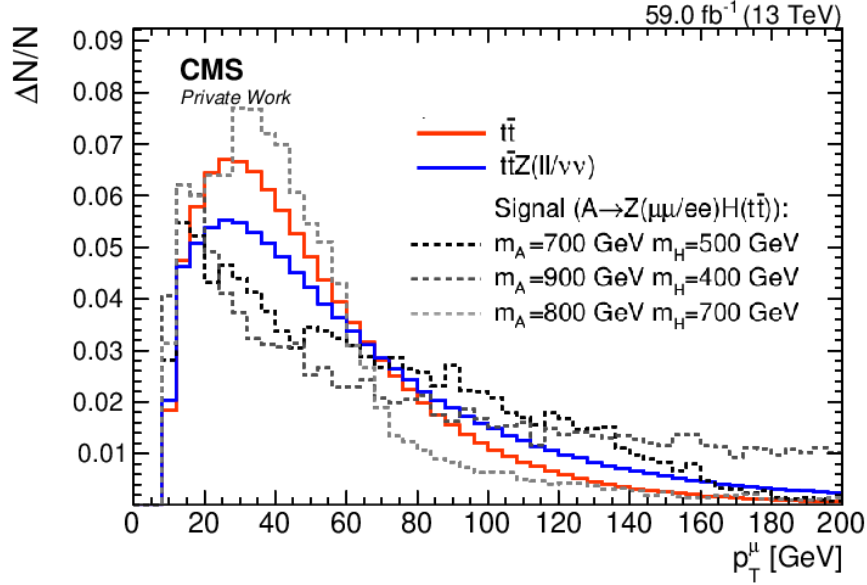


**Figure 6.6** Transverse momentum spectrum of muons on generator level with minimum requirement of 5 GeV.

$m_A = 700 \text{ GeV}$ ,  $m_H = 500 \text{ GeV}$  the edge is located in a region where the background is higher, but due to the distinct shape of the signal distribution the edge can be distinguished. Only the sample with the lowest mass difference has a significant overlap with the maxima of the backgrounds. Since its edge lays in the second bin the distribution as a whole is very compressed. A good acceptance rate of also low  $p_T$  muons will therefore be key to be to sensitive regions where the two Higgs boson masses are close to each other.

Following this motivation of the final observable  $p_T^Z$ , in the next step the reconstructed kinematic properties are studied, taking into account detector effects, such a misreconstruction, fake objects and uncertainties to the measured values.

## 6.3 Event selection

In this section, the different event selection criteria are discussed. Furthermore the  $p_T$  criterion of the muons will be analysed, since it effects the signal to background ratio significantly.

### 6.3.1 Minimal muon momentum

The transverse momentum criterion has been studied in detail before being fixed to the value of 20 GeV already given in 5.2. For this purpose the lower region of the transverse momentum spectrum of the muons has been analysed. It is displayed in Fig. 6.6. Some significant differences can be seen between the signal events at different mass configurations. For low

mass differences between the two heavy Higgs bosons the spectrum shows a high peak at values around 30 GeV before declining fast. For higher mass differences the spectrum gets harder and the tail at high momenta increases. Sorting out muons bellow 30 GeV would reduce the number of signal events significantly, especially for a low mass difference between  $A$  and  $H$ . To quantify this effect, the signal over  $t\bar{t}Z + t\bar{t}$  background ratio has been calculated for four different minimum values of transverse momentum. For those calculations the product of production cross section and all relevant branching ratios for  $A \rightarrow t\bar{t}\mu^+\mu^-$  were set to 0.1 pb. The results are displayed in Table 5. This table shows that a requirement of 30 GeV reduces the sig-

**Table 5**  $N_{sig}/\sqrt{N_{back}}$  for four different minimal transverse momenta of the muons after all event selections

$m_A$ [GeV], $m_H$ [GeV]	$p_T > 5$ GeV	$p_T > 20$ GeV	$p_T > 30$ GeV	$p_T > 50$ GeV
900, 400	28.8	30.9	32.4	34.2
700, 500	23.6	25.3	22.1	15.5
800, 700	23.3	24.1	18.6	10.4

nal over background ratio for all mass configurations except for the one with the highest mass difference. This is in agreement with Fig. 6.6, where the graph of the two signal samples with smaller mass difference lay under the graph of the background, meaning that eliminating events from this region reduces the background more than the signal. The opposite is true for the mass configuration with the highest mass difference.

From the examined  $p_T$  values the one at 20 GeV shows the best signal to background ratio for the majority of the mass points. For further improvement, different  $p_T$  requirements for different mass point could be included. For this analysis a general requirement of 20 GeV has been chosen since it improves the signal to background ratio especially for the difficult region with low mass differences that are generally more vulnerable to the kinetic requirements of the muons resulting in a lower signal acceptance rate. Furthermore, a dilepton trigger with a minimum  $p_T$  of 20 GeV is available at CMS.

It should be further noticed that by rejecting muons from the region between 5 GeV and 20 GeV, a difference in signal acceptance between the different signal points is created. This is the reason for the difference in the total number of signal events after applying all event selections as shown in Table 7.

### 6.3.2 Event selection

Ideally, a selection criterion sorts out as many background events as possible while on the other hand most of the signal events should pass it. This is of course just the ideal scenario. In reality, misreconstruction and other detection errors occur and no selection will allow all signal events to pass or sort out all backgrounds. Therefore each selection should be checked for its

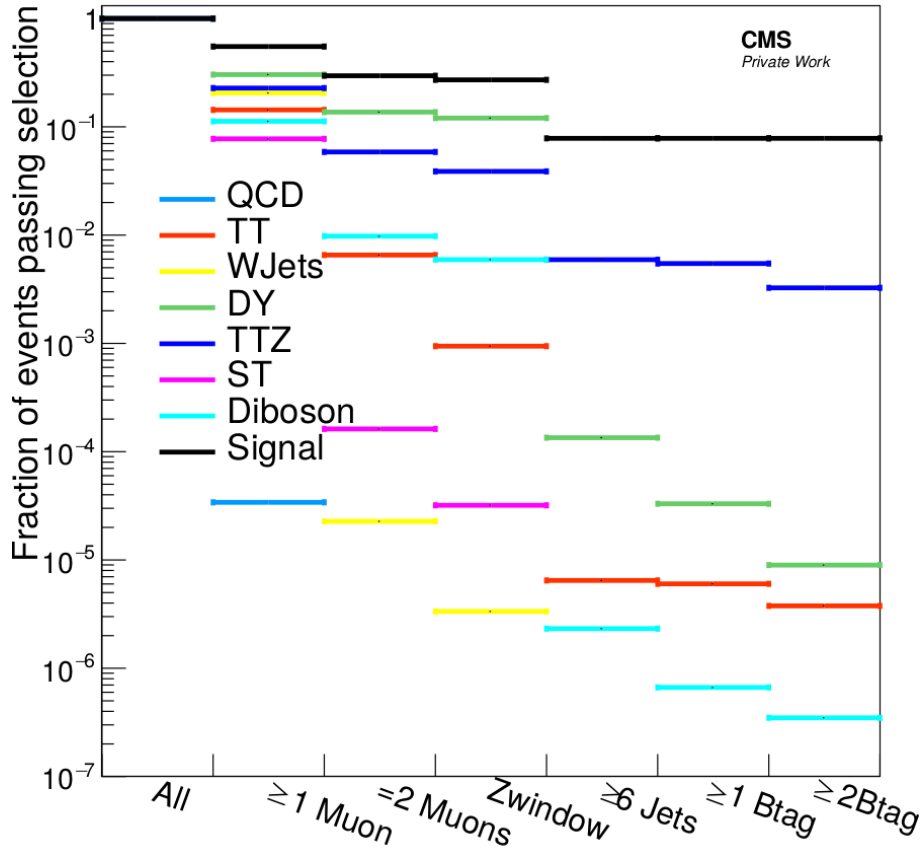


**Figure 6.7** Number of events after each criterion divided by the total number of events. Different colours represent the seven background processes that have been examined in this analysis. Black represents a signal process with  $m_A = 700 \text{ GeV}$  and  $m_H = 500 \text{ GeV}$ . Statistical error bars are present, but too small to be visible.

efficiency.

Since the final state of this analysis includes a pair of muons originating from a  $Z$  boson, the first event selection step is the requirement of exactly two muons in the final state with opposite charge. Furthermore, there should not be any other source of leptons in the event, so all events containing an electron are vetoed. As shown in Fig. 6.5, the invariant mass of the muon pairs is also expected to be close to the  $Z$  boson mass when their four momenta are added together, so a selection around the mass of the  $Z$  boson has also been applied. To cover approximately  $1 \sigma$  of the width of the peak, the borders of the mass window have been set to  $80 \text{ GeV}$  and  $100 \text{ GeV}$ . To target the hadronic decays of the top quarks, a total of six jets, two of which b-tagged, is requested.

The selection efficiency of these criteria on the signal and background events can be seen in Fig. 6.7. Each bin represents the addition of another criterion. The y-axis shows the number of events passing the respective selection criterion divided by the total number of all events. The black bars represent the signal process, in this case a sample with  $m_A = 700 \text{ GeV}$  and  $m_H = 500 \text{ GeV}$  has been chosen to represent a mass point with no extreme properties.

In the first bin with no selections, signal and background yields are aligned at a value of 1 representing the normalisation with respect to the number of events without any requirements. The requirement of at least one muon and no electron leads to a decrease to around  $2/3$  for the signal. This probability equals the sum of the decay fraction of one top quark decaying into a muon, which is around 15% plus the decay fraction of the  $Z$  boson decaying into a pair of muons. Since the signals are produced inclusive only to electronic and muonic  $Z$  decays, this branching fraction is  $1/2$ , leading to a total fraction of 0.65 signal events with this topology. The  $t\bar{t}Z$  background decreases to around 0.25 which is the sum of the probability of one of the top quarks decaying to a muon, which is again 15% plus the probability of a  $Z$  boson decaying into a muon. Since for this sample the decay is simulated also including the neutrino decay, this probability is only approximately  $1/9$ . The  $t\bar{t}$  yield is reduced by a factor of approximately 0.15 with contributions mainly from the  $\ell$ +jets decay channel. The muon criterion has by far the strongest impact on the QCD background. The requirement of one isolated muon alone reduces the number of QCD events by four orders of magnitude. The second lepton criterion, requiring exactly two muons, reduces it by eight orders of magnitude in total, compensating the large cross section of QCD processes. The second selection reduces all processes involving a pair of top quarks because only the purely leptonic decay of the top quarks results in a pair of muons. The fraction for this equals the product of the probability of the purely leptonic decay (10.2%) and the probability for both leptons being muons ( $(1/3)^2 = 1/9$ ), which results in a branching fraction of only around 1%.

Rejecting all events where the invariant mass of two muons does not result in a value close ( $\pm 10\text{ GeV}$ ) to the mass of the  $Z$  boson results in a drop for all processes involving no  $Z$  boson. Especially  $t\bar{t}$  events are reduced by approximately one order of magnitude. The signal yield is only reduced by approximately 10%.

The requirement of at least six jets leads to a strong reduction in all channels. The Drell-Yan events are reduced by three orders of magnitude, since in their dominant production channel only one jet is expected at leading order, meaning that only at significantly higher orders, 6 jets are expected. The  $t\bar{t}$  events are reduced by also by a large margin, although slightly less than the Drell-Yan events. By requiring exactly two muons in the final state, only the leptonically decaying events are selected, setting the number of leading order jets to two. At leading order two jets are expected as a result from the bottom quark decays. After both the muon and the number of jets criteria, the total number of  $t\bar{t}$  events has been reduced by five orders of magnitude. The signal events are affected less by this criterion, since their jet multiplicity is shifted to higher values (see Fig 6.4).

The requirement of at least one/two b-tagged jets further reduces the number of Drell-Yan events by approximately one order of magnitude. For the  $t\bar{t}$  and the  $t\bar{t}Z$  events pattern similar to Drell-Yan can be observed. For both processes two b quarks are expected in the final state. The reduction represents the efficiency of the b-tagging algorithm, missing some of the b quarks.

**Table 6** List of selection criteria.

$p_T$ of muons	$\geq 20 \text{ GeV}$
$ \eta $ of muons	$\leq 2.4$
Number of muons	2
Charge of muons	$1 \mu^+, 1 \mu^-$
Invariant mass of muons	80 GeV-100 GeV
$p_T$ of electrons	$\geq 20 \text{ GeV}$
$ \eta $ of electrons	$\leq 2.4$
Number of electrons	0
$p_T$ of jets	$\geq 30 \text{ GeV}$
$ \eta $ of jets	$\leq 2.4$
Number of jets	$\geq 6$
Number of b-tagged jets	$\geq 2$

This b-tagging efficiency is not implemented properly in the DELPHES production for the signal processes, which is the reason they do not change after the b-tagging requirement.

So far no Trigger have been used, since only simulated data has been used at this point in this analysis. A dilepton high-level trigger path targeting the  $Z$  boson will be used when analysing real data. The complete set of object and event selections are summarized in Table 6. An overview of the background and signal event yields can be found in Table 7.

From this table the main backgrounds can be identified as  $t\bar{t}$ , Drell-Yan and  $t\bar{t}Z$ . The other backgrounds have been reduced to nearly zero. The signal events are reduced to 250-550 events, depending on their mass configuration. Higher masses  $m_A$  have a positive effect on the selection efficiency, because fewer jets and muons are sorted out from the minimum  $p_T$  requirement.

**Table 7** Singal and background event yields and their statistical uncertainties after applying all selection criteria.

Process	Number of events
<b>Background</b>	
W+jets	$1.1 \pm 0.4$
QCD	$1.9 \pm 0.3$
Single top	$3.3 \pm 0.7$
Diboson	$5.2 \pm 1.5$
$t\bar{t}Z$	$41.3 \pm 2.2$
Drell-Yan	$107 \pm 4$
$t\bar{t}$	$290 \pm 6$
<b>Signal</b>	
$m_A$ [GeV], $m_H$ [GeV]	
500, 400	$273 \pm 14$
550, 400	$250 \pm 14$
600, 400	$287 \pm 14$
600, 500	$315 \pm 14$
700, 400	$272 \pm 14$
700, 500	$278 \pm 14$
700, 550	$296 \pm 14$
700, 600	$284 \pm 14$
800, 400	$372 \pm 15$
800, 500	$438 \pm 16$
800, 550	$411 \pm 16$
800, 600	$392 \pm 16$
800, 700	$361 \pm 15$
900, 400	$495 \pm 16$
900, 500	$469 \pm 16$
900, 600	$519 \pm 17$
900, 650	$503 \pm 17$
1200, 400	$825 \pm 21$

## 6.4 Signal and background properties at detector level

The study of the events at generator level demonstrated that the  $p_T^Z$ -distribution poses a very sensitive variable for the  $A \rightarrow ZH$  process in agreement with the studies in [12]. The next section will discuss the kinematic distributions at reconstruction level after application of the event selection listed above.

For all following plots, the product of production cross section and the branching ratios  $A \rightarrow ZH$ ,  $H \rightarrow t\bar{t}$  and  $Z \rightarrow \mu^+\mu^-$  have been set to 0.1 pb for the signal events. This value has been chosen because it sets the total number of signal events after all requirements to a similar level as the summed backgrounds. Furthermore, this value lies within one order of magnitude to its theoretical prediction. In contrast to the generator level plots, the following plots are not normalized to show the expected yields of the various backgrounds.

The multiplicity of the jets shown in Fig. 6.8 (top, left) reflects the requirement of more than 6

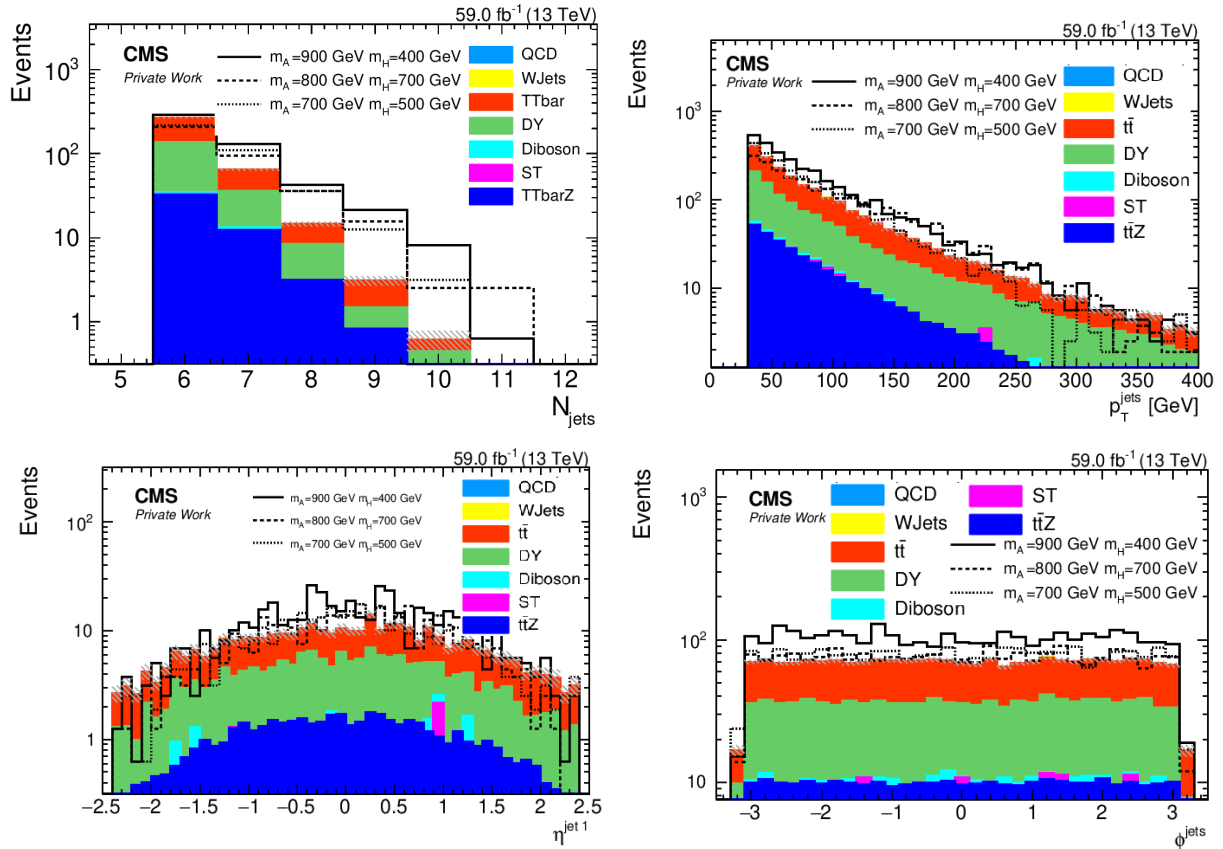


**Figure 6.8** Kinematic properties of reconstructed jets for all background and signal processes at three different mass configurations. The figures show clockwise beginning from the upper left figure the multiplicity, transverse momentum, azimuthal angle and pseudorapidity.

jets in the final state. The general shift of the signal towards a higher number of jets discussed in the previous section is also visible at reconstructed level. The  $p_T$ ,  $\eta$  and  $\phi$  spectra of the jets is in good agreement to its corresponding distributions at generator level shown in Fig. 6.3. Again, the signal events generally are produced at higher momenta and more central.

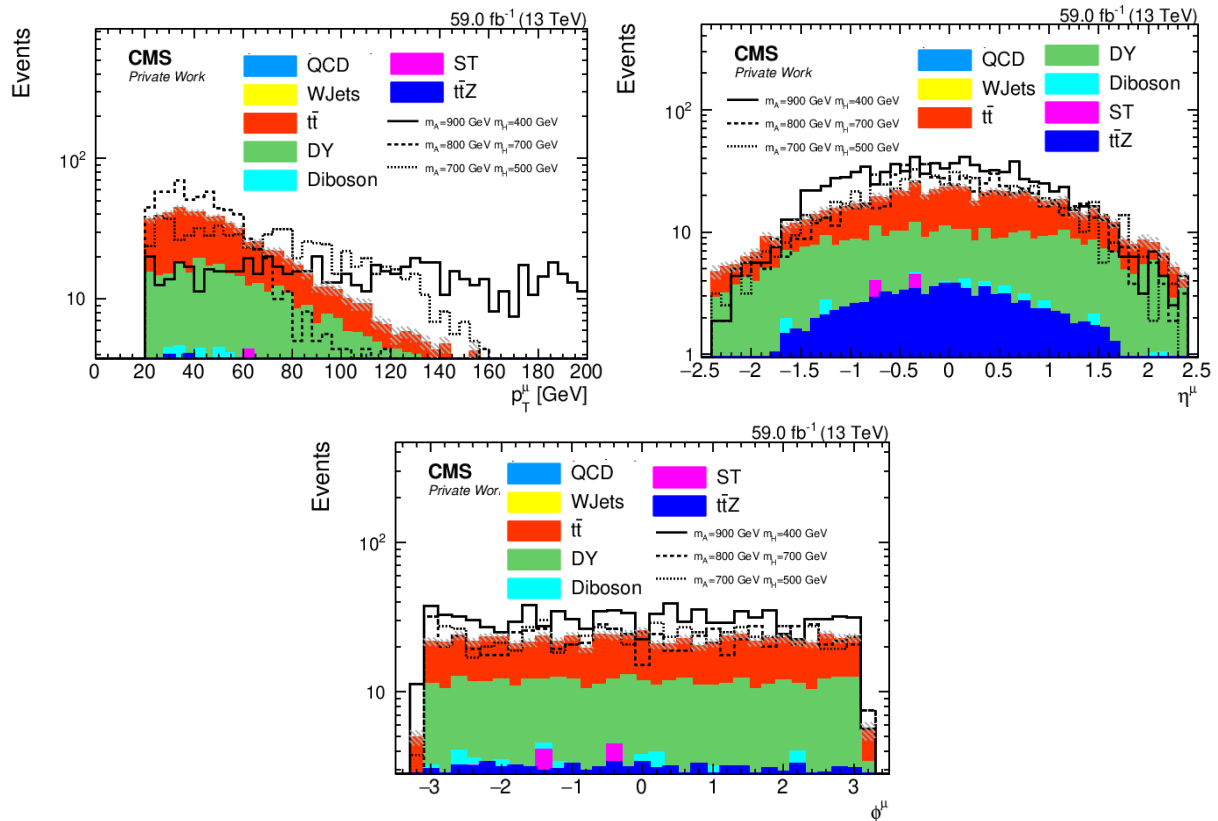


**Figure 6.9** Kinematic properties of reconstructed muons for all background and signal processes at three different mass configurations. The figures show the transverse momentum, pseudorapidity and azimuthal angle.

The  $p_T$  spectrum of the muons (Fig. 6.9) is very similar to the spectra at generator level. The Drell-Yan events contribute mostly to the lower  $p_T$  region, increasing the difference between the signal (especially with large mass differences) and background events even more. The  $\eta$  and  $\phi$  spectra are similar in shape compared to the generator level plots.

The invariant mass of the di-muon system (Fig. 6.10 left)) represents the sole acceptance of values between 80 GeV and 100 GeV. In this window all processes involving a Z boson, namely the signals, the  $t\bar{t}Z$  background and the Drell-Yan background, show a peak structure at the centre, while the  $t\bar{t}$  events are evenly distributed throughout the range. The transverse momentum spectrum of the reconstructed Z boson can be seen in Fig. 6.10 (right). It becomes evident that the mass difference between the  $A$  and the  $H$  is crucial for the search in this kinematic variable. For a large mass difference as in the  $m_A = 900\text{ GeV}$  and  $m_H = 400\text{ GeV}$ , the peak is situated at 354 GeV in agreement with equation 6.4 and therefore at a region with very few background events, while the mass configuration  $m_A = 800\text{ GeV}$ ,  $m_H = 700\text{ GeV}$  peaks at only 41 GeV situated at the region with the most background events. All background processes show a similar behaviour for this kinematic variable: A peak at low  $p_T$  values ( $\leq 100\text{ GeV}$ ) and then an exponential decrease towards higher values.

A selection of more different mass points can be seen in Fig. 6.11). The left histogram shows



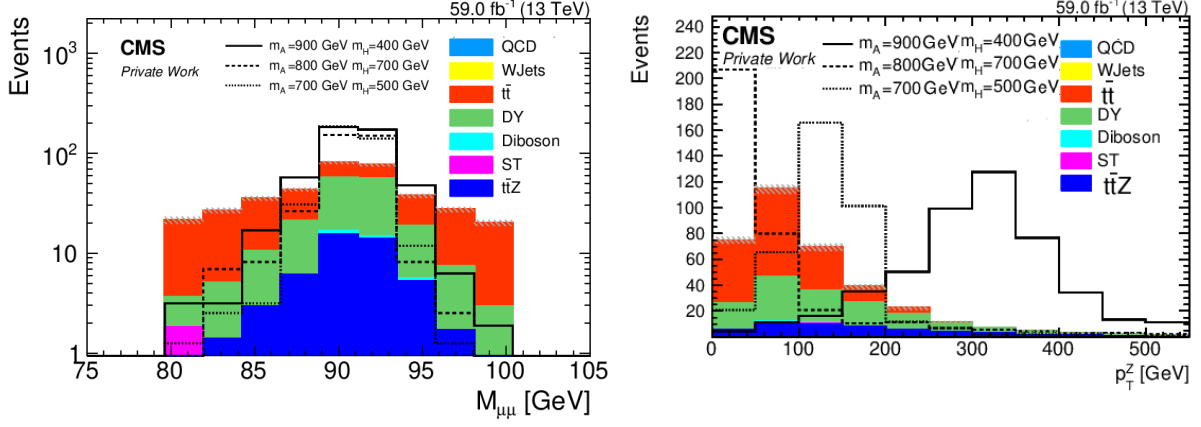


**Figure 6.10** Kinematic properties of the reconstructed Z boson. The invariant mass is shown on the left, the transverse momentum on the right.

three different masses  $m_H \in \{400 \text{ GeV}, 500 \text{ GeV}, 600 \text{ GeV}\}$  for a constant mass  $m_A = 800 \text{ GeV}$ . The edge in the  $p_T$  spectrum varies from 291 GeV to 41 GeV, showing its dependence on the mass difference between  $A$  and  $H$ . The right histogram further verifies this statement, showing a variation of both masses individually.

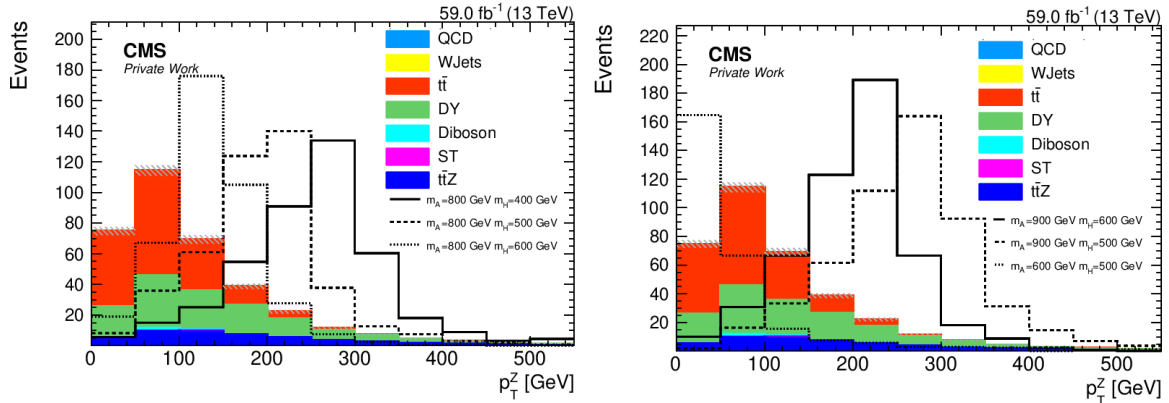


**Figure 6.11** Transverse momentum of the Z boson for signals with different mass configurations.

## 6.5 Results

This section will statistically quantify the found results. For this a brief introduction to the statistical analysis method used for this analysis is given. This explanation follows Ref. [117] (for the general statistics part only), Ref. [118] and Ref. [119]. After the introduction of the method, the expected exclusion limits for different mass points are presented.

### 6.5.1 The $CL_s$ technique

In particle physics, exclusion limits for a certain process mark the end of a parameter region in which this process can be ruled out by analysing the existing data. Above the exclusion limits, the process would have been seen as a significant deviation from the background. Past the exclusion limits, the deviation from the background is not significant enough and could as well be explained by statistical fluctuations and systematic uncertainties of the background.

In particle physics, the  $C_sL$  method is commonly used to derive exclusion limits. The basic concept is the likelihood of the data given hypothesis. This likelihood function acts as a measurement of how likely the result of an experiment can be explained by a given hypothesis. With only one data point  $n$ , this likelihood is just the result of this value plugged into the probability distribution  $P_H(x = n)$ . Most measurements in particle physics are counting experiments, meaning that the number of events in a fixed bin of an observable is counted. Let  $\lambda$  be the expected number of events in this bin under the tested hypothesis. The probability of counting  $n$  events in an experiment is then given by the Poisson distribution:

$$P(x = n) = \frac{\lambda^n e^{-\lambda}}{n!} \quad (6.5)$$

Let there be a set of  $k$  bins. The total likelihood of all bins is retrieved by multiplying all individual probability densities, resulting in the formula:

$$L = \prod_{i=1}^k \frac{\lambda^{n_i} e^{-\lambda}}{n_i!} \quad (6.6)$$

which is the definition of the likelihood function for a counting experiment. A search in particle physics generally features two hypotheses: A background only hypothesis  $b$  and a signal plus background hypothesis  $s+b$ . For both hypotheses, a likelihood function can be defined:  $L(b)$  and  $L(s+b)$ . For each set of measurements, a test statistic  $Q$  can be defined as:

$$Q = -2 \ln \left( \frac{L(s+b)}{L(b)} \right) \quad (6.7)$$

The better a given measurement agrees with the signal plus background hypothesis, the more this test statistic will decrease. Plotting the probability of each outcome as a function of  $Q$  under the assumption that either  $b$  or  $s+b$  is true results in a distribution similar to Fig. 6.12. A hypothetical measurement is shown as a red line, the areas under the background and signal plus background curve can be interpreted as different probabilities. The green area is the level of confidence for the signal plus background hypothesis  $CL_{s+b}$ . The bigger it is, the higher the probability of a false exclusion of the signal plus background hypothesis becomes. The yellow area on the other hand represents the false discovery rate  $1-CL_b$ . The bigger the area  $1-CL_b$ , the higher the discovery potential becomes and the bigger the area  $CL_b$ , the larger the exclusion

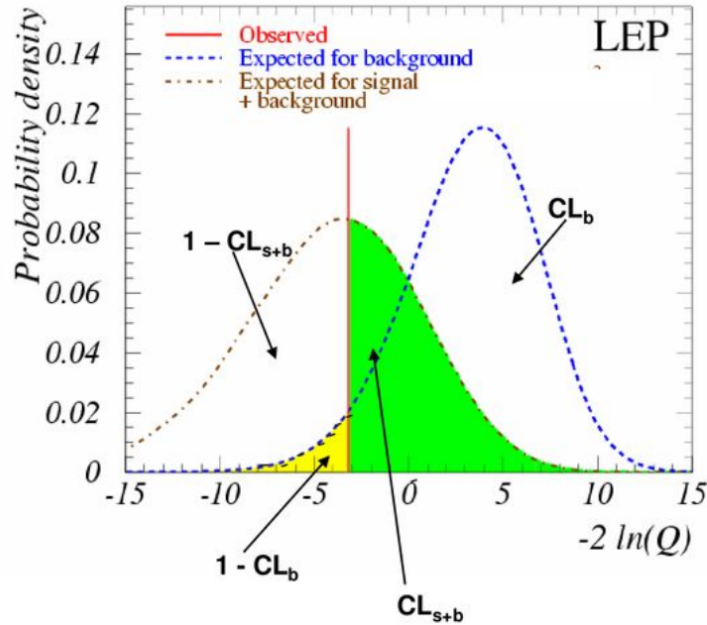


**Figure 6.12** Probability density for the test statistic  $Q$  Taken from Ref. [119]

potential. By introducing a signal strength modifier  $\mu$  as  $s \rightarrow \mu s$ , the cross section and with that the number of events for the signal distribution can be changed. By tuning this parameter slowly to zero, the signal plus background curve approaches the background curve. In this process the probability of wrongfully excluding the signal plus background hypothesis increases up to a point at which the analysis becomes practically insensitive to the signal. By extracting the value for  $\mu$  where this probability reaches a predefined point, an exclusion limit on the signal cross section can be defined.

However, this definition leads to some unphysical paradoxes e.g. negative exclusion limits, or the exclusion of a signal with a cross section of zero, especially when the background and the signal hypotheses lay close together (see Ref. [120] for more information.)

To solve those problems, the  $CL_s$  is defined as:

$$CL_s = \frac{CL_{s+b}}{CL_b} \quad (6.8)$$

All though this quantity is not strictly mathematically a confidence interval, it can be understood as an approximation for a signal-only confidence interval. By defining a confidence level for the signal-only, the problems mentioned above are solved.

To summarize the procedure: A given signal hypothesis can only be excluded if its cross section exceeds a certain value. Below this value, the probability of missing the signal in the background exceeds a certain predefined value meaning that a potential discovery would be overlooked because a contribution from the signal would lay in the range of the statistical Poisson fluctuations of the background. To calculate the minimum number of events that still can

be discovered with relative certainty, the signal strength is multiplied with a factor and the minimal values is extracted and can be transformed into a minimal cross section which can then be transformed into the desired kinematic variable, in this case for example the masses of the Higgs boson  $m_A$  and  $m_H$  or the  $\tan(\beta)$ .

The calculation of the limits, according to this method, has been done with the program Combine [121] using its function *Asymptotic limits*. Combine implements the explained  $CL_s$  method to calculate estimated values for the exclusion limits, relying on an asymptotic approximation of the LHC test statistic.

### 6.5.2 Systematic uncertainties

In addition to the statistical uncertainties, systematic uncertainties can affect the result of the measurement. In this thesis, systematic uncertainties on the cross sections of all background processes due to renormalization and factorisation scales and due to PDF uncertainties are considered. Furthermore, the uncertainty of the luminosity is considered for all background and signal events. The list of all uncertainties can be found in Table 8. All mentioned uncertainties

**Table 8** Cross sections for the most important background processes

Background process	QCD scale uncertainty	cross section PDF uncertainty
$t\bar{t}Z$	+8.1% / -9.3% [110]	$\pm 3.5\%$ [110]
Drell-Yan	2% [112]	0.2% [112]
W+jets	3.8% [112]	+0.8% / -0.4% [112]
$t\bar{t}$	+2.4% / -3.5% [114]	4.2% [114]
Single top	3.1% [115]	2.8% [115]
Diboson	3% [112]	5% [112]

are log normal distributed, meaning they influence the event yield directly. Further sources of uncertainty are b-tagging, jet energy scale, jet energy resolution or the lepton reconstruction efficiency. They are not yet considered in this version of the analysis.

To estimate the impact of the systematic uncertainties, for three exemplary mass points the limits have been calculated with and without those uncertainties. The results can be found in Table 9. For the largest mass difference, the edge in the  $p_T^Z$  distribution is expected at 529 GeV.

**Table 9** Impact of the systematic uncertainties on three limits.

$m_A$ [GeV], $m_H$ [GeV]	expected limit [fb] with uncertainties	expected limit [fb] without uncertainties
1200, 400	2.69	2.63
700, 400	7.03	6.87
500, 400	14.36	11.72

As shown in Fig. 6.10, in those regions there are only very few background events. Since the statistical uncertainty of a counting experiment is anti-proportional to the square root of the number of events, it is larger in regions with a low number of events. Systematic uncertainties on the other hand are often not effected by the number of selected events. For this reason the dominating uncertainty for the mass points with a large mass difference is expected to be the statistical one. This is reflected in the only minimal change between the two limits for this mass configuration. Going to smaller mass differences, the systematic uncertainties become more important as more background events fall into the region of the expected  $p_T^Z$  edge, lowering the statistical uncertainty. For the mass configuration just barely above the  $Z$  mass threshold, the systematic uncertainties change the limit by approximately 23%.

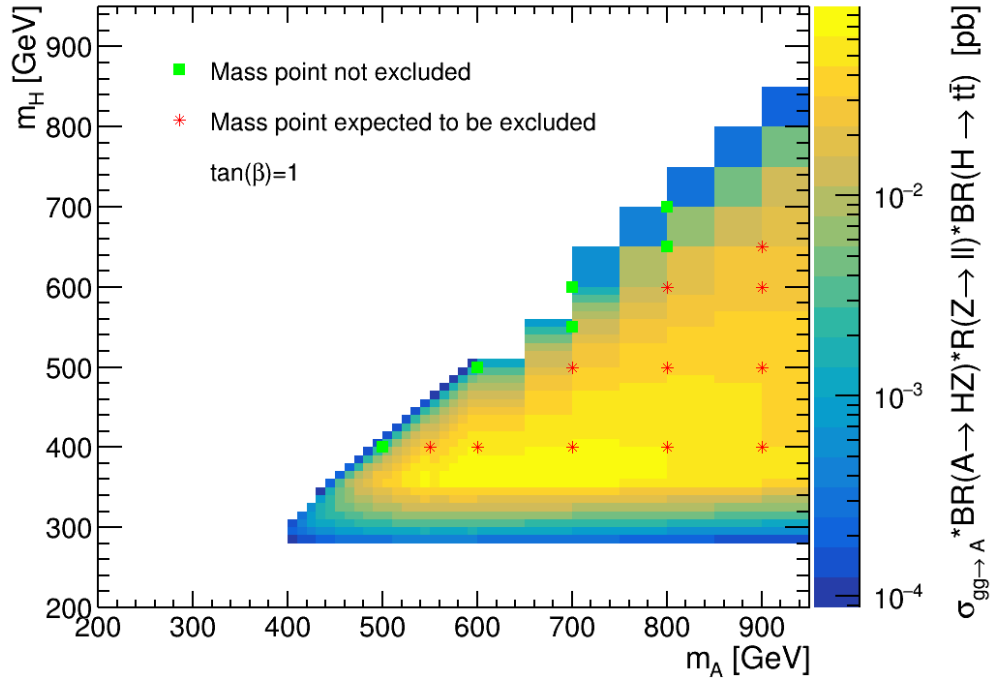
### 6.5.3 Expected exclusion limits

Upper exclusion limits at 95% CL on the  $A \rightarrow Z(\mu\mu)H(t\bar{t})$  cross section times branching ratio have been calculated for the different studied mass points. For this, histograms with the transverse momentum of the reconstructed  $Z$  boson for signal and background have been used as an input to `Combine` [121]. The *Asymptotic Limits* function outputs the exclusion limits at 95% CL and the one and two  $\sigma$  confidence intervals of this quantity. The limits have been calculated three times, once for the 2018 integrated luminosity of  $59\text{fb}^{-1}$ , once for the full Run-II luminosity of  $140\text{fb}^{-1}$  and once for the expected total luminosity after Run-III of  $300\text{fb}^{-1}$ . One motivation for the calculation of the exclusion limits at the expected Run-III luminosity was to compare the results with the theoretical predictions in Ref. [12]. They are listed together with the theoretical prediction of the cross section in Table 10. All mass points with a predicted cross section times branching ratio greater than the upper cross section limit can be considered as excluded. A graphical overview of which points on the mass plane are expected to be excluded with the 2018 data can be found in Fig. 6.13. The background in this plot is a colour scale representing the theory prediction cross section times branching ratio similar to Fig. 3.10, this time including also the branching ratio  $Z \rightarrow \ell^+\ell^-$  since the signal samples have been produced inclusive to only this decay channel.

The only points not excluded are all located at regions with low mass differences of 100 GeV-150 GeV. In this region, two main effects coincide: The production cross section and the branching fraction for the  $A \rightarrow ZH$  process decrease significantly as already discussed in section 3. Furthermore, the transverse momentum of the  $Z$  boson shrinks, resulting in the signal to be located in a part of the  $p_T$  spectrum with more background. This dependency on  $m_A - m_H$  is the main correlation noticeable in Table 10. Some minor effects regarding the absolute value of the individual masses can be seen as well: Higher masses have slightly lower exclusion limits. For example the mass point at  $m_A = 900\text{GeV}$  and  $m_H = 600\text{GeV}$  has an exclusion limit of 5.71 fb, while the mass point at  $m_A = 700\text{GeV}$  and  $m_H = 400\text{GeV}$  has an exclusion limit of 7.03 fb even though both mass points share the same difference. This trend can be observed for all sets

**Table 10** Predicted cross section times branching ratio and predicted exclusion limits for 2018 ( $59\text{fb}^{-1}$ ), Run-II( $140\text{fb}^{-1}$ ) and Run-III ( $300\text{fb}^{-1}$ ) luminosities.

$m_A$ [GeV], $m_H$ [GeV]	predicted cross section times branching ratio [fb]	exclusion limit at $59\text{fb}^{-1}$ [fb]	exclusion limit at $140\text{fb}^{-1}$ [fb]	exclusion limit at $300\text{fb}^{-1}$ [fb]
500, 400	2.2	$14.4^{+4.3}_{-3.8}$	$12.2^{+4.1}_{-3.6}$	$10.8^{+3.9}_{-3.4}$
550, 400	28.3	$12.1^{+4.1}_{-3.8}$	$10.0^{+3.9}_{-3.3}$	$8.1^{+3.3}_{-2.7}$
600, 400	50.6	$11.3^{+4.2}_{-3.8}$	$9.5^{+3.5}_{-2.9}$	$8.0^{+3.3}_{-2.7}$
600, 500	1.1	$11.6^{+4.1}_{-3.8}$	$9.7^{+3.9}_{-3.6}$	$8.1^{+3.2}_{-2.7}$
700, 400	64.3	$7.0^{+2.9}_{-2.5}$	$6.3^{+2.7}_{-2.1}$	$5.1^{+2.4}_{-1.9}$
700, 500	29.6	$9.8^{+3.0}_{-2.6}$	$7.8^{+2.6}_{-1.8}$	$6.2^{+2.4}_{-1.8}$
700, 550	11.4	$12.0^{+4.0}_{-3.8}$	$8.6^{+3.0}_{-2.7}$	$7.0^{+2.8}_{-2.5}$
700, 600	0.58	$14.3^{+4.1}_{-3.8}$	$11.5^{+3.9}_{-3.6}$	$9.7^{+3.7}_{-3.4}$
800, 400	56.2	$5.5^{+2.4}_{-1.6}$	$3.8^{+1.2}_{-0.9}$	$2.4^{+0.9}_{-0.5}$
800, 500	41.0	$7.3^{+2.9}_{-2.6}$	$5.9^{+2.5}_{-1.8}$	$5.2^{+2.3}_{-1.6}$
800, 600	30.9	$8.6^{+3.0}_{-2.8}$	$6.7^{+2.5}_{-2.1}$	$5.6^{+2.4}_{-1.7}$
800, 650	4.1	$9.4^{+2.9}_{-2.6}$	$7.6^{+2.6}_{-2.2}$	$6.1^{+2.3}_{-1.9}$
800, 700	0.34	$9.4^{+3.6}_{-2.8}$	$7.9^{+3.1}_{-2.8}$	$6.8^{+2.5}_{-2.3}$
900, 400	43.9	$4.0^{+2.7}_{-2.2}$	$2.6^{+1.1}_{-0.7}$	$1.8^{+0.7}_{-0.4}$
900, 500	37.7	$4.4^{+2.8}_{-2.2}$	$2.8^{+1.1}_{-0.8}$	$2.0^{+0.8}_{-0.5}$
900, 600	26.9	$5.7^{+2.4}_{-1.7}$	$4.1^{+1.8}_{-1.0}$	$2.8^{+1.0}_{-0.8}$
900, 650	20.1	$6.4^{+2.5}_{-2.2}$	$4.3^{+1.8}_{-1.0}$	$3.2^{+1.3}_{-1.0}$
1200, 400	13.9	$2.7^{+1.1}_{-0.8}$	$1.7^{+0.7}_{-0.5}$	$1.2^{+0.5}_{-0.2}$


**Figure 6.13** Expected exclusion limits on  $\sigma_{gg \rightarrow A} \times BR(A \rightarrow ZH) \times BR(H \rightarrow t\bar{t}) \times BR(Z \rightarrow \mu\mu)$  at 95% C.L. with 2018 luminosity of  $59\text{fb}^{-1}$ ,  $\tan(\beta) = 1$ ,  $m_{H^\pm} = \max(m_A, m_H)$ ,  $\cos(\alpha - \beta) = 0$ . Red asterisks mark points that are expected to be excluded, green squares mark points that are not excluded. The colour scale represents the predicted cross section times branching ratios.

of mass points with identical mass difference. The main cause for this effect is not the different position of the  $p_T^Z$  edge. Although equation 6.4 does not depend solely on the mass difference, the predicted position of the edge does not vary much for samples with the same difference. For the exemplary points above, the edge only changes from 238 GeV for the point at  $m_A = 900$  GeV and  $m_H = 600$  GeV to 224 GeV for the point at  $m_A = 700$  GeV and  $m_H = 400$  GeV. The larger impact on the limits poses the greater number of events surviving the different event selections, especially the requirement of six jets. For processes requiring a higher centre of mass energy the  $p_T$  spectrum of the jets is generally harder, meaning that more jets fulfil the minimal  $p_T$  criterion of 30 GeV. The total number of events after all selection criteria for different mass points, inter alia the two points mentioned above, can be seen in Table 7. The greater the number of events, the smaller the statistical uncertainty and therefore the better the expected exclusion limit.

Going beyond the highest masses  $m_A$  covered in this thesis, different effects are expected. Beyond 1000 GeV the production cross section for a heavy Higgs boson decreases significantly. At the same time the number of background events is expected to decrease further, resulting in generally lower exclusion limits. A further increase of the energy would at some point pose a problem to the analysis strategy as the reconstruction of the six highly boosted jet would become more and more difficult. For those reasons an investigation of the parameter space beyond 1000 GeV, that is not covered by this analysis, would be of interest.

Another aspect can be seen when comparing the exclusion limits for different luminosities. The Run-III luminosity and therefore the expected number of events is approximately 5 times larger than the 2018 luminosity. Since the statistical uncertainty of a counting experiment with  $N$  events scales with  $1/\sqrt{N}$ , the statistical uncertainty is expected to drop by a factor of  $1/\sqrt{5} \approx 0.447$ .

Comparing the results at different luminosities, this holds true for points with high mass differences, e.g.  $m_A = 1200$  GeV and  $m_H = 400$  GeV where the ratio is  $1.23/2.69 \approx 0.457$  or  $m_A = 900$  GeV and  $m_H = 400$  GeV with  $1.83/4.01 \approx 0.456$ . For these mass points the expected number of background events located at the  $p_T^Z$  edge is small, meaning that the main contribution to the limits comes from the statistical uncertainties rather than from the systematic uncertainties. For the mass points with a  $p_T^Z$  edge coinciding with the main background the statistical errors are much smaller, meaning that the systematic uncertainties are larger. Indeed the ratios are e.g.  $m_A = 500$  GeV and  $m_H = 400$  GeV with  $10.81/14.36 \approx 0.752$  or  $m_A = 800$  GeV and  $m_H = 700$  GeV with  $6.8/9.42 \approx 0.722$ . Higher luminosities would therefore be the most beneficial for the regime of large mass differences, where a lot of values are already excluded. The upper exclusion limits in the analysed region of the parameter space would therefore not benefit significantly from the higher expected luminosity of Run-III. Only one of the studied mass points (at  $m_A = 700$  GeV and  $m_H = 550$  GeV) can be excluded at  $300 \text{ fb}^{-1}$  while narrowly not being excluded at  $59 \text{ fb}^{-1}$ . The results for Run-II and Run-III are very similar. The same mass points are expected to be excluded at both luminosities.

Slicing parallel to the x-axis through Fig. 6.13 results in Fig. 6.14. This plot shows the predicted

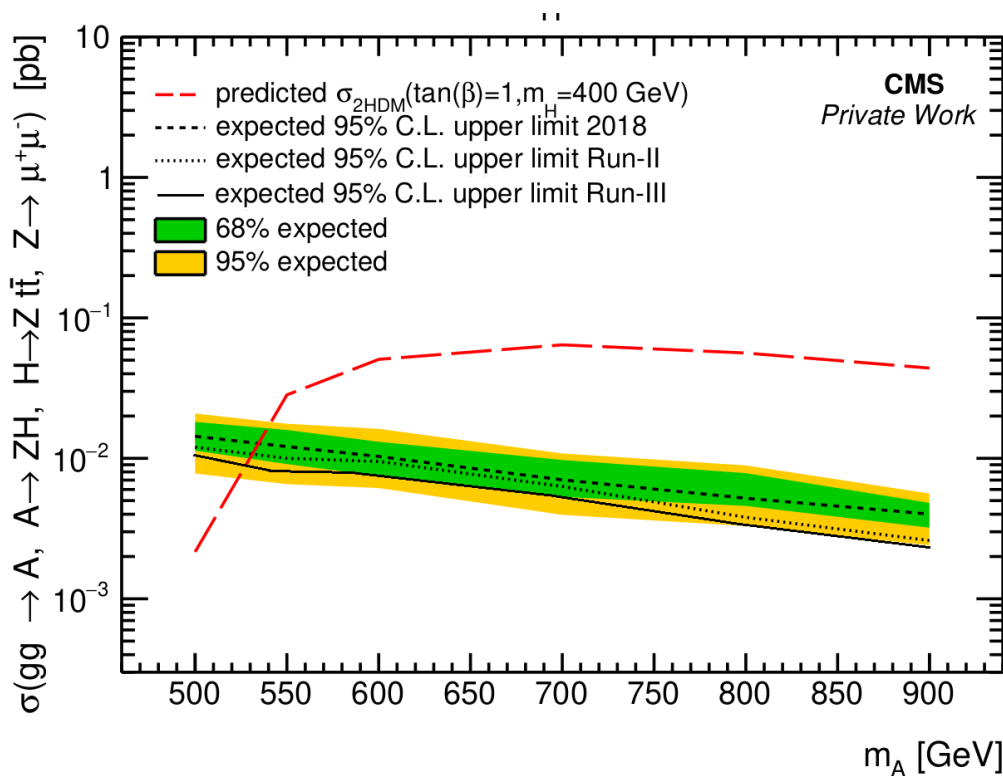


**Figure 6.14** Upper exclusion limits on  $\sigma_{gg \rightarrow A} \times BR(A \rightarrow ZH) \times BR(H \rightarrow t\bar{t}) \times BR(Z \rightarrow \mu\mu)$  at 95% C.L. and predicted theory cross section times branching ratio as a function of  $m_A$ .

cross section times branching ratio and the expected upper exclusion limit with its 68% and 95% confidence level bands. The regions where the predicted cross section runs above the expected limit is the excluded region. Near the threshold at 500 GeV the product of cross section and branching ratio is too small to be excluded. For higher masses this changes, making it possible to exclude a majority of the examined parameter space. For higher events a downward trend in the product of cross section and branching ratio becomes visible. This is due to the decreasing production cross section for the  $A$  boson, as explained in section 3. However, in the analysed mass region up to 900 GeV this decrease did not impact the exclusion of these regions.

Following the same principal, the expected exclusion limits with respect to  $\tan(\beta)$  can be determined. The result can be seen in Fig. 6.15 for fixed Higgs boson masses of  $m_A = 600$  GeV and  $m_H = 400$  GeV. The exclusion limit does not change with respect to  $\tan(\beta)$  since this variable does not affect the kinematic distributions directly. The predicted product of cross section times branching ratio on the other hand decreases dramatically at higher  $\tan(\beta)$ . The detailed discussion of this can again be found in section 3, the main reason is the decreasing branching ratio of the process  $H \rightarrow t\bar{t}$ . The two lines intersect at around  $\tan(\beta) = 2$ , excluding lower values. This intersection point varies for different masses. Two extreme examples can be found in Fig. 6.16. Fig. 6.16a shows a mass point that is barely not excluded at  $\tan(\beta) = 1$ . Lowering  $\tan(\beta)$  does increase the product of cross section and branching ratio by a small margin, but



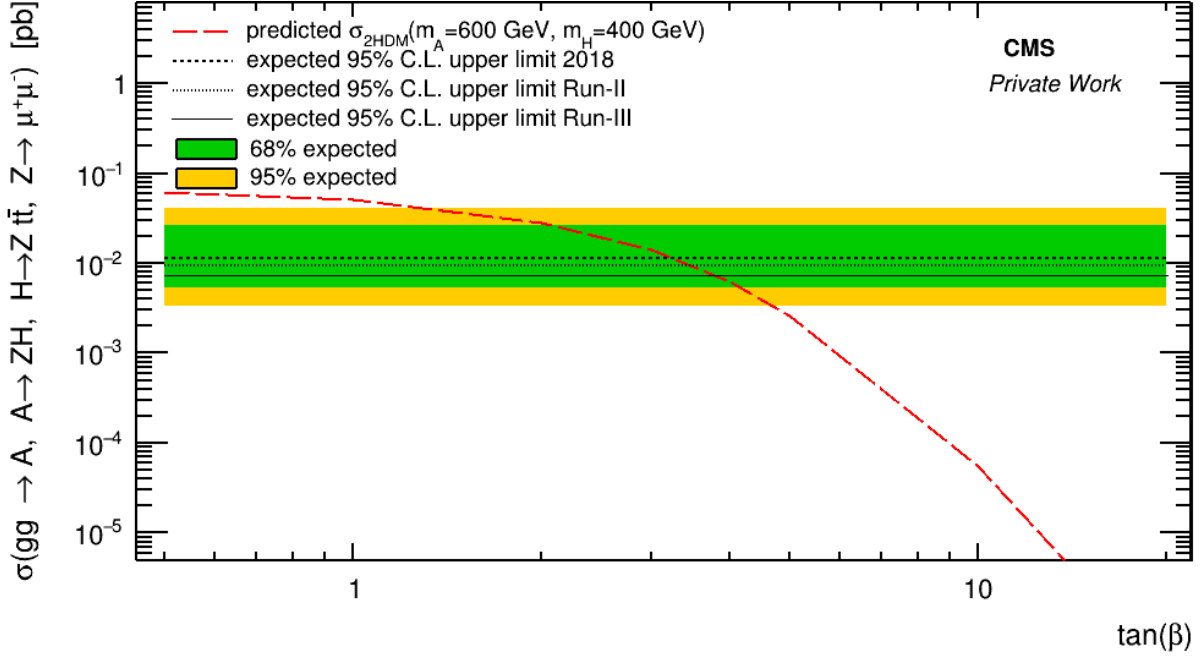


**Figure 6.15** Upper exclusion limits at on  $\sigma_{gg \rightarrow A} \times BR(A \rightarrow ZH) \times BR(H \rightarrow t\bar{t}) \times BR(Z \rightarrow \mu\mu)$  at 95% C.L. and predicted theory cross section times branching ratio as a function of  $\tan(\beta)$  at  $m_A = 600 \text{ GeV}$  and  $m_H = 400 \text{ GeV}$ .

since the branching ratio  $H \rightarrow t\bar{t}$  saturates at nearly 1, this effect is not sufficient to exclude this mass point at any of the observed  $\tan(\beta)$  values between 0.5 and 20.

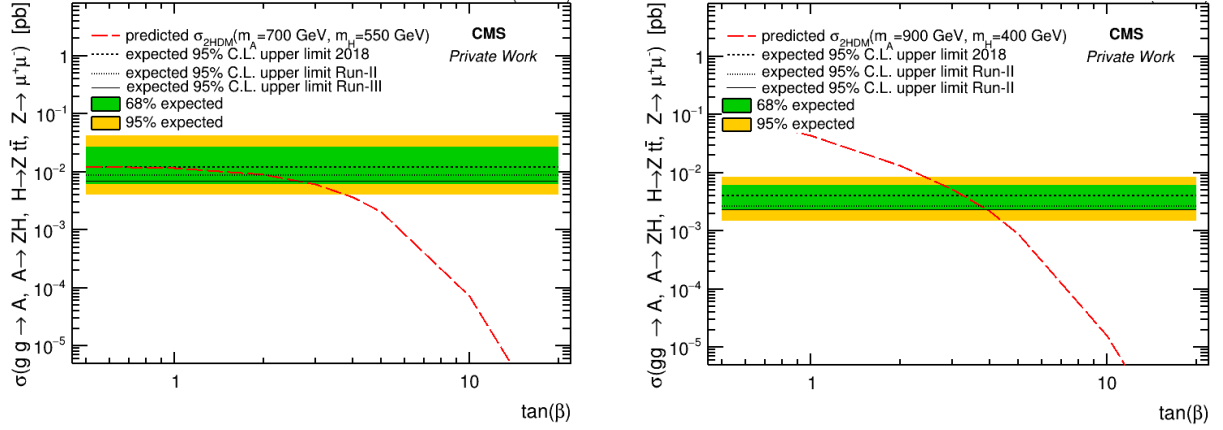
The graph in Fig. 6.16b shows a similar behaviour as in Fig. 6.15. The mass difference is much larger, but the intersection is still at approximately  $\tan(\beta) = 3$ . The main difference is the steeper shape of the curve. One reason for this is the production cross section that changes its shape and steepness with respect to  $m_A$ .

This rule holds true for most of the mass points at a high mass differences that are excluded. The intersection lies at  $\tan(\beta)$  values between 2 and 4. Since in this region the branching ratio  $A \rightarrow ZH$  already saturates at high values, the differences between the points is rather small. For the points that could not be excluded at  $\tan(\beta) = 1$ , there is no intersection in the analysed  $\tan(\beta)$  range.

A phenomenological study of the expected sensitivity can be found in [12]. This paper considers the  $A \rightarrow ZH \rightarrow Zt\bar{t}$  decay and uses the  $p_T^Z$  spectrum for the calculation of the limits. The main difference is the consideration of the  $\ell + \text{jets}$  decay of the top quarks, compared to the purely hadronic decay considered in this thesis. The exclusion plot taken from the paper can be found in Fig. 6.17.

Since the final state is not the same for both analyses, no exact quantitative agreement between Fig. 6.17 and Fig. 6.13 is expected. Still, qualitatively both figures show similar results. The excluded regions are both at rather high mass differences. Both plots show significant exclusions even for masses  $m_A$  up to 1000 GeV. Generally the exclusions in the conducted analysis show

## 6 Search for $A \rightarrow ZH(t\bar{t})$



(a) Upper exclusion limits and predicted theory cross section times branching ratio at  $m_A = 700$  GeV and  $m_H = 550$  GeV.

(b) Upper exclusion limits and predicted theory cross section times branching ratio at  $m_A = 900$  GeV and  $m_H = 400$  GeV.

**Figure 6.16** Exclusion limits on  $\sigma_{gg \rightarrow A} \times BR(A \rightarrow ZH) \times BR(H \rightarrow t\bar{t}) \times BR(Z \rightarrow \mu\mu)$  at 95% C.L. as a function of  $\tan(\beta)$  at different mass points.

a broader exclusion region. Table 10 lists a point at  $m_A = 1200$  GeV and  $m_H = 400$  GeV which is still excluded. At values for  $m_A$  this high, the plot from [12] does not show any exclusions. Furthermore, the highest excluded value for  $m_H$  (in the scenario  $m_H < m_A$ ) is at approximately 550 GeV while the analysis of this thesis expects exclusions up to at least 650 GeV. However, in both cases these highest values are reached at  $m_A$  around 900 GeV. One possible reason for the higher exclusion limits in this plot might be the very small background from  $t\bar{t}$  events, that are dramatically reduced by the requirement of two leptons in the  $Z$  mass window and six jets. In the  $\ell + \text{jets}$  channel a third lepton has to be taken into account in addition to missing transverse energy from the neutrino resulting from the top decay, a quantity not present in the decay channel of this analysis.

Taking into account the different final states, both results agree in the most important qualitative points, including the general shape and the exclusion favourability towards higher masses.

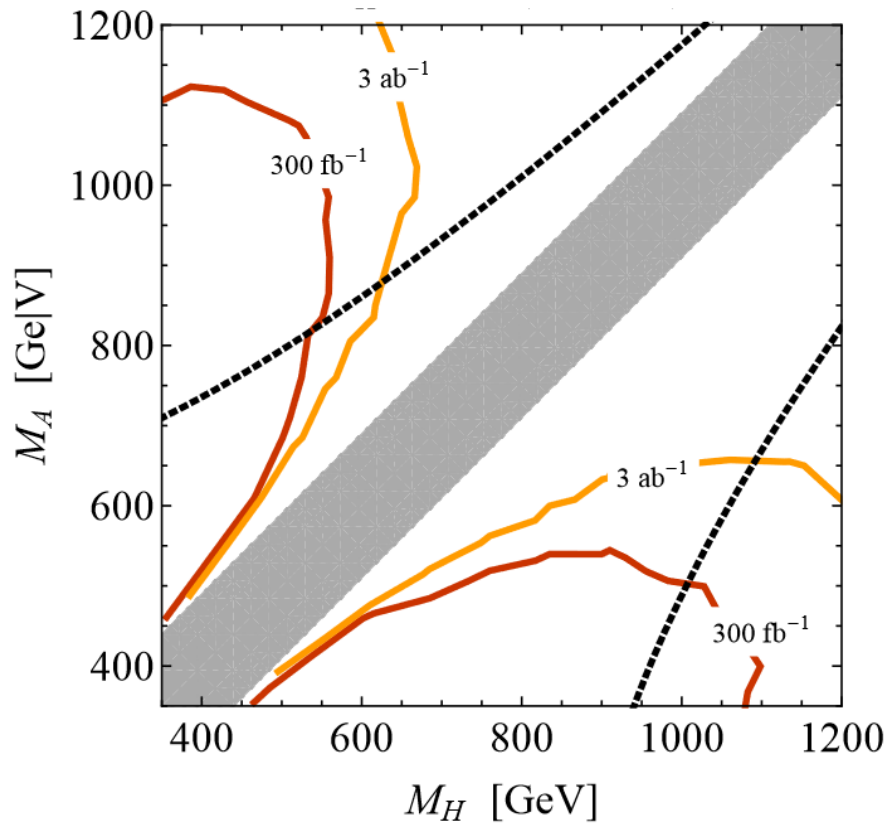


**Figure 6.17** Theoretical prediction of exclusion limits at different luminosities and  $\tan(\beta) = 1$ . For  $m_H > m_A$  the decay channel  $H \rightarrow ZA$  is considered. Taken from [12].

## 7 Conclusion and Outlook

First studies of a search for heavy Higgs bosons within the 2HDM at the LHC have been presented in this thesis, conducted in the decay channel  $A \rightarrow ZH \rightarrow Zt\bar{t}$  where  $A$  and  $H$  are heavy Higgs bosons. This channel has not yet been searched for at the LHC. For this analysis, the muon decay of the  $Z$  boson and the purely hadronic decay of the top quarks were considered, resulting in a final state topology with two leptons and six jets.

In the first part of this thesis, the basis transformation laws between the physical mass basis and the parameters of the 2HDM Lagrangian have been derived. The parameter space in the physical mass basis has been studied in detail and the behaviour of the production cross section and the branching ratios with respect to the heavy Higgs boson masses and the ratio between the vacuum expectation values  $\tan(\beta)$  has been examined. The study concluded that in most of the parameter space, especially at large mass differences between the  $A$  and the  $H$  and at low values of  $\tan(\beta)$ , the decay channel is the dominant decay for a hypothetical heavy Higgs boson  $A$ .

Events at different points in the parameter region have been produced and studied at generator level. The shape of the transverse momentum distribution of the  $Z$  boson has been derived and the discriminating power of this variable has been shown for several mass points following the study in [12]. The characteristic edge in the  $p_T^Z$  spectrum differs greatly from the background spectrum. Detector effects and showering have been simulated and the kinematic variables have been discussed after object and event selections. Especially at large mass differences, the  $p_T^Z$  edge reaches into areas with a low number of background events.

Exclusion limits have been calculated using the  $CL_s$  method and compared to the predicted theory cross sections. Beginning between 50-100 GeV beyond the production thresholds and at low  $\tan(\beta)$  values, most of the examined parameter space is expected to be excluded, provided no deviation from the predicted curve is observed.

Overall the results of this study are promising. The next natural step is to perform the search with real data. Some further improvements and future researches are of interest as well.

Even though the simulations with DELPHES are fairly accurate, a full scale GEANT based CMS detector simulation for the signal events would provide more realism. Furthermore, not all systematic uncertainties have been investigated so far. Missing are e.g. the b-tagging uncertainty, the lepton reconstruction efficiency and the trigger efficiency.

The analysis of this thesis was conducted for heavy Higgs boson masses below 1000 GeV. Most of the mass points in this region were excluded, so naturally an extension to higher masses would be of interest, to see how far the exclusion reaches. For higher masses a significant decrease in the production cross section is expected, a further analysis could determine exactly to which  $m_A$  expected exclusion region would reach.

Of further interest would be the combination with other sensitive variables as for example the

---

reconstructed  $H$  or  $A$  mass. These quantities could provide higher exclusion limits at regions with high  $m_H$ . Combining the results of this thesis with the analysis of other kinematic variables would provide a larger excluded region.

Another field of interest is the analysis of different decay modes for the top quarks. So far only the purely hadronic decay has been examined. The lepton + jets and the purely leptonic decay channels could complement the analysed decay channel.

Furthermore, combining the results of other decay modes would provide a conclusive overview of the excluded 2HDM parameter space to focus future searches on the yet unsearched regions.

## References

- [1] H. von Glasenapp, *Jainism: An Indian Religion of Salvation*, Dehli: Motilal Banarsidass, 1999, ISBN: 81-208-1376-6.
- [2] S. Berryman, “Ancient Atomism”, *The Stanford Encyclopedia of Philosophy*, ed. by Edward N. Zalta, Fall 2008, Metaphysics Research Lab, Stanford University, 2008.
- [3] E. Davis, “Discovery of the electron: Commentary on J. J. Thomson’s classic paper of 1897”, *Philosophical Magazine Letters - PHIL MAG LETT* 87 (May 2007), pp. 293–301, DOI: 10.1080/09500830701305514.
- [4] E. Rutherford, “The scattering of alpha and beta particles by matter and the structure of the atom”, *Philosophical Magazine* 21 (1911), pp. 669–688, URL: <https://personal.math.ubc.ca/~cass/rutherford/rutherford.html>.
- [5] J. Chadwick, “The existence of a neutron”, *Proc. R. Soc. Lond.* 21 (1932), pp. 692–708, URL: <https://royalsocietypublishing.org/doi/10.1098/rspa.1932.0112>.
- [6] L. Meitner and O.R. Frisch, “Products of the Fission of the Uranium Nucleus”, *Nature* 143 (1939), pp. 471–472, URL: <https://www.nature.com/articles/143471a0>.
- [7] O. Hahn and F. Strassmann, “Über den Nachweis und das Verhalten der bei der Bestrahlung des Urans mittels Neutronen entstehenden Erdalkalimetalle”, *Naturwissenschaften* 27 (1939), pp. 11–15, URL: <https://www.nature.com/articles/143471a0>.
- [8] M. Planck, “Über das Gesetz der Energieverteilung im Normalspectrum”, *Ann. Phy.* 4 (1901), pp. 553–563.
- [9] E. Schrödinger, “Quantisierung als Eigenwertproblem”, *Ann. Phy.* 79 (1926), pp. 361–376.
- [10] W. Heisenberg, “Über den anschaulichen Inhalt der quantentheoretischen Kinematik und Mechanik”, *Z. Phy.* 43 (1927), pp. 172–198.
- [11] N. Bohr, “On the Constitution of Atoms and Molecules”, *Phil. Mag.* 26 (1913), pp. 1–25.
- [12] U. Haisch and G. Polesello, “Searching for heavy Higgs bosons in the  $t\bar{t}Z$  and  $tbW$  final states”, *Journal of High Energy Physics* 2018.9 (Sept. 2018), ISSN: 1029-8479, URL: <https://arxiv.org/abs/1807.07734#>.
- [13] M.E. Peskin and D.V. Schroeder, *An introduction to quantum field theory*, Boulder, CO: Westview, 1995, ISBN: 978-0201503975.
- [14] D.J. Griffiths, *Introduction to elementary particles; 2nd rev. version*, Willey, 2008, ISBN: 9783527618477.

- [15] R. Wolf, *The Higgs Boson Discovery at the Large Hadron Collider*, Springer, 2015, ISBN: 978-3319354378, URL: <https://link.springer.com/book/10.1007/978-3-319-18512-5>.
- [16] *Standard Model*, URL: [https://en.wikipedia.org/wiki/Standard\\_Model](https://en.wikipedia.org/wiki/Standard_Model) (visited on 04/11/2021).
- [17] C. S. Wu et al., “Experimental Test of Parity Conservation in Beta Decay”, *Phys. Rev.* 105 (4 Feb. 1957), pp. 1413–1415, DOI: 10.1103/PhysRev.105.1413, URL: <https://link.aps.org/doi/10.1103/PhysRev.105.1413>.
- [18] A. Ceccucci, Z. Ligeti, and Y. Sakai, *The CKM Quark-mixing matrix*, URL: <https://pdg.lbl.gov/2020/reviews/rpp2020-rev-ckm-matrix.pdf> (visited on 04/11/2021).
- [19] E. Gallo et al., *Lecture notes "Advanced Particle physics", WS 2019/20, Universität Hamburg*.
- [20] V. Trimble, “Existence and Nature of Dark Matter in the Universe”, *ARA+A* 25 (Nov. 2003), pp. 425–472, DOI: 10.1146/annurev.aa.25.090187.002233.
- [21] P. A. R. Ade et al., “Planck2013 results. I. Overview of products and scientific results”, *Astronomy and Astrophysics* 571 (Oct. 2014), A1, ISSN: 1432-0746, DOI: 10.1051/0004-6361/201321529, URL: <http://dx.doi.org/10.1051/0004-6361/201321529>.
- [22] A. Sakharov, “Violation of CP invariance, C Asymetry and Baryon Asymetry of the universe”, *JETP Letters* 5 (1966), pp. 32–33.
- [23] G.C. Branco et al., “Theory and phenomenology of two-Higgs-doublet models”, *Physical Reports* 516.1-2 (July 2012), URL: <https://arxiv.org/abs/1106.0034>.
- [24] L. Altenkamp, “Precise Predictions within the Two-Higgs-Doublet Model”, Dissertation, Albert-Ludwigs-Universität Freiburg, Dec. 1, 2016.
- [25] H. Haber J., Gunion, “Conditions for CP violation in the general two-Higgs-doublet model”, *Physical Review D* 52 (Nov. 2005), URL: <https://link.aps.org/doi/10.1103/PhysRevD.72.095002>.
- [26] P Ferreira, R. Santos, and A. Barroso, “Stability of the tree-level vacuum in two Higgs doublet models against charge or CP spontaneous violation”, *Physics Letters B* 603.3-4 (Dec. 2004), pp. 219–229, URL: <http://dx.doi.org/10.1016/j.physletb.2004.10.022>.
- [27] C. Nishi, “Physical parameters and basis transformations in the two-Higgs-doublet model”, *Physical Review D* 77.5 (Mar. 2008), ISSN: 1550-2368, DOI: 10.1103/physrevd.77.055009, URL: <http://dx.doi.org/10.1103/PhysRevD.77.055009>.

## References

---

- [28] A. Kuncinas, “Analysing the extended Higgs sector of the standard Model: In search of stable CP-conserving Two Higgs Doublet potentials in different bases”, Undergraduate thesis, Vilnius University, 2017.
- [29] H. Haber and J. Silva, “Exceptional regions of the 2HDM parameter space”, *Physical Review D* 103.11 (June 2021), URL: <http://dx.doi.org/10.1103/PhysRevD.103.115012>.
- [30] M. Aoki et al., “Models of Yukawa interaction in the two Higgs doublet model, and their collider phenomenology”, *Physical Review D* 80.1 (July 2009), URL: <https://arxiv.org/abs/0902.4665>.
- [31] T. Nomura and P. Sanyal, “Lepton specific two-Higgs-doublet model based on a U(1)X gauge symmetry with dark matter”, *Physical Review D* 100.11 (Dec. 2019), ISSN: 2470-0029, DOI: 10.1103/physrevd.100.115036, URL: <http://dx.doi.org/10.1103/PhysRevD.100.115036>.
- [32] E. Graverini, “Flavour anomalies: a review”, *Journal of Physics: Conference Series* 1137 (Jan. 2019), p. 012025, DOI: 10.1088/1742-6596/1137/1/012025.
- [33] Muon  $g - 2$  Collaboration, “Measurement of the Positive Muon Anomalous Magnetic Moment to 0.46 ppm”, *Phys. Rev. Lett.* 126 (14 Apr. 2021), p. 141801, DOI: 10.1103/PhysRevLett.126.141801, URL: <https://link.aps.org/doi/10.1103/PhysRevLett.126.141801>.
- [34] L. Delle Rose et al., “ $R_{K}$  and  $R_{K^*}$  in an aligned 2HDM with right-handed neutrinos”, *Physical Review D* 101 (June 2020), DOI: 10.1103/PhysRevD.101.115009.
- [35] G. Arcadi et al., *A 2HDM for the  $g-2$  and Dark Matter*, 2021, arXiv: 2104.04456 [hep-ph].
- [36] *Higgs PAG Summary Plots*, *CERN Twiki*, URL: [https://twiki.cern.ch/twiki/bin/view/CMSPublic/SummaryResultsHIG#Summary\\_of\\_MSSM\\_Higgs\\_Boson\\_sear](https://twiki.cern.ch/twiki/bin/view/CMSPublic/SummaryResultsHIG#Summary_of_MSSM_Higgs_Boson_sear).
- [37] The CMS Collaboration, “Search for neutral resonances decaying into a Z boson and a pair of b jets or tau leptons”, *Physics Letters B* 759 (Aug. 2016), pp. 369–394, ISSN: 0370-2693, URL: <https://arxiv.org/abs/1603.02991>.
- [38] The CMS Collaboration, “Search for new neutral Higgs bosons through the  $H \rightarrow ZA \rightarrow \ell^+ \ell^- b \bar{b}$  process in pp collisions at  $\sqrt{s} = 13$  TeV”, *Journal of High Energy Physics* 2020.3 (), ISSN: 1029-8479, URL: <https://arxiv.org/abs/1911.03781>.
- [39] The ATLAS Collaboration, “Search for a heavy Higgs boson decaying into a Z boson and another heavy Higgs boson in the  $l\bar{l}b\bar{b}$  final state in pp collisions at  $s=13$  TeV with the ATLAS detector”, *Physics Letters B* 783 (Aug. 2018), pp. 392–414, ISSN: 0370-2693, URL: <https://arxiv.org/abs/1804.01126>.



- [40] The ATLAS Collaboration, “Search for a CP-odd Higgs boson decaying to Zh in pp collisions at 8 TeV with the ATLAS detector”, *Physics Letters B* 744 (May 2015), pp. 163–183, ISSN: 0370-2693, URL: <https://arxiv.org/abs/1502.04478>.
- [41] The ATLAS Collaboration, “Search for heavy resonances decaying into a W or Z boson and a Higgs boson in final states with leptons and b-jets at  $\sqrt{s} = 13$  TeV pp collisions with the ATLAS detector”, *Journal of High Energy Physics* 2018.3 (Mar. 2018), ISSN: 1029-8479, URL: <https://arxiv.org/abs/1712.06518>.
- [42] The CMS Collaboration, “Search for a pseudoscalar boson decaying into a Z boson and the 125 GeV Higgs boson in l+lbb final states”, *Physics Letters B* 748 (Sept. 2015), pp. 221–243, ISSN: 0370-2693, URL: <https://arxiv.org/abs/1504.04710>.
- [43] The CMS Collaboration, “Search for a heavy pseudoscalar boson decaying to a Z and a Higgs boson at  $\sqrt{s} = 13$  TeV”, *The European Physical Journal C* 79.7 (July 2019), ISSN: 1434-6052, URL: <https://arxiv.org/abs/1504.04710>.
- [44] The CMS Collaboration, “Search for physics beyond the standard model in events with two leptons of same sign, missing transverse momentum, and jets in proton-proton collisions at  $\sqrt{s} = 13$  TeV”, *The European Physical Journal C* 77.9 (Sept. 2017), ISSN: 1434-6052, URL: <https://arxiv.org/abs/1704.07323>.
- [45] The ATLAS Collaboration, “Search for supersymmetry at  $\sqrt{s} = 13$  TeV in final states with jets and two same-sign leptons or three leptons with the ATLAS detector”, *The European Physical Journal C* 76.5 (May 2016), ISSN: 1434-6052, URL: <https://arxiv.org/abs/1602.09058>.
- [46] The CMS Collaboration, “Search for beyond the standard model Higgs bosons decaying into a  $b\bar{b}$  pair in collisions at  $\sqrt{s} = 13$  TeV”, *Journal of High Energy Physics* 2018.8 (Aug. 2018), ISSN: 1029-8479, URL: <https://arxiv.org/abs/1805.12191>.
- [47] The CMS Collaboration, “Search for additional neutral MSSM Higgs bosons in the  $\tau\tau$  final state in proton-proton collisions at  $\sqrt{s} = 13$  TeV”, *Journal of High Energy Physics* 2018.9 (Sept. 2018), ISSN: 1029-8479, URL: <https://arxiv.org/abs/1803.06553>.
- [48] The CMS Collaboration, “Search for MSSM Higgs bosons decaying to  $\mu + \mu^-$  in proton-proton collisions at  $\sqrt{s} = 13$  TeV”, *Physics Letters B* 798 (Nov. 2019), p. 134992, ISSN: 0370-2693, URL: <https://arxiv.org/abs/1907.03152>.
- [49] A. D. Martin et al., “Parton distributions for the LHC”, *The European Physical Journal C* 63.2 (July 2009), pp. 189–285, ISSN: 1434-6052, DOI: 10.1140/epjc/s10052-009-1072-5, URL: <http://dx.doi.org/10.1140/epjc/s10052-009-1072-5>.
- [50] J. Collins, D. Soper, and G. Sterman, “Factorization of Hard Processes in QCD”, 5 (Sept. 2004), DOI: 10.1142/9789814503266\_0001.

## References

---

- [51] *2HDM cross section ntuple*, URL: <https://twiki.cern.ch/twiki/bin/view/LHCPhysics/LHCHWG2HDM?redirectedfrom=LHCPhysics.LHCHXSWG2HDM> (visited on 12/11/2021).
- [52] T. Mayer-Kuckuck, *Atomphysik*, 5th ed., Stuttgart: B.G. Teubner, 1997, pp. 129–133, ISBN: 3-519-43042-1.
- [53] O. Nachtmann, *Phaenomene und Konzepte der Elementarteilchenphysik*, Braunschweig: Vieweg, 1986, ISBN: 3-528-08926-1.
- [54] A Djouadi, J Kalinowski, and P.M. Zerwas, “Two- and Three-Body Decay Modes of SUSY Higgs Particles”, *Z.Phys* (Nov. 1995), URL: <https://arxiv.org/abs/hep-ph/9511342>.
- [55] J. Baglio and A. Djouadi, “Higgs production at the LHC”, *Journal of High Energy Physics* 2011.3 (Mar. 2011), ISSN: 1029-8479, URL: <https://arxiv.org/abs/1012.0530>.
- [56] A Djouadi, “The anatomy of electroweak symmetry breaking Tome II: The Higgs bosons in the Minimal Supersymmetric Model”, *Physics Reports* 459.1-6 (Apr. 2008), URL: <http://dx.doi.org/10.1016/j.physrep.2007.10.005>.
- [57] *Higgs working group twiki*, URL: <https://twiki.cern.ch/twiki/bin/view/LHCPhysics/CrossSections>.
- [58] J. Schaarschmidt, “The Discovery Potential of Neutral Supersymmetric Higgs Bosons with Decay to Tau Pairs at the ATLAS Experiment”, Dissertation, TU Dresden, Apr. 8, 2011, URL: <http://cds.cern.ch/record/1309945/files/CERN-THESIS-2010-164.pdf>.
- [59] V. Balagura, “Van der Meer scan luminosity measurement and beam-beam correction”, *The European Physical Journal C* 81.1 (Jan. 2021), ISSN: 1434-6052, DOI: 10.1140/epjc/s10052-021-08837-y, URL: <http://dx.doi.org/10.1140/epjc/s10052-021-08837-y>.
- [60] CMS Collaboration, *Public CMS Luminosity Information*, URL: <https://twiki.cern.ch/twiki/bin/view/CMSPublic/LumiPublicResults> (visited on 04/09/2021).
- [61] D. Boussard et al., “The LHC superconducting cavities”, vol. 2, Feb. 1999, 946–948 vol.2, ISBN: 0-7803-5573-3, DOI: 10.1109/PAC.1999.795409.
- [62] L. Rossi, “The LHC superconducting magnets”, 2003, URL: <https://accelconf.web.cern.ch/p03/PAPERS/TOAB001.PDF> (visited on 12/11/2021).
- [63] *LHC performance reaches new highs*, URL: <https://home.cern/news/news/accelerators/lhc-performance-reaches-new-highs> (visited on 04/11/2021).

- [64] *The LHC racks up records*, URL: <https://home.cern/news/news/accelerators/lhc-racks-records> (visited on 12/09/2021).
- [65] The ATLAS Collaboration, “The ATLAS Experiment at the CERN Large Hadron Collider”, *Journal of Instrumentation* 3.08 (Aug. 2008), S08003–S08003, DOI: 10.1088/1748-0221/3/08/s08003, URL: <https://doi.org/10.1088/1748-0221/3/08/s08003>.
- [66] The CMS Collaboration, “The CMS experiment at the CERN LHC”, *Journal of Instrumentation* 3.08 (Aug. 2008), S08004–S08004, DOI: 10.1088/1748-0221/3/08/s08004, URL: <https://doi.org/10.1088/1748-0221/3/08/s08004>.
- [67] The LHCb Collaboration, “The LHCb Detector at the LHC”, *Journal of Instrumentation* 3.08 (Aug. 2008), S08005–S08005, DOI: 10.1088/1748-0221/3/08/s08005, URL: <https://doi.org/10.1088/1748-0221/3/08/s08005>.
- [68] The ALICE Collaboration, “The ALICE experiment at the CERN LHC”, *Journal of Instrumentation* 3.08 (Aug. 2008), S08002–S08002, DOI: 10.1088/1748-0221/3/08/s08002, URL: <https://doi.org/10.1088/1748-0221/3/08/s08002>.
- [69] L. Evans and P. Bryant, “LHC Machine”, *Journal of Instrumentation* 3.08 (Aug. 2008), S08001–S08001, DOI: 10.1088/1748-0221/3/08/s08001, URL: <https://doi.org/10.1088/1748-0221/3/08/s08001>.
- [70] M. Zinser, “The Large Hadron Collider”, *Search for New Heavy Charged Bosons and Measurement of High-Mass Drell-Yan Production in Proton–Proton Collisions*, Cham: Springer International Publishing, 2018, pp. 47–51, ISBN: 978-3-030-00650-1, URL: [https://doi.org/10.1007/978-3-030-00650-1\\_4](https://doi.org/10.1007/978-3-030-00650-1_4).
- [71] *LHC running*, URL: [https://www.lhc-closer.es/taking\\_a\\_closer\\_look\\_at\\_lhc/0.lhc\\_running](https://www.lhc-closer.es/taking_a_closer_look_at_lhc/0.lhc_running) (visited on 12/10/2021).
- [72] URL: [https://www.lhc-closer.es/taking\\_a\\_closer\\_look\\_at\\_lhc/0.momentum](https://www.lhc-closer.es/taking_a_closer_look_at_lhc/0.momentum) (visited on 12/10/2021).
- [73] URL: <https://en.wikipedia.org/wiki/Pseudorapidity> (visited on 04/11/2021).
- [74] T. Sakuma and T. McCauley, “Detector and Event Visualization with SketchUp at the CMS Experiment”, *Journal of Physics: Conference Series* 513.2 (July 2014), p. 022032, ISSN: 1742-6596, DOI: 10.1088/1742-6596/513/2/022032, URL: <http://dx.doi.org/10.1088/1742-6596/513/2/022032>.
- [75] CMS Collaboration, *CMS Tracker Detector Performance Results*, *CERN Twiki*, URL: <https://twiki.cern.ch/twiki/bin/view/CMSPublic/DPGResultsTRK> (visited on 12/10/2021).

## References

---

- [76] P. Adzic et al., *Energy Resolution Performance of the CMS Electromagnetic Calorimeter*, tech. rep., Geneva: CERN, Sept. 2006, URL: <http://cds.cern.ch/record/1000388>.
- [77] Q. Ingram, “Energy resolution of the barrel of the CMS Electromagnetic Calorimeter”, *Journal of Instrumentation* 2.04 (Apr. 2007), P04004–P04004, DOI: 10.1088/1748-0221/2/04/p04004, URL: <https://doi.org/10.1088/1748-0221/2/04/p04004>.
- [78] The CMS Collaboration, *CMS Physics: Technical Design Report Volume 1: Detector Performance and Software*, Technical design report. CMS, Geneva: CERN, 2006, URL: <https://cds.cern.ch/record/922757>.
- [79] The CMS Collaboration, “Performance of the CMS muon detector and muon reconstruction with proton-proton collisions at  $\sqrt{s} = 13$  TeV”, *Journal of Instrumentation* 13.06 (June 2018), P06015–P06015, ISSN: 1748-0221, DOI: 10.1088/1748-0221/13/06/p06015, URL: <http://dx.doi.org/10.1088/1748-0221/13/06/p06015>.
- [80] *Public CMS Luminosity Information, CERN Twiki*, URL: [https://twiki.cern.ch/twiki/bin/view/CMSPublic/LumiPublicResults#2018\\_proton\\_proton\\_collisions](https://twiki.cern.ch/twiki/bin/view/CMSPublic/LumiPublicResults#2018_proton_proton_collisions) (visited on 02/12/2021).
- [81] *3.2 Data Formats and Data Tiers, CERN Twiki*, URL: <https://twiki.cern.ch/twiki/bin/view/CMSPublic/WorkBookDataFormats> (visited on 12/10/2021).
- [82] S. Cittolin, A. Racz, and P. Sphicas, *CMS The TriDAS Project: Technical Design Report, Volume 2: Data Acquisition and High-Level Trigger. CMS trigger and data-acquisition project*, Technical design report. CMS, Geneva: CERN, 2002, URL: <http://cds.cern.ch/record/578006>.
- [83] D. Barney, *CMS Detector Slice*, URL: <https://cds.cern.ch/record/2120661> (visited on 12/10/2021).
- [84] The CMS Collaboration, “Particle-flow reconstruction and global event description with the CMS detector”, *Journal of Instrumentation* 12.10 (Oct. 2017), P10003–P10003, ISSN: 1748-0221, DOI: 10.1088/1748-0221/12/10/p10003, URL: <http://dx.doi.org/10.1088/1748-0221/12/10/p10003>.
- [85] *Baseline muon selections for Run-II*, URL: [https://twiki.cern.ch/twiki/bin/viewauth/CMS/SWGuideMuonIdRun2#Tight\\_Muon](https://twiki.cern.ch/twiki/bin/viewauth/CMS/SWGuideMuonIdRun2#Tight_Muon) (visited on 12/10/2021).
- [86] J. Rembser, “CMS Electron and Photon Performance at 13 TeV”, *Journal of Physics: Conference Series* 1162 (Jan. 2019), p. 012008, DOI: 10.1088/1742-6596/1162/1/012008, URL: <https://doi.org/10.1088/1742-6596/1162/1/012008>.
- [87] *Electron Identification Based on Simple Cuts, CERN Twiki*, URL: [https://twiki.cern.ch/twiki/bin/view/CMSPublic/EgammaPublicData#Electron\\_ID\\_Working\\_Points](https://twiki.cern.ch/twiki/bin/view/CMSPublic/EgammaPublicData#Electron_ID_Working_Points) (visited on 02/12/2021).

- [88] M Cacciari, G Salam, and G. Soyez, “The anti-ktjet clustering algorithm”, *Journal of High Energy Physics* 2008.04 (Apr. 2008), pp. 063–063, DOI: 10.1088/1126-6708/2008/04/063, URL: <https://doi.org/10.1088/1126-6708/2008/04/063>.
- [89] G. Salam, “Towards Jetography”, *The European Physical Journal C* 67 (June 2009), DOI: 10.1140/epjc/s10052-010-1314-6.
- [90] *Jet Identification for the 13 TeV data Run2016*, CERN Twiki, URL: <https://twiki.cern.ch/twiki/bin/view/CMS/JetID13TeVRun2016> (visited on 02/12/2021).
- [91] D. Bertolini et al., “Pileup per particle identification”, *Journal of High Energy Physics* 2014.10 (Nov. 2014), ISSN: 1029-8479, DOI: 10.1007/jhep10(2014)059, URL: [http://dx.doi.org/10.1007/JHEP10\(2014\)059](http://dx.doi.org/10.1007/JHEP10(2014)059).
- [92] CMS Collaboration, “New Developments for Jet Substructure Reconstruction in CMS” (July 2017), URL: <https://cds.cern.ch/record/2275226>.
- [93] *Performance of the CMS.DeepJet b tagging algorithm using 41.9/fb of data from proton-proton collisions at 13TeV with Phase 1 CMS detector*, CERN Twiki, URL: <https://twiki.cern.ch/twiki/bin/view/CMSPublic/BTV13TeV2017DeepJet> (visited on 02/12/2021).
- [94] *Z Boson*, Particle Data Group, 2018, URL: <https://pdg.lbl.gov/2018/listings/rpp2018-list-z-boson.pdf>.
- [95] *Top Quark*, Particle Data Group, 2019, URL: <https://pdg.lbl.gov/2019/reviews/rpp2019-rev-top-quark.pdf>.
- [96] J. Alwall et al., “The automated computation of tree-level and next-to-leading order differential cross sections, and their matching to parton shower simulations”, *Journal of High Energy Physics* 2014.7 (July 2014), ISSN: 1029-8479, URL: <https://arxiv.org/abs/1405.0301>.
- [97] C. Duhr, M. Herquet, and C. Degrande, *The general Two-Higgs-Doublet Model*, URL: <https://feynrules.irmp.ucl.ac.be/wiki/2HDM>.
- [98] R.D. Ball, “Parton distributions from high-precision collider data”, *Eur. Phys. J. C* 77 (2017), p. 663, DOI: 10.1140/epjc/s10052-017-5199-5, arXiv: 1706.00428 [hep-ph].
- [99] P. Artoisenet et al., “Automatic spin-entangled decays of heavy resonances in Monte Carlo simulations”, *Journal of High Energy Physics* 2013.3 (Mar. 2013), ISSN: 1029-8479, DOI: 10.1007/jhep03(2013)015, URL: [http://dx.doi.org/10.1007/JHEP03\(2013\)015](http://dx.doi.org/10.1007/JHEP03(2013)015).

## References

---

- [100] T. Sjostrand, S. Mrenna, and P. Skands, “A brief introduction to PYTHIA 8.1”, *Computer Physics Communications* 178.11 (June 2008), pp. 852–867, ISSN: 0010-4655, URL: <https://arxiv.org/abs/0710.3820>.
- [101] A. M. Sirunyan et al., “Extraction and validation of a new set of CMS PHYTHIA 8 tunes from underlying-event measurements”, *Eur. Phys. J. C* 80 (2020), p. 4.
- [102] S. Ovin, X. Rouby, and V. Lemaitre, “Delphes, a framework for fast simulation of a generic collider experiment” (Mar. 2009), URL: <https://arxiv.org/abs/0903.2225>.
- [103] S. Agostinelli, J. Allison, and K. Amako, “Geant4-a simulation toolkit”, *Nuclear Instruments and Methods in Physics Research Section A: Accelerators, Spectrometers, Detectors and Associated Equipment* 506.3 (2003), pp. 250–303, ISSN: 0168-9002, DOI: [https://doi.org/10.1016/S0168-9002\(03\)01368-8](https://doi.org/10.1016/S0168-9002(03)01368-8), URL: <https://www.sciencedirect.com/science/article/pii/S0168900203013688>.
- [104] M. Selvaggi, *Fast Detector Simulation*, URL: [https://www.physics.sjtu.edu.cn/madgraphschoo/sites/www.physics.sjtu.edu.cn/madgraphschoo/files/delphes\\_MG\\_school.pdf](https://www.physics.sjtu.edu.cn/madgraphschoo/sites/www.physics.sjtu.edu.cn/madgraphschoo/files/delphes_MG_school.pdf) (visited on 02/12/2021).
- [105] S. Frixione, P. Nason, and C. Oleari, “Matching NLO QCD computations with parton shower simulations: the POWHEG method”, *JHEP* 11 (2007), p. 070, DOI: 10.1088/1126-6708/2007/11/070, arXiv: 0709.2092 [hep-ph].
- [106] S. Alioli et al., “A general framework for implementing NLO calculations in shower Monte Carlo programs: the POWHEG BOX”, *JHEP* 06 (2010), p. 043, DOI: 10.1007/JHEP06(2010)043, arXiv: 1002.2581 [hep-ph].
- [107] T. Ježo and P. Nason, “On the Treatment of Resonances in Next-to-Leading Order Calculations Matched to a Parton Shower”, *JHEP* 12 (2015), p. 065, DOI: 10.1007/JHEP12(2015)065, arXiv: 1509.09071 [hep-ph].
- [108] H. Hartanto et al., “Higgs boson production in association with top quarks in the POWHEG BOX”, *Phys. Rev. D* 91 (2015), p. 094003, DOI: 10.1103/PhysRevD.91.094003, arXiv: 1501.04498 [hep-ph].
- [109] J. Alwall et al., “The automated computation of tree-level and next-to-leading order differential cross sections, and their matching to parton shower simulations”, *JHEP* 07 (2014), p. 079, DOI: 10.1007/JHEP07(2014)079, arXiv: 1405.0301 [hep-ph].
- [110] A. Kulesza et al., “Associated production of a top quark pair with a heavy electroweak gauge boson at NLO+NNLL accuracy”, *Eur. Phys. J. C* 79 (2019), p. 249, DOI: 10.1140/epjc/s10052-019-6746-z, arXiv: 1812.08622 [hep-ph].

- [111] *How to Compute Cross Sections with the GenXSecAnalyzer*, CERN Twiki, URL: <https://twiki.cern.ch/twiki/bin/viewauth/CMS/HowToGenXSecAnalyzer> (visited on 02/12/2021).
- [112] *Standard Model Cross Sections for CMS at 13 TeV*, TWiki: [https://twiki.cern.ch/twiki/bin/viewauth/CMS/StandardModelCrossSectionsat13TeV\\_r26](https://twiki.cern.ch/twiki/bin/viewauth/CMS/StandardModelCrossSectionsat13TeV_r26).
- [113] *CMS XSDB entry for WJetsToQQ HT180 13TeV-madgraphMLM-pythia8*, MCM: [https://cms-gen-dev.cern.ch/xsdb/?searchQuery=DAS=WJetsToQQ\\_2868HT180\\_13TeV-madgraphMLM-pythia8..](https://cms-gen-dev.cern.ch/xsdb/?searchQuery=DAS=WJetsToQQ_2868HT180_13TeV-madgraphMLM-pythia8..)
- [114] *NNLO+NNLL top-quark-pair cross sections: ATLAS-CMS recommended predictions for top-quark-pair cross sections using the Top++v2.0 program*, TWiki: [https://twiki.cern.ch/twiki/bin/view/LHCPhysics/TtbarNNLO\\_r16](https://twiki.cern.ch/twiki/bin/view/LHCPhysics/TtbarNNLO_r16).
- [115] *NLO single-top channel cross sections: ATLAS-CMS recommended predictions for single-top cross sections using the Hathor v2.1 program*, TWiki: [https://twiki.cern.ch/twiki/bin/view/LHCPhysics/SingleTopRefXsec\\_r34](https://twiki.cern.ch/twiki/bin/view/LHCPhysics/SingleTopRefXsec_r34).
- [116] CMS Collaboration, “CMS Physics Technical Design Report: Addendum on High Density QCD with Heavy Ions” (Jan. 2007).
- [117] R. Barlow, *Statistics, A Guide to the Use of Statistical Methods in the Physical Science*, Chichester: John Wiley and Sons, Ltd., 1989, pp. 71–95, ISBN: 978-0471922957.
- [118] The LHC Higgs Combination Group The ATLAS Collaboration The CMS Collaboration, *Procedure for the LHC Higgs boson search combination in Summer 2011*, tech. rep., CERN, Aug. 2011, URL: <https://cds.cern.ch/record/1379837>.
- [119] A. Read, “Presentation of search results: the CL<sub>s</sub> technique”, *Journal of Physics G: Nuclear and Particle Physics* 28.10 (Sept. 2002), pp. 2693–2704, DOI: 10.1088/0954-3899/28/10/313, URL: <https://doi.org/10.1088/0954-3899/28/10/313>.
- [120] A. Read, “Modified frequentist analysis of search results (the CL<sub>s</sub> method)”, *CERN Report* (Jan. 2000), URL: <https://cds.cern.ch/record/451614/files/open-2000-205.pdf>.
- [121] G. Cowan et al., “Asymptotic formulae for likelihood-based tests of new physics”, *The European Physical Journal C* 71.2 (Feb. 2011), ISSN: 1434-6052, DOI: 10.1140/epjc/s10052-011-1554-0, URL: <https://arxiv.org/abs/1007.1727>.
- [122] U. Haisch and G. Polesello, “Searching for heavy Higgs bosons in the  $t\bar{t}Z$  and  $tbW$  final states”, *Journal of High Energy Physics* 2018.9 (Nov. 2018), ISSN: 1029-8479, DOI: 10.1007/jhep09(2018)151, URL: <https://arxiv.org/abs/1807.07734>.





# Danksagung

Mein Dank gilt den vielen Menschen, die mich während meines Studiums und dieser Masterarbeit begleitet haben.

Zu allererst Prof. Johannes Haller für die Möglichkeit, die Arbeit in seiner Forschungsgruppe zu schreiben. Das Masterprojekt hat mir sehr viel Freude bereitet und war thematisch ein absoluter Volltreffer. Durch zahlreiche Diskussionen und hilfreiche Tipps, insbesondere in unseren wöchentlichen Gruppenmeetings, habe ich sehr viel gelernt, wofür ich sehr dankbar bin. Für die exzellente Betreuung möchte ich mich besonders bei Dr. Matthias Schröder bedanken. Regelmäßige Meetings, immer ein offenes Ohr für Fragen und ein Talent für das Erklären physikalischer Sachverhalte: Seine Zeit und sein Engagement waren unglaublich wichtige Stützen während meines Masterprojekts. Bei Prof. Gregor Kasieczka möchte ich mich dafür bedanken, dass er sich dieser Arbeit als Zweitgutachter angenommen hat.

Auch den anderen Mitgliedern der Arbeitsgruppe bin ich sehr dankbar. Besonders Ksenia und Henrik möchte ich hier erwähnen, die mir unzählige Anfängerfragen verständlich und geduldig erklärt und mir viele Tipps zu meinem Projekt gegeben haben. Mit solchen Menschen fällt das Einarbeiten und Einleben in einer neuen Arbeitsgruppe sehr leicht. Auch für das gründliche Korrekturlesen dieser Arbeit bin ich sehr dankbar. Vielen Dank auch an alle anderen Mitglieder der Arbeitsgruppe. Die offene und freundliche Atmosphäre hat die Arbeit sehr angenehm gemacht.

Mein Dank gilt weiterhin ganz besonders meiner Freundin Leonie, die mich in dieser stressigen Zeit sowie während meines gesamten Studiums, so liebevoll unterstützt, mir den Rücken frei gehalten und diese Arbeit korrekturgelesen hat. Für den häufigen gemeinsamen Austausch, das Krafttanken bei leckerem Essen und die Unterstützung während meines gesamten Studiums möchte ich mich bei meiner Mutter bedanken. Den Weg des Studiums alleine zu bestreiten, wäre für mich eine undenkbare Vorstellung, deshalb möchte ich mich bei Johanna und Lea bedanken für die vielen schönen Momente und das gemeinsame Meistern von so mancher Univeranstaltung.

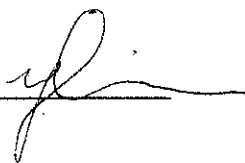
Meine Ausbildungszeit war immer wieder geprägt von Menschen, die ihrer Lehrtätigkeit mit besonderer Hingabe nachgegangen sind. Diese Menschen sind mir auf verschiedenen Stationen meines Weges eine große Inspiration gewesen. Mein Dank gilt daher Angelika Titze-Knuth und Marcus Jacobs für ihren fantastischen Unterricht, sowie Dr. Paolo Gunnellini für die beste Vorlesung meines Masterstudiums und die Beratung zu einem Masterprojekt in der Teilchenphysik.

*Vielen Dank!*



## **Eidesstattliche Erklärung**

Ich versichere, dass ich die beigefügte schriftliche Masterarbeit selbstständig angefertigt und keine anderen als die angegebenen Hilfsmittel benutzt habe. Alle Stellen, die dem Wortlaut oder dem Sinn nach anderen Werken entnommen sind, habe ich in jedem einzelnen Fall unter genauer Angabe der Quelle deutlich als Entlehnung kenntlich gemacht. Dies gilt auch für alle Informationen, die dem Internet oder anderer elektronischer Datensammlungen entnommen wurden. Ich erkläre ferner, dass die von mir angefertigte Masterarbeit in gleicher oder ähnlicher Fassung noch nicht Bestandteil einer Studien- oder Prüfungsleistung im Rahmen meines Studiums war. Die von mir eingereichte schriftliche Fassung entspricht jener auf dem elektronischen Speichermedium. Ich bin damit einverstanden, dass die Masterarbeit veröffentlicht wird.

Pinneberg, 14.12.21 

Ort, Datum, Unterschrift